Ice Accretion on Aerofoils

University of Nottingham

Zaid Ayaz Janjua, B.E., MSc.

Thesis submitted to the University of Nottingham

for the degree of Doctor of Philosophy

March 2017

Abstract

Ice accretion on aerofoils is a problematic phenomenon affecting power lines, ships and aircraft wings. This work thus undertakes an experimental and computational investigation into the formation and adhesion of ice on aerofoils. An experimental setup to test the adhesion strength of ice was designed and tested for repeatability and the effect of temperature on it. It was found that the ambient temperature has a profound effect on the adhesion strength, possibly due to dependence on the heat transfer mechanism through an amorphous liquid-like layer between ice and substrate. The tests were expanded to determine the effect of contact angle parameters on the icephobicity of 14 nanocoatings. It was found that the surface should possess high receding contact angle and low CAH to reduce adhesion thereby reducing the ice-substrate contact points. Hydrophobicity and icephobicity may not necessarily be dual characteristics of a surface unless the aforementioned criteria is satisfied. Anti-icing tests on the same coatings showed that

the freezing time of a droplet on the surface reduces with an increase in static contact angle. To understand the role of mixed ice, a one dimensional model is introduced to measure the accretion of mixed, rime and glaze ice on an aerofoil. This process occurs in four distinct stages and the effect of atmospheric parameters on the transition time between different growth types and height is determined. This mode was developed further to include a convective term to determine the profile of ice when rime grows above glaze/mixed with water flowing inside. This is a first step towards understanding the links between porous structures, ice structures and runback water that can generate interesting icy structures. This work forms part of the ICECOAT project funded by the EU Framework 7 CleanSky programme under grant award JTI-CS-2012-02-SFWA-01-051.

A list of papers that have been published is as follows:

Conference

[1] Janjua Z.A., Turnbull B., Hibberd S. and Choi K-S, 2015. The accretion of mixed ice on an aircraft wing due to the partial freezing of impinging supercooled droplets. European Drag Reduction and Flow Control Meeting - EDRFCM 2015, 23–26 March, Cambridge, UK.

[2] Zaid Janjua, Barbara Turnbull, Stephen Hibberd, and Kwing-So Choi."A Four-Stage One-Dimensional Model for Rime, Mixed and Glaze Ice Accretion on Aerofoils", AIAA Modeling and Simulation Technologies Conference, AIAA SciTech Forum, (AIAA 2017-1760).

[3] Zaid Janjua, Barbara Turnbull, Junpeng Liu, Xiang Hui Hou, and Kwing-So Choi. "Performance and Wear Tests of Icephobic Nanocoatings to Prevent Ice Accretion on Aerofoils", 58th AIAA/ASCE/AHS/ASC Structures, Structural Dynamics, and Materials Conference, AIAA SciTech Forum, (AIAA 2017-0353).

Journal

[1] Liu J., Janjua Z.A., Roe M., Xu F., Turnbull B., Choi K-S and Hou X, 2016. Super-hydrophobic/icephobic coatings based on silica nanoparticles modified by self-assembled monolayers. Nanomaterials, 232(6), 1–10.

[2] Janjua Z.A., Turnbull B., Choy K-L., Pandis C., Liu J., Hou X., Choi K.-S., 2017. Performance and Durability Tests of Smart Icephobic Coatings to Reduce Ice Adhesion. Applied Surface Science, 407, 555-564.

[3] Janjua Z.A., 2017. The influence of freezing and ambient temper-

ature on the adhesion strength of ice. Cold Regions Science and Technology, 140, 14–19.

Acknowledgements

Bismillah Hir Rahman Nir Rahim. There are several individuals without whom such a task would be impossible to achieve. My parents, Ayaz and Rukhsana, have been a constant source of inspiration and support throughout my studies. Growing up with an engineer and doctor as role models, has inculcated a dedication towards the sciences which I wish to pursue throughout my life. To Dr. Barbara Turnbull, I am eternally grateful. From the initial offer to join this project, to the countless hours of weekly supervision meetings to help me through difficult times and the amazing effort taken towards improving my writing and research skills; I could never have imagined that I would be blessed with such an incredible supervisor. To my co-supervisors Professor Kwing-So Choi and Dr. Stephen Hibberd. From the former, I have learned dedication and a tireless appetite for research, whilst the latter has most kindly helped in the difficult task of modelling with patience and encouragement. To Dr. Donald Giddings, for his most

useful suggestions during our yearly review meetings. I would like to thank Aishapi, Asad bhai, Sofia and Aiden for providing a welcome relief over the weekends and a family environment throughout my masters and PhD. To all the technicians: Nigel, Gary, Sam, Steve, Jim, Dan, Steve and Carl; I would have never been able to enter that cold chamber without your supervision and constant reminders of safety. To the rest of the ICECOAT team: Dr. Hou and Prof. Choy; for working tirelessly in the completion of a successful project.

I would like to thank the EU for sponsoring ICECOAT; part of the Clean Sky Joint-Undertaking to develop a "Novel aircraft de-icing concept based on smart coatings with electro-thermal system". The project code was JTI-CS-2012-02-SFWA-01-051 with coordinating person Prof. Kwing-So Choi.

I would like to thank all of my friends including but not limited to Ushashi, Rohit, Shivansh, Mevish, Jummy, Shreya, Jeff and Lucia for their endless tolerance of my complaints and jokes! The L4-135 office including Dr. Wang, Dr. Kim, Long Fei, Paul, Navid, Alessio, Noura, Domenico and Arnold; thank you for keeping my spirits up always! To everyone else who was not named here, I am grateful for your contribution towards the completion of this PhD. as well.

Contents

1 Introduction **34**

1.1 Ice Accretion on Aerofoils 35

1.2 Ice Adhesion Testing 45

1.3 Icephobic Coatings Design 46

1.4 Ice Accretion Modelling 47

2 Design and Calibration of a Centrifuge Ice Adhesion Test **54**

2.1 Introduction 54

2.2 Design Specifics 59

2.3 Method 61

2.3.1 Ice sample preparation 61

2.3.2 Adhesion stress tests 62

2.4 Repeatability Tests - Coffee Bean Mould 63

2.5 Repeatability Tests - Cuboid Mould 67

2.5.1 Mould Design 67

2.5.2 Substrate Description 68

2.5.3 Ice Characteristics 69

2.5.4 Surface Roughness Characterisation 70

2.5.5 Contact Angle Measurements 71

2.5.6 Results and Analysis 73

2.6 Conclusion 85

3 Centrifuge Adhesion Tests of Icephobic Coatings 87

3.1 Introduction 87

3.2 Coating Design 89

3.3 Experimental setup and procedure 93

3.4 Results 97

3.4.1 Uncoated substrates 97

3.4.2 Coated Substrates 101

3.5 Analysis 114

3.6 Conclusion 134

4 Static Anti-icing Adhesion Tests using Icephobic Coatings 139

4.1 Introduction 139

4.2 Methodology 142

4.3 Results and Analysis 145

4.4 Conclusion 158

5 A One-dimensional Mixed Ice Accretion Model 160

5.1 Introduction 160

5.2 Model Assumptions 165

5.3 Model Formulation 166

5.3.1 Mass Flux of Droplets 167

5.3.2 Rime Ice 171

5.3.3 Mixed Ice 172

5.3.4 Energy Balance 175

5.3.5 Freezing Fraction 181

5.3.6 Secondary Mixed Ice 184

5.3.7 Accretion Types 187

5.4 Solution Procedure 189

5.5 Results and Analysis 189

5.5.1 Variation of Ice Height and Freezing Fraction λ with Rime Ice Density and Ambient Temperature 193

5.5.2 Variation of Ice Height and Freezing Fraction λ with Liquid Water Content 199

5.5.3 Variation of Ice Height and Freezing Fraction λ with Air Velocity 201

5.5.4 Variation of Ice Height and Freezing Fraction λ with Collection Efficiency 205

5.5.5 Variation of Ice Height and Freezing Fraction λ with Angle of Attack 206

5.5.6 A Comparison with Myers and Charpin Code 209

5.5.7 A Comparison with Experimental Data 213

5.6 Conclusion 214

6 Two-dimensional Mixed Ice Accretion Model 217

6.1 Introduction 217

6.2 Mathematical Formulation 222

6.2.1 Solution Procedure 228

6.3 Results and Analysis 230

6.3.1 Non-Dimensionalisation 231

6.3.2 Ice Accretion under Different Scenarios 241

6.3.3 Effect of Runback Water 247

6.4 Conclusion 249

7 Conclusion **253**

8 Future Work **256**

A **258**

B **273**

List of Figures

1.1 Cross-sectional view of aircraft wing in flight showing different regions of liquid movement and ice formation. 37

1.2 Photograph of rime ice accretion on fuselage nose of an aircraft [1]. 39

1.3 Aerial view of an aircraft wing showing separate regions of glaze and runback ice formation. 41

1.4 Close-up photograph of glaze ice accretion after 22.5 minute warm-hold spray at the NASA Glenn Icing Research Tunnel [2]. The flow of the water film is from right to left. 43

1.5 Mixed ice as a combination of glaze and rime from experiments at NASA-Lewis Research Center [3]. 44

2.1 Detailed schematic of centrifuge set-up for the adhesion tests. 58

2.2 Schematic of stainless steel drum used for adhesion tests. . . . 60

2.3 Photo of ice attached to substrate inside environmental chamber, Z.Janjua. 60

2.4 Contact angle measurements of SS 304. 75

2.5 Contact angle measurements of Al 6082-T651. 75

2.6 Contact angle measurements of Al 1050A-H14. 75

2.7 The adhesion strength of the three different substrate types at different preparation and ambient temperatures. T_p = -5°C, T_a = -5°C (1); T_p = -10°C, T_a = -5°C (2); T_p = -5°C, T_a = -10°C (3); T_p = -10°C, T_a = -10°C (4). 78

2.8 Adhesion strength for SS 304, Al 1050A-H14 and Al 6082-T651 versus a) Static contact angle, b) Advancing contact angle, c) Receding contact angle and d) Contact angle hysteresis. 81

3.1 A schematic diagram of the Aerosol Assisted Deposition process [4]. 94

3.2 Mean adhesion speed of 20 uncoated aluminium 6082-T651 substrates. 98

3.3 Example measurements of 1) Static (101.09°), 2) Advancing (104.92°), 3) Receding contact angle (77.32°) respectively for Coating A. 4) shows the top view of the coating. 101

3.4 ARF and CAH versus number of cycles for coating A. 102

3.5 Example measurements of 1) Static (103.9°), 2) Advancing (109.1°), 3) Receding contact angle (76.2°) respectively for Coating B. 4) shows the top view of the coating. 103

3.6 ARF and CAH versus number of cycles for coating B. 104

3.7 Example measurements of 1) Static (129.1°), 2) Advancing (138.44°), 3) Receding contact angle (79.14°) respectively for Coating C. 4) shows the top view of the coating. 105

3.8 ARF and CAH versus number of cycles for coating C. 106

3.9 Example measurements of 1) Static (133.75°), 2) Advancing (141.29°), 3) Receding contact angle (76.74°) respectively for Coating D. 4) shows the top view of the coating. 107

3.10 ARF and CAH versus number of cycles for coating D. 108

3.11 Ice attached to coating E inside environmental chamber. . . . 108

3.12 Static contact angle measurement example of coating E prior to testing. 109

3.13 Coating E under Alicona optical microscope at 20x magnification. 109

3.14 Ice attached to coating F inside environmental chamber. . . . 110

3.15 Static contact angle measurement example of coating F prior to testing. 110

3.16 Coating F under Alicona optical microscope at 20x magnification. 111

3.17 Coating G after cycle 2. The ice shearing off visibly removed the coating clearly indicating poor adhesion to the substrate. . 111

3.18 Static contact angle measurement example of coating G prior to testing. 112

3.19 Coating G under Alicona optical microscope at 20x magnification. 112

3.20 ARF versus number of cycles for coating G. 113

3.21 Example measurements of 1) Static (137.65°), 2) Advancing (143.71°), 3) Receding contact angle (61.83°) respectively for Coating H. 4) shows the top view of the coating. 114

3.22 Coating H under Alicona optical microscope at 20x magnification. 115

3.23 ARF and CAH versus number of cycles for coating H. 116

3.24 Example measurements of 1) Static (159.58°), 2) Advancing (154.79°), 3) Receding contact angle (148.98°) respectively for Coating I. 4) shows the top view of the coating. 118

3.25 Coating I under Alicona optical microscope at 20x magnification. 119

3.26 ARF and CAH versus number of cycles for coating I. 120

3.27 Example measurements of 1) Static (113.38°), 2) Advancing (131.91°), 3) Receding contact angle (54.26°) respectively for Coating J. 4) shows the top view of the coating. 122

3.28 Coating J under Alicona optical microscope at 20x magnification. 123

3.29 ARF and CAH versus number of cycles for coating J. 124

3.30 Example measurements of 1) Static (108.33°), 2) Advancing (132.95°), 3) Receding contact angle (67.54°) respectively for Coating K. 4) shows the top view of the coating. 125

3.31 ARF and CAH versus number of cycles for coating K. 126

3.32 Example measurements of 1) Static (111.52°), 2) Advancing (133.78°), 3) Receding contact angle (34.11°) respectively for Coating L. 4) shows the top view of the coating. 127

3.33 ARF and CAH versus number of cycles for coating L. 128

3.34 Example measurements of 1) Static (107.83°), 2) Advancing (118.22°), 3) Receding contact angle (31.93°) respectively for Coating M. 4) shows the top view of the coating. 129

3.35 ARF and CAH versus number of cycles for coating M. 130

3.36 Example measurements of 1) Static (156.93°), 2) Advancing (161.19°), 3) Receding contact angle (130.69°) respectively for Coating N. 4) shows the top view of the coating. 131

3.37 ARF and CAH versus number of cycles for coating N. 132

3.38 Ice adhesion for all 14 coatings versus a) Static, b) Advancing, c) Receding contact angle and d) Contact angle hysteresis. . . 133

3.39 SEM micrographs of sample K at a magnification of 30000X obtained (a) before and (b) after the ice adhesion tests. 137

3.40 Adhesion strength versus CAH plotted for SS 304, Al 1050A-H14 and Al 6082-T651 in comparison to Gaussian best fit from equation 3.2. 138

4.1 Schematic of cold plate setup for icing time measurements of a water droplet. 144

4.2 Freezing times of droplets at plate temperature of -5°C. 153

4.3 Freezing times of droplets at plate temperature of -10°C. . . . 155

4.4 Freezing times of droplets at -5°C versus a) Static, b) Advancing, c) Receding and d) CAH. 156

4.5 Freezing times of droplets at -10°C versus a) Static, b) Advancing, c) Receding and d) CAH. 157

5.1 Schematic representation of the modes of accretion in mixed ice formation. At times $t < t_w$, supercooled droplets freeze on impact with the wing, forming rime ice (with air in the pore space). 167

5.2 Schematic representation of the modes of accretion in mixed ice formation. When the layer of rime ice is thick enough that the latent heat released on freezing can no longer be conducted through it, a proportion of the incoming supercooled droplets remain as water. This percolated water quickly freezes as glaze ice within the pore spaces of the original rime layer ($t_w \geq t < t_b$). 168

5.3 Schematic representation of the modes of accretion in mixed ice formation. Once the glaze ice fully occupies the pore space between the rime crystals, rime and glaze can accrete simultaneously in a mixed ice layer, enhancing the thermal conductivity over rime ice alone. 169

5.4 Schematic representation of the modes of accretion in mixed ice formation. The *mixed ice* layer restricts the transport of released latent heat and a water film forms on its surface. This leads to the formation of glaze ice. This may be supplemented by runback water formed by melting ice formations at the wing leading edge. 170

5.5 Mixed ice accretion model at T_a = -5°C and $\phi = 0.65$. 192

5.6 Freezing fraction versus accretion time at T_a = -5°C and $\phi = 0.65$. 192

5.7 Temperature profile of mixed ice accretion model at T_a = -5°C and $\phi = 0.65$. 193

5.8 Mixed ice accretion model at T_a = -3°C and $\phi = 0.65$. 194

5.9 Mixed ice accretion model at T_a = -3°C and $\phi = 0.96$. 194

5.10 Mixed ice accretion model at T_a = -6°C and $\phi = 0.65$. 195

5.11 Mixed ice accretion model at T_a = -6°C and $\phi = 0.96$. 195

5.12 Variation in freezing fraction λ with changes in packing fraction ϕ for 100 s. 197

5.13 Variation in freezing fraction λ with changes in atmospheric temperature T_a for 100 s. 198

5.14 Ice accretion versus LWC. 1) T_a = -3°C, ϕ = 0.65, ρ_a = 0.001 kg m^{-3}. Occurrence of Stage A (0–4 s), B (4–20 s) and C (20–30 s). 2) T_a = -3°C, ϕ = 0.65, ρ_a = 0.002 kg m^{-3}. Occurrence of Stage A (0–1 s), B (1–13 s), C (13–18 s) and D (18–30 s). 3) T_a = -6°C, ϕ = 0.65, ρ_a = 0.001 kg m^{-3}. Occurrence of Stage A (0–12 s) and B (12–30 s). 4) T_a = -6°C, ϕ = 0.65, ρ_a = 0.002 kg m^{-3}. Occurrence of Stage A (0–2 s), B (2–18 s) C (18–28 s) and D (28–30 s). 200

5.15 Variation in freezing fraction λ with changes in ρ_a for 100 s. . . 201

5.16 Ice accretion versus air velocity. 1) T_a = -3°C, ϕ = 0.65, U_∞ = 90 m s^{-1}. Occurrence of Stage A (0–4 s), B (4–20 s) and C (20–30 s). 2) T_a = -3°C, ϕ = 0.65, U_∞ = 180 m s^{-1}. Occurrence of Stage A (0–1 s), B (1–11 s), C (11–16 s) and D (16–30 s). 3) T_a = -6°C, ϕ = 0.65, U_∞ = 90 m s^{-1}. Occurrence of Stage A (0–12 s) and B (12–30 s). 4) T_a = -6°C, ϕ = 0.65, U_∞ = 180 m s^{-1}. Occurrence of Stage A (0–2 s), B (2–15 s), C (15–25 s) and D (25–30 s). 202

5.17 Variation in freezing fraction λ with changes in U_∞ for 100 s. . 203

5.18 Ice accretion versus air velocity. 1) T_a = -3°C, ϕ = 0.65, β = 0.5. Occurrence of Stage A (0–4 s), B (4–20 s) and C (20–30 s). 2) T_a = -3°C, ϕ = 0.65, β = 1. Occurrence of Stage A (0–1), B (1–13 s), C (13–18 s) and D (18–30 s). 3) T_a = -6°C, ϕ = 0.65, β = 0.5. Occurrence of Stage A (0–12 s) and B (12–30 s). 4) T_a = -6°C, ϕ = 0.65, β = 1. Occurrence of Stage A (0–2 s), B (2–18 s), C (18–28 s) and D (28–30 s). 204

5.19 Variation in freezing fraction λ with changes in β for 100 s. . . 205

5.20 Ice accretion versus angle of attack. 1) T_a = -3°C, ϕ = 0.65, AoA = 0∘. Occurrence of Stage A (0–4 s), B (4–20 s) and C (20–30 s). 2) T_a = -3°C, ϕ = 0.65, AoA = 10∘. Occurrence of Stage A (0–4 s), B (4–20 s) and C (20–30 s). 3) T_a = -6°C, ϕ = 0.65, AoA = 0∘. Occurrence of Stage A (0–12 s) and B (12–30 s). 4) T_a = -6°C, ϕ = 0.65, AoA = 10∘. Occurrence of Stage A (0–12 s) and B (12–30 s). 207

5.21 Variation in freezing fraction λ with changes in AoA for 100 s. 208

5.22 Ice growth due to glaze ice model [5] at T_a = -3°C and ϕ = 0.96. 210

5.23 Ice growth due to glaze ice model [5] at T_a = -6°C and $\phi = 0.96$. 210

5.24 Overall ice height variation with changes in ϕ at -3°C ($\circ$), -3.5°C ($+$), -4°C (x), -4.5°C ($\square$), -5°C ($\diamondsuit$), -5.5°C ($\triangle$), -6°C ($\bigtriangledown$), -6.5°C ($\triangleright$), -7°C ($\star$) and -7.5°C ($*$). 212

6.1 Schematic of two-dimensional ice accretion on an aerofoil. . . . 223

6.2 Schematic of non-dimensional ice accretion with no glaze formation. 232

6.3 Non-dimensional saturation flux R^* for different values of time scale ratio ε. 234

6.4 Non-dimensional saturation flux R^* for different values of ϕ_i. . 235

6.5 Non-dimensional saturation flux R^* for different values of ε. $\phi_i = 0.5$, $T_s = 268\,\mathrm{K}$, $b = 2\,\mathrm{mm}$. λ is varied from 0.1 to 0.9 across $\tilde{x}$. 238

6.6 Non-dimensional saturation flux R^* for different values of T_s. $\phi_i = 0.5$, $\varepsilon = 1$, $b = 2\,\mathrm{mm}$. λ is varied from 0.1 to 0.9 across $\tilde{x}$. 239

6.7 Non-dimensional saturation flux R^* for different values of b. $\phi_i = 0.5$, $\varepsilon = 1$, $T_s = 268\,\mathrm{K}$. λ is varied from 0.1 to 0.9 across $\tilde{x}$. 240

6.8 Non-dimensional number γ for different values of b. $\lambda = 0.5$, $\dot{M} = 0.27\,\mathrm{kg\,m^{-2}\ s^{-1}}$. 241

6.9 The latent heat-conduction ratio γ for different values of b. T_s = 268 K, $\dot{M} = 0.27\,\mathrm{kg\,m^{-2}\ s^{-1}}$. 242

6.10 Two-dimensional ice height and profile at 90 s, $T_s = 266\,\mathrm{K}$ and $\phi_i = 0.49$. Red line represents rime ice and blue line represents glaze ice. 243

6.11 Two-dimensional profile of ϕ_w and α at 90 s, $T_s = 266\,\mathrm{K}$ and $\phi_i = 0.49$. Green line represents ϕ_w and black line represents saturation level α. 244

6.12 Two-dimensional ice height and profile at 90 s, $T_s = 266\,\mathrm{K}$ and $\phi_i = 0.38$. Red line represents rime ice and blue line represents glaze ice. 245

6.13 Two-dimensional profile of ϕ_w and α at 90 s, $T_s = 266\,\mathrm{K}$ and $\phi_i = 0.38$. Green line represents ϕ_w and black line represents saturation level α. 246

6.14 Two-dimensional ice height and profile at 90 s, $T_s = 266$ K and $\phi_i = 0.49$. Red line represents rime ice and blue line represents glaze ice. 247

6.15 Two-dimensional profile of ϕ_i and α at 90 s, $T_s = 266$ K and $\phi_i = 0.49$. Green line represents ϕ_w and black line represents saturation level α. 248

6.16 Two-dimensional ice profiles for a) No runback flux; b) 100% electro-thermal mat efficiency; c) 75% electro-thermal mat efficiency; and d) 50% electro-thermal mat efficiency. 250

6.17 Two-dimensional saturation levels and liquid fraction profiles for a) No runback flux; b) 100% electro-thermal mat efficiency; c) 75% electro-thermal mat efficiency; and d) 50% electro-thermal mat efficiency. 251

List of Tables

1.1 Values of important meteorological parameters contributing to rime and glaze ice formation. 36

2.1 Preliminary results of centrifuge tests on SS 304 substrates. . . 66

2.2 Surface roughness parameters of all three substrates. 72

2.3 Contact angle parameters of three different substrate types. . 74

2.4 Detachment speeds and adhesion strength at different preparation and ambient temperatures for three different substrates. 77

2.5 Percentage influence of preparation and ambient temperatures on adhesion strength for three different substrate types from base conditions of T_p = -5°C, T_a = -5°C [6]. * refers to a value that lies within the error limits of adhesion strength. 83

2.6 Comparison of results with Laforte and Beisswenger (2005) [7]. 84

3.1 Coating label and its respective composition, contact angle and surface roughness properties (A-G). A single uncoated sample characteristics are also shown. 95

3.2 Coating label and its respective composition, contact angle and surface roughness properties (H-N). 96

3.3 Properties and their variation across 20 uncoated substrates illustrating the repeatability of each measurement. 99

3.4 Summary of test results for Coating A-N. 116

3.5 Coating decay rates and retained icephobicity values of Coatings A—N. *Extrapolated values since test results from first cycle were invalid. 121

4.1 Test data for the uncoated and coated substrates. 146

4.2 Contact angle parameters for all substrates. 148

4.3 Freezing sequence of water droplet on uncoated and coated surface at -10°C plate temperature. 149

4.4 Overall ranking of the coatings. 153

5.1 Ice type variation with droplet freezing fraction, λ. 184

5.2 Ice height comparison between author's model and glaze ice model [5]. 213

5.3 Ice height comparison between author's model and experimental data. *Experimental data in comparison to author's model. 215

A.1 Summary of results for coating A from test period. MF stands for mould failure. PD stands for partial detachment. 259

A.2 Summary of results for coating B from test period. MF stands for mould failure. PD stands for partial detachment. 260

A.3 Summary of results for coating C from test period. MF stands for mould failure. PD stands for partial detachment. 261

A.4 Summary of results for coating D from test period. MF stands for mould failure. PD stands for partial detachment. 262

A.5 Summary of results for coating E from test period. MF stands for mould failure. PD stands for partial detachment. ND stands for no detachment at maximum speed of 4500 rpm. . . 263

A.6 Summary of results for coating F from test period. MF stands for mould failure. PD stands for partial detachment. ND stands for no detachment at maximum speed of 4500 rpm. . . 264

A.7 Summary of results for coating G from test period. MF stands for mould failure. PD stands for partial detachment. ND stands for no detachment at maximum speed of 4500 rpm. . . 265

A.8 Summary of results for coating H from test period. MF stands for mould failure. PD stands for partial detachment. 266

A.9 Summary of results for coating I from test period. MF stands for mould failure. PD stands for partial detachment. 267

A.10 Summary of results for coating J from test period. MF stands for mould failure. PD stands for partial detachment. 268

A.11 Summary of results for coating K from test period. MF stands for mould failure. PD stands for partial detachment. 269

A.12 Summary of results for coating L from test period. MF stands for mould failure. PD stands for partial detachment. 270

A.13 Summary of results for coating M from test period. MF stands for mould failure. PD stands for partial detachment. 271

A.14 Summary of results for coating N from test period. MF stands for mould failure. PD stands for partial detachment. 272

Nomenclature

Symbol	Description	Units/Value
d	Droplet Size	μm
T_a	Ambient Temperature	K
T_f	Freezing Temperature	K
T_s	Substrate Temperature	K
T_d	Droplet Temperature	K
ρ_g	Density of Glaze Ice	$917\,\mathrm{kg\,m^{-3}}$
ρ_w	Density of Water	$1000\,\mathrm{kg\,m^{-3}}$
g	Gravitational Acceleration	$9.81\,\mathrm{m\,s^{-2}}$
ρ_a	Liquid Water Content	$\mathrm{kg\,m^{-3}}$
U_∞	Free Stream Air Velocity	$\mathrm{m\,s^{-1}}$
ρ_r	Density of Rime Ice	$\mathrm{kg\,m^{-3}}$
β	Collection Efficiency	
A	Wing Surface Area	$\mathrm{m^2}$

A_h	Electro-thermal Mat Surface Area	m^2
k_i	Thermal Conductivity of Ice	$2.18\,\mathrm{W\,m^{-1}K^{-1}}$
k_w	Thermal Conductivity of Water	$0.571\,\mathrm{W\,m^{-1}K^{-1}}$
x_s	Sublimation Coefficient	$11.65\,\mathrm{m\,s^{-1}}$
a	Aerodynamic Heating Constant	0.895
c_a	Specific Heat Capacity of Air	$1014\,\mathrm{J\,kg^{-1}K^{-1}}$
H_{aw}	Air-Water Heat Transfer Coefficient	$500\,\mathrm{W\,m^{-2}K^{-1}}$
L_f	Latent Heat of Fusion	$334000\,\mathrm{J\,kg^{-1}}$
c_w	Specific Heat Capacity of Water	$4220\,\mathrm{J\,kg^{-1}K^{-1}}$
x_e	Evaporative Coefficient	$9.53\,\mathrm{m\,s^{-1}}$
e_0	Evaporative Function Derivative	$44.4\,\mathrm{Pa\,K^{-1}}$
c_i	Specific Heat Capacity of Ice	$2108\,\mathrm{J\,kg^{-1}K^{-1}}$
x, y, z	Cartesian Coordinate System	
ARF	Adhesion Reduction Factor	

Chapter 1

Introduction

Ice formation on an aircraft in flight reduces the aerodynamic control, fuel efficiency and lift characteristics of the system [8]. This is due to the fact that, the presence of rough ice structures near the leading edge can disrupt the laminar flow pattern, thereby causing extra fuel usage and inducement of stall. Aerodynamic imbalance, for example, can also occur due to unequal ice distribution and formation on both wings. The development of a smart anti-ice coating is considered as a crucial step in reducing the high power usage required by electro-thermal mats which melt ice formed at the leading edge of the wing surface. Electro-thermal mats operate only near the leading edge due to their power requirement and bulk, so coatings present an

opportunity to reduce icing over all parts of the wing. The primary motivation of this work is to aid in the development of such a coating through understanding, modelling and experimentally verifying the physical process of ice accretion. Accretion models to date have treated heat transfer processes around the solidification front very simplistically. The author seeks to incorporate mixed ice physics into models of the solidification process. Overall, the additional development of a smart anti-ice coating will aim to increase flight safety, economy and reduce greenhouse gas emissions to the atmosphere by maintaining a smooth flow over the wing.

1.1 Ice Accretion on Aerofoils

An aircraft in flight under given atmospheric conditions (Table 1.1), is subject to ice accretion or formation of ice on its surface [9]. This phenomena occurs due to the impingement and subsequent freezing of supercooled water droplets (droplets which exist in the liquid form below 0°C) present in the clouds onto the wing surface and is greatly influenced by the external shear force exerted by the air flow. Icing usually occurs between 3000-6000 metres above sea level [10]. Some of the crucial regions of icing on an aircraft occur on the engine nacelles, propellers, wind shields and hubs on fixed-wing

aircraft [8]. However, the majority of incoming droplets impact the leading edge of the wings and the empennages owing to the significantly greater surface area of capture, relative to the direction of impingement. Gent et al. (2000) [11] reported that even minor quantities of ice accumulation can cause a significant reduction in aerodynamic stability, maximum lift capacity and performance. This inevitably contributes to excess fuel requirements and a subsequent increase in carbon dioxide emissions in the atmosphere.

Type of Ice	ρ_a ($\mathrm{g\,cm^{-3}}$)	d (μm)	T_∞ (0°C)	Event Duration
Rime	0.3−0.7	10−20	−40 to −10	Days
Glaze	0.7−1.3	20−80	−10 to 0	Hours
Reference	[10]	[10]	[8]	[12]

Table 1.1: Values of important meteorological parameters contributing to rime and glaze ice formation.

The overall effect of icing depends strongly on the type of icing. The ISO 12494 Standard classifies three main categories of in-flight icing based on the process of formation: hoar frost, precipitation icing and in-cloud icing [9]. The first two occur less commonly and pose a significantly reduced

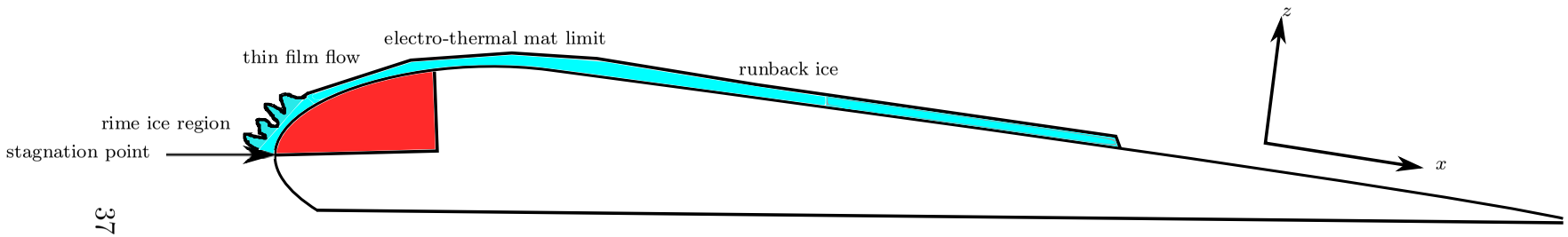


Figure 1.1: Cross-sectional view of aircraft wing in flight showing different regions of liquid movement and ice formation.

aviation hazard in comparison to in-cloud icing because the ice formed in both cases is of a lower strength and density (approximately 40-50% less than in-cloud ice in both cases respectively). In-cloud icing can itself be classified as glaze, rime or a mixture of the two [13]. Rime ice is the most commonly occurring (around 70–75%) followed by mixed 1.5 and then finally glaze ice [10]. Figure 1.1 shows a schematic of the liquid movement on an aircraft wing in flight highlighting the probable regions of rime and glaze ice formation. When supercooled droplets impact the wing surface and freeze almost immediately, an opaque/white, eccentric-shaped (randomly shaped) ice formation occurs that has a significant amount of air trapped within the solid structure [12]. This is known as rime ice (Figure 1.2) and is critically less hazardous to aviation due to its poor adhesion strength, low density and location of occurrence along the protected section of a wing. Enzmann et al. (2011) [14] reported that the size of porous voids calculated from graupel samples varied from 2μm to 18μm. Carras and Macklin (1975) [15] reported for dry growth (rime) accretion, the pore sizes varied from 1μm to 4μm. As Varela et al. (2005) [16] state "The accumulation of droplets can form porous accretions with internal channels that are interconnected"; along with the presumptive size of porous space, this will form an important basis for the exploration of mixed ice accretion in Chapter 5 and 6. When supercooled droplets impact the surface and do not freeze immediately but run back



Figure 1.2: Photograph of rime ice accretion on fuselage nose of an aircraft [1].

along the wing in the form of a thin liquid film; a clear, dendrite-shaped ice occurs that has minimum air trapped in between the crystal lattice [8]. This is known as glaze ice and forms the primary concern of this research owing to its hazardous effect on aircraft aerodynamics and flight safety. Chen and Morris (2011) [17] reported that glaze icicle growth can also exhibit a different shape comprising of distinct wavy ridges during accretion.

Due to the difference in the amount of entrapped air in the solid structure, glaze ice has a higher density of $\sim$900 kg m^{-3} and above while the density of rime ice can vary from 200–900 kg m^{-3} [12]. Table 1.1 exhibits the influence of meteorological parameters on the type of formation of ice.

From this data it is apparent, that for all parameters except event duration (i.e. ρ_a, d and T_∞), glaze ice formation requires higher values as compared to rime ice. Politovich (2000) [18] reported from experimental data that even at lower values of liquid water content, glaze ice formation is still prominent if large droplets and warmer temperatures exist as parameters beyond a critical threshold.

Although the formation of glaze ice can have hazardous effects on aerodynamic stability, both fixed-wing and rotor-wing aircraft are currently fitted with numerous anti-icing and de-icing devices to aid in mitigating the problem. De-icing refers to the removal of already formed ice while anti-icing enlists techniques preventing or inhibiting the buildup of ice [8]. In the review of the most effective methods to mitigate ice accretion, Ryerson (2011) [19] listed electro-thermal mats as a popular technique in current industrial practice. However, solely using electro-thermal mats is unfeasible, owing to the large electricity consumption ($\sim 10^5$ W) and the location of this de-icing device that remains close to the leading edges leaving a large portion of the wing vulnerable to ice buildup [20]. A combination of the above, along with thermally receptive nano-scale icephobic coatings, is mooted as the future of in-flight ice mitigation. Significant research is currently being conducted into optimizing the capacity of the mats and increasing the durability and

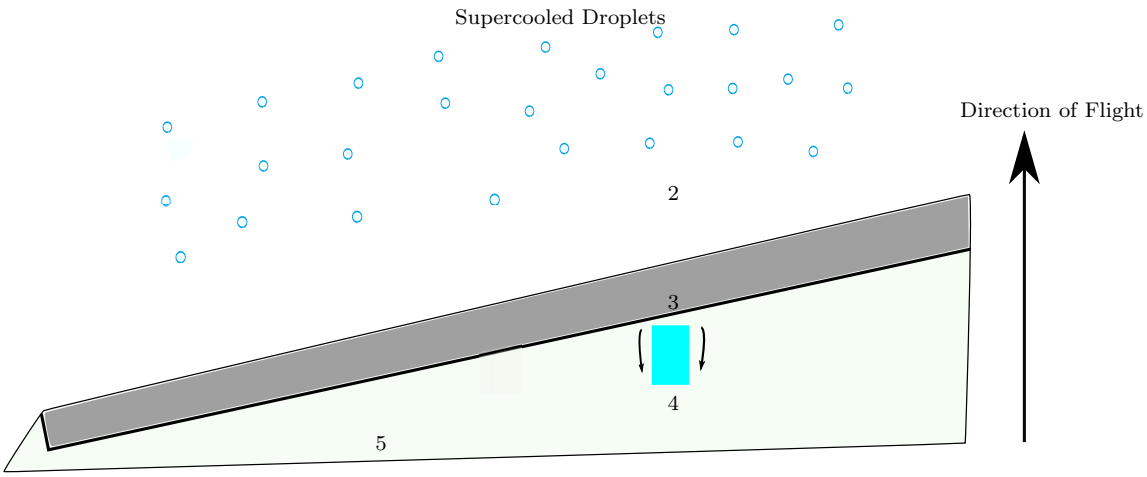


Figure 1.3: Aerial view of an aircraft wing showing separate regions of glaze and runback ice formation.

effectiveness of the nano-coatings [21].

Although most authors refer to runback and glaze ice in the same sense, it will be useful to distinguish between the two for the purpose of our research. Previous work considering runback icing [22] has considered impinging supercooled water droplets as the main source of fluid from which primary glaze runback ice is formed. However, we are interested in the formation of secondary glaze runback ice from melt water generated by the electro-thermal mats. From now on, for all practical purposes, this type of ice formation shall be defined as "runback ice" while glaze ice (figure 1.4) shall retain the definition explained in the previous section as a primary form of ice accretion.

Figure 1.3 shows an aerial view of an aircraft wing in flight denoting the separate regions of glaze and runback ice formation. The region in grey denotes the average section of a wing covered by the electro-thermal mats and the blue circles show the array of incoming supercooled droplets. 2) denotes supercooled droplets on the smaller scale ($\simeq$20 μm) that become entrained in the incoming air field and form glaze ice on the curved surface of the leading edge, close to the stagnation point. If allowed to grow uninhibited, they form a single/double horned structure on freezing [23]. 3) denotes larger droplets (50$-$80 μm) that impact the wing beyond the curved surface of the leading edge and form glaze ice in the region bounded by the electro-thermal mats. 4) denotes the glaze ice that on melting of ice near the leading edge, refreezes after flowing as a thin film back along the wing surface (denoted by light blue in the figure). Broeren et al. (2010) [24] reported that this runback ice forms a ridge-type shape disrupting laminar air flow. 5) denotes the largest supercooled droplets ($\geq$100 μm) that due to their inertia, impact the wing directly beyond the electro-thermal mats. The nano-coatings form the sole prohibitive measure to ice growth in this region.



Figure 1.4: Close-up photograph of glaze ice accretion after 22.5 minute warm-hold spray at the NASA Glenn Icing Research Tunnel [2]. The flow of the water film is from right to left.



Figure 1.5: Mixed ice as a combination of glaze and rime from experiments at NASA-Lewis Research Center [3].

1.2 Ice Adhesion Testing

Kasaai and Farzaneh (2004) [25] extensively review various methods for evaluating ice adhesion strength. Approaches include a parallel plate type shear rig experimental technique developed by the NASA Lewis Icing Research Tunnel [26], a plunger and pressure tube arrangement [27], destructive wedge testing using weights [28], a modified Zero-Degree cone test [29] and an electro-magnetic shaker system [7]. However, most of these devices are complex and exhibit high variability in their measurements. The approach described here draws upon the design and strategy previously implemented by Laforte and Beisswenger (2005) [7] and Kulinich and Farzaneh (2009) [30], employing a spinning centrifuge to determine the rotation rate at which the centrifugal acceleration overcame the ice adhesion strength. This technique is simple and significantly leads to a relatively low variability in measurements (18%) [30], and further permits atmospheric icing temperature conditions to be replicated by deploying the system within an environment-controlled chamber.

Using the centrifuge technique, several researchers [7, 30, 31] were able to obtain the influence of contact angle and surface roughness parameters on the adhesion strength of ice. The findings indicate, that low contact angle

hysteresis and surface roughness contribute towards reducing ice adhesion. Saito et al. (1997) [32] mentioned that beyond a limit, high surface roughness contributes to lowering ice adhesion strength due to the incorporation of air bubbles at the ice-surface interface. Momen et al. (2015) [33] also studied the effect of atmospheric icing conditions such as liquid water content and droplet size on adhesion strength. They found that lower liquid water content and smaller droplet size reduced adhesion strength. However, the quantified influence of altering temperature conditions on the adhesion strength of ice has yet to be fully understood.

In Chapter 2, we measure the repeatability of the centrifuge experiment and determine the effect of temperature on the adhesion strength.

1.3 Icephobic Coatings Design

Ice accretion is problematic also in other engineering applications such as power cables, radio masts or wind turbines [34]. Research into finding icephobic coatings has been active since the 1960's [35], but several issues persist: in particular, the durability of coatings and the practicalities of applying to extensive areas on structural surfaces exposed to rugged environments. Several materials have been proposed as icephobic coatings including polytetraflu-

oroethylene (PTFE)[36, 37], fluorinated polymethylsiloxane and octavinyl-polyhedral oligomeric silsesquioxanes (OVPOSS) [38, 39, 36], Al_2O_3 nanoparticle in silicone rubber solution [40] and sol-gel coatings containing tetraethylorthosilicate (TEOS) and 3-glycidylpropyl trimethoxy silane (GPTMS) [27]. By investigating this range of coatings, we aim to add further evidence to the debate over the correlation between icephobicity and hydrophobicity [41, 42, 43]. In particular, we look at the contact angle hysteresis for a surface [44, 37, 38, 36] to evaluate its link to icephobicity.

In Chapter 3 and 4, we investigate the icephobicity of 14 nanocoatings by repeating ice adhesion tests and measuring the effect of ice removal on contact angle parameters; and measuring the freezing time of water droplets on a coated surface at sub-zero temperatures.

1.4 Ice Accretion Modelling

The ice accretion process is not straightforward, with different types of ice growing under different environmental conditions. Rime ice results from a relatively simple heat transfer process, whereby supercooled water droplets freeze instantaneously on impact with a very cold wing surface [45, 46, 47, 48, 49]. This process creates a relatively low density porous ice, with a distinc-

tive white appearance. In contrast, glaze ice typically grows at temperatures closer to the melting point via a Stefan-type boundary condition, to form a dense and translucent ice layer. Glaze formation requires the presence of water, either due to partial freezing of the supercooled water droplets, or as *runback* water as the electrothermal systems in the leading edge melt any ice structures accreted there. In practice, the ice that forms on an aircraft wing tends to be a combination of rime and glaze ice; potentially with some retained pockets of air and described as *mixed ice* [3]. From Figure 1.5, we can see a combination of clear and rime ice from actual experiments on an aerofoil in the NASA Lewis Icing Research Center. The structure and method of formation of this mixed ice will be explored using a theory of partial freezing of droplets on impact with the aerofoil in Chapter 5 and 6.

Commercial icing codes such as LEWICE, TRAJICE, ONERA and ICECREMO code [22, 50, 51, 5, 52] have been developed over a number of years. The latter considers the dynamic behaviour of the runback water film on the accretion rate and will form a basis for our analysis. The ICECREMO code modelled solidification of the runback water film, which resulted in a wider applicability of the model to different icing conditions. All of these models however tend to over-predict ice accretion, leading to potential energy wastage through over-use of the electro-thermal de-icing system. A limitation is these do not differentiate between different ice types - an important

consideration when considering adhesion to possible wing coatings.

In Chapter 5, we develop a one-dimensional icing model describing four stages of accretion and the presence of mixed ice, a combination of rime and glaze.

The flow of the melted glaze ice moving back along the wing surface can be classified as a thin film flow. Since the ratio of height-to-length is extremely small and the film possesses a very low Reynold's number, one would assume that the influence of surface tension and viscosity are significant near the stagnation point. In comparison though to the magnitude of the shear force, this effect is greatly lessened further downstream where airspeeds are high and film thickness may have developed. Surface tension opposes the film motion and aims to reduce the surface area by coalescing the water into beads or rivulets. Hansman and Turnock (1989) [53] reported that increasing surface tension contributed to an enhanced surface roughness even leading to horned ice formations on the wing surface. This is one of the major contributing factors to the overall shape of the ice structure but not the movement of the film as explained above. It is worth noting here as well that aircraft cruising speed can have significant effect on the stagnation temperature and at higher altitudes and faster speeds, assumptions made regarding a constant ambient temperature may not hold true. For this

purpose, the scope of this research focuses on scenarios relating to slower speeds ($\leq$ Mach number $M_r = 0.2$) and lower altitudes. For example, using the static temperature T_{st} equation [54], we get

$$T_{st} = T_a \left[1 + \frac{(\chi - 1)}{2} M_r^2)\right], \tag{1.1}$$

where χ is the ratio of specific heats (1.4 for dry air). Taking $T_a =$ 268 K, for $M_r = 0.5$ and 0.75, we get $T_{st} = 281.4$ K and 298.15 K respectively. Thus we appreciate the effect of velocity at higher speeds on the temperature surrounding the aerofoil.

An important reference relating to glaze ice formation is the stagnation point which can be defined as the point along the leading edge of the wing where the velocity of the incoming air field is zero [55]. Experimental data has revealed that glaze ice occurs in three distinct zones of ice formation: smooth, rough and runback [50]. The latter zone will be renamed as the "rivulet" zone to avoid confusion with our predefined term for runback ice. The smooth zone is deemed to form due to the effects of surface tension and viscosity near the stagnation point while the rivulet zone develops due to the presence of a non-impingement region on the wing. Figure 1.4 which exhibits the close-up photograph of glaze ice accretion after a 22.5 minute

warm-hold spray at the NASA Glenn Icing Research Tunnel, correlates these findings. The warm-hold term refers to ambient temperatures of close to 0°C in the experimental setup. Towards the start of the accretion (far right of picture), a smooth zone can be seen followed by a majority occupying rough zone (characterised by the tall, dendrite peaks) which mixes with the rivulet zone up to a point; before a clear rivulet zone develops (far left of the picture).

The zoning of glaze ice was initially recorded in the findings of Yamaguchi and Hansman (1992) [56] who studied the effects of ice surface roughness on the heat transfer rate and the subsequent ice accretion rate. The authors implied from their findings, that the transition point from smooth to rough ice occurred at the same point as the transition from the laminar to turbulent air boundary layer. Also, the former was recorded to move towards the stagnation point with an increase in time with the rough zone enveloping the smooth zone for a cylindrical substrate. This upstream movement of roughness with time, may be explained by the flow of impinged droplets back from the rough to the smooth zone, sliding along from the peaks of sloped icicle-shaped formations. Since the smooth zone occurs, only at and near the stagnation point, it will be interesting to see whether runback ice formation has a smooth zone since no stagnation point occurs beyond the

electro-thermal mat region. Similarly, another question arises whether glaze ice formations have sufficient time to develop a rivulet zone before melting in the electro-thermal mat region. Our experiments will provide an interesting comparison to the above findings and will hope to validate our predictions of the model.

The effect of film thickness on the heat transfer process and ice accretion rate has been studied extensively in literature [50, 51, 57, 58]. More recently, Yanxia et al. (2010) [59] concluded from a study that increasing shear stress is accompanied by an increase in the flow of runback water which subsequently increases the overall ice accretion rate.

There appears to have been significant work done on thin film flow but, when it comes to mixed ice and the particular condition of rime growing above glaze with water flowing through the porous spaces, this is yet to be fully explored. In Chapter 6, we develop a model to explain the dimensional and non-dimensional implications of such a flow within a porous media driven by overlying shear.

This project forms part of the ICECOAT Project, under the umbrella of CLEANSKY, aimed at developing a novel anti-ice coating on aircraft wings. The major industrial partner in this scheme is a French company Das-

sault Aviation. Our particular work relating to the project encompasses the testing of ice adhesion strength. The implementation and experimental evaluation of an icing code incorporating mixed ice physics forms an additional part to the adhesion tests which will be included in this thesis. This task involves understanding a key heat transfer process which is greatly influenced by the boundary layer of air surrounding the aircraft wing. Other work packages encompass the design of a fully functional wind tunnel (only the third in the UK!) and the manufacture of the nano-coatings themselves. The aim of this project is to develop a mathematical model and a laboratory experiment to describe the effect of glaze icing on aerofoils during flight.

The main objectives of this PhD are:

1. To identify key ice adhesion properties for minimization of icing through mathematical model development, experimental investigation and its numerical implementation.

2. To develop instrumentation for the physical characterisation of ice adhesion and accretion properties and implement within a laboratory experiment.

3. To test the effectiveness of nano-coatings in preventing ice accretion on aerofoils in flight and use the results from 1. to determine likely ice types at different atmospheric conditions.

Chapter 2

Design and Calibration of a Centrifuge Ice Adhesion Test

2.1 Introduction

This chapter reports on the specification and operation of a centrifuge device designed to measure the reduction in ice adhesion strength of icephobic coatings. The principle behind the testing mechanism and repeatability tests of the apparatus are detailed.

The purpose of our ice adhesion tests is to determine the effectiveness of smart icephobic nano-coatings. Techniques implemented to measure

ice adhesion strength include a plunger and pressure tube arrangement [28], destructive wedge testing using weights [29], modified Zero-Degree cone test [27] and an electro-magnetic shaker system [60]. Some experiments however exhibit difficulty in maintaining constant force [60] and lead to high variability in results. Our experimental setup is based on that of Kulinich and Farzaneh (2009) [30]. In their research, glaze ice samples were produced in a wind tunnel using supercooled droplets sprayed from a nozzle onto a coated substrate. The system employed a centrifuge technique for measuring the adhesion strength at the point of detachment of glaze ice as a measurement of reaction force

$$F = mr\,\omega^2, \tag{2.1}$$

where m is the mass of ice, r is the centrifuge beam radius and ω is the speed of rotation in $\mathrm{rad\,s^{-1}}$. The shear stress τ applied to the sample can be calculated as F divided by the de-iced area A. A coating which provides the lowest rotation speed for glaze ice detachment will be more icephobic than a corresponding coating with detachment at a higher rotation speed

Figure 2.1 shows a schematic of our experiment drawn to scale, with rotor length of 19.25 cm and width 2 cm. The size of the steel drum was constrained by the dimensions of the environmental chamber (1980 x 1380 x 2330 mm) and comfortable maneuvering of attaching/detaching the samples

within the chamber. Using the values for adhesion strength from Laforte and Beisswenger (2005) (see Table 2.6), we initially chose a MOOG brushless servo-motor with top speed of 6000 rpm. A previous motor had encountered severe malfunctioning due to moisture exposure and was discarded after trial for 18 months. After modification of the MOOG motor to ensure no exposure to moisture and due to enhanced vibration of the environmental chamber at higher rotational speeds, the motor top speed was capped at 4500 rpm. The substrate was attached to one end of the beam (balanced by a counter-weight) and rotated at steadily increasing speeds until detachment, recorded by an accelerometer mounted on the wall of the device and corroborated with a microphone positioned below the drum base.

As Kulinich and Farzaneh (2009) [30] and Laforte and Beisswenger (2005) [7] showed, this centrifuge technique is relatively repeatable and simple to perform, showing lower standard deviation (18%) in adhesion measurements than the alternative methods recording upto 300% in variation [7]. The effectiveness of the icephobic coating is indicated by an Adhesion Reduction Factor (ARF), which is calculated as the ratio of shear stress for an uncoated surface τ_u to shear stress for a coated surface τ_c. Uniformity in the glaze ice samples and reducing contamination of the substrate is key to ensuring repeatable results. The experiment has been carried out under sim-

ulated atmospheric icing conditions in an environmental chamber to ensure applicable results and to provide a controlled environment. The atmospheric conditions recreated are those favouring the formation of runback icing, using an ALPHA 1550-40H Environmental Test Chamber manufactured by Design Environmental. This has a test volume of 1550 litres with controllable temperature and humidity levels. The system has a temperature range (θ) of -40 $< \theta <$ +180°C ± 0.3°C and a humidity range of 10–98%, falling comfortably within the range for runback ice formation and maintaining excellent stability. When the rotor spins at high speeds, there is a possibility for the air temperature within the steel drum to rise due to frictional resistance of air. The maximum linear speed calculated at 4500 rpm equals $\sim 90\,\mathrm{m\,s^{-1}}$. This gives us $M_r = 0.26$. At M_r values lower than or equal to 0.2, the difference between stagnation temperature and ambient temperature is negligible (in the order of 2°C). As most coatings exhibit adhesion strengths within this range as will be seen in Chapter 3, our assumption holds true. Either ways, the key focus is the ARF to determine the true icephobic effectiveness of the coating. It is also worth mentioning here that the thermal expansion coefficient of ice is 50 x 10^{-6} deg^{-1}; a significant value which may cause the adhesion strength of ice to be affected by minor temperature changes in the surrounding.

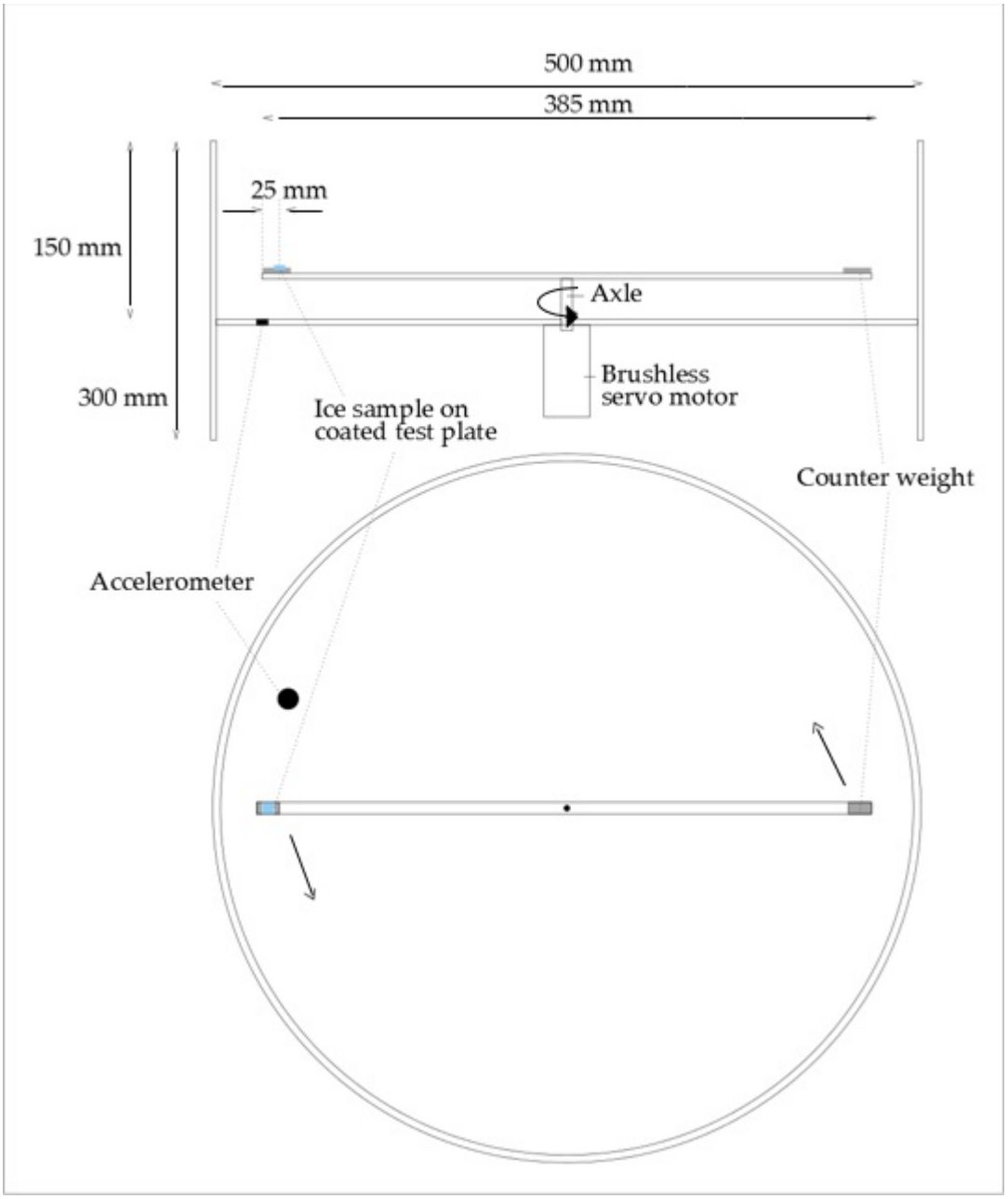


Figure 2.1: Detailed schematic of centrifuge set-up for the adhesion tests.

2.2 Design Specifics

The constructed centrifuge testing system comprises a stainless steel cylindrical drum, 300 mm deep, diameter 500 mm. A steel floor is mounted 150 mm below the top of the drum. A detachable carbon fibre reinforced polymer (Easycomposites prepreg carbon fibre flat sheet) rotor has dimensions 385 x 20 x 3 mm (see figure 2.1) and mounts to the motor shaft via a stiff coupling. The sample substrate plates attached to either end of the rotor are 50 x 20 x 3 mm with counter sunk holes to take M4 thread 12 mm screws (see figure 2.2). The substrate material used in this section is stainless steel 304. The rotor is driven by a MOOG Brushless Servo Motor G403-2053A. This motor has been treated to optimise performance at sub-zero temperatures, avoiding condensation within the motor housing and using a resolver control. Additionally, an accelerometer (RS-online 759-1994 70g accelerometer 22kHz iMEMs CLCC8) is mounted in the drum floor to detect ice detachment and a standard headset microphone is also placed underneath the drum to corroborate the time of detachment. The accelerometer voltage output is viewed via an NI USB6212 DAQ system.

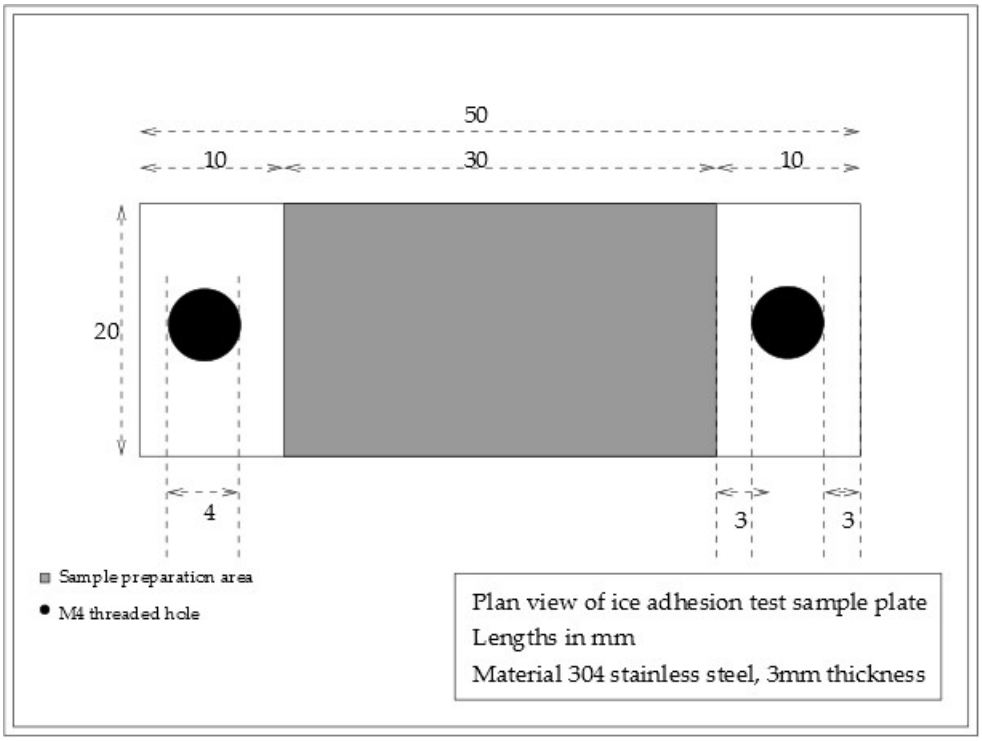


Figure 2.2: Schematic of stainless steel drum used for adhesion tests.



Figure 2.3: Photo of ice attached to substrate inside environmental chamber, Z.Janjua.

2.3 Method

The test procedure consists of two steps: Ice sample preparation and adhesion stress measurements.

2.3.1 Ice sample preparation

To manufacture repeatable, uniform glaze ice samples (e.g. figure 2.3), the following procedure was adopted.

1. The sample substrate plate was attached to the carbon fibre reinforced polymer rotor with a counterweight fixed to the other end. The counterweight is a substrate, with a mass welded on to balance the weight of the sample ice plus substrate on the other end of the rotor. This is used to prevent undesired vibrations in the rotor.

2. The arm was placed upside down in the Environmental Test Chamber at a selected freezing temperature. The substrate plate was attached to a $\sim$2 ml silicone mould filled with de-ionised 18 MΩ water and left to freeze for 24 hours. The water was stored in an air-tight plastic container to ensure minimal gas absorption. The pore size of the filter is 0.2μm.

2.3.2 Adhesion stress tests

To measure the adhesion shear stress of the ice sample to the substrate plate, the centrifuge device was operated as follows.

1. The ambient temperature was set to the desired value, if different from the preparation temperature.

2. The rotor was coupled to the motor shaft and the silicone mould removed from covering the sample. The steel drum cover was fastened securely by 4 clips and the test chamber closed.

3. Motor drive software, data viewing for the accelerometer response and recording for the microphone signal were initiated.

4. Motor acceleration was set to a fixed value of $30\,\mathrm{rev\,min^{-1}s^{-1}}$ from 0 rpm to the motor's maximum speed of 4500 rpm. The drive was programmed with a deceleration rate of 200 rpm/s. This low acceleration rate was selected to minimize the effect of time measurement error and to create a smooth, stable test.

5. The motor was started simultaneously with a stop watch (± 0.5 s).

6. When the accelerometer showed a sharp peak, corresponding to

ice detachment, the stop watch was paused and the motor brake applied. The rotor decelerated to a stop and the steel cover opened.

7. Detachment time from the accelerometer signal was corroborated with the audible recorded microphone response.

8. The rotation rate at detachment is determined from the product of the acceleration rate and detachment time. This is further corroborated with readouts of instantaneous motor shaft speed in the motor control software.

9. The adhesion shear stress can now be evaluated for the sample and the test repeated using the same rotor and counterweight (equation 2.1).

2.4 Repeatability Tests - Coffee Bean Mould

This section details the initial test trials of the centrifuge setup to measure the adhesion strength of ice samples formed in a coffee bean mould on stainless steel 304 3 mm substrates (figure 2.2). These tests sought to identify the optimal ice preparation and ambient temperature for the centrifuge technique and to inform the final test protocols for the icephobic coatings. In this regard, we define two separate temperature conditions involved in the

adhesion testing of ice: "preparation temperature" (T_p) and "ambient temperature" (T_a). The preparation temperature refers to the temperature of the surroundings during the freezing process of the glaze ice samples. Ambient temperature on the other hand, refers to temperature of the surroundings at the time of the centrifugal detachment test.

To quantify sources of error, the steel substrate plates machined in an identical manner, were weighed. The steel substrate plate masses were satisfactorily uniform with an average of 21.09 g $\pm$ 0.81%. When weighed also with grown ice samples, the ice sample mass was found to be 1.31 $\pm$ 0.03 g at -5$^{\text{deg}}$C freezing temperature, a relative error of 2.24%. The ice was weighed by moving the weighing machine inside the environmental chamber. To evaluate the performance of the centrifuge adhesion shear stress measurement device, a series of tests were run under nominally identical conditions. 4 different test conditions were conducted to determine the repeatability at each set, the effect of the preparation temperature versus the ambient temperature and the mean detachment speed for a minimum of 25 tests.

Glaze ice was grown in the coffee bean mould (refer figure 2.3) on stainless steel 304 substrates, with the contact area between ice and substrate for these tests constant at 2.92 x 10^{-4}m^2. Assuming the mass of ice was the sample mean 1.31 g $\pm$ 0.03 and with the radius of the rotor from the mid-

point to the centre of mass of the ice 167.5 mm, we can calculate the shear stress for the four different test conditions.

Table 2.1 shows the results from preliminary tests on SS 304 substrates for different preparation and ambient temperatures. All successful detachments relate to the situation where the ice sample completely shears off the sample. All remaining tests imply that the ice remained attached to the substrate at the maximum detachment speed. Thus, the experimental setup functions smoothly with an easily detectable detachment of ice. A decrease in the ambient temperature by 5 degrees from -5°C to -10°C causes an increase in the adhesion strength of ice frozen at a single temperature. However tests at -10°C are too close to the maximum capability of the rig for valid results to be collected. The maximum speed of the motor (4500 rpm) is prohibitive in accurately quantifying the exact effect of the preparation and ambient temperatures for the 4 comparisons. The detachment percentages for conditions of -10°C preparation temperature and -10°C ambient temperature; and -5°C preparation temperature and -10°C ambient temperature are relatively low in this regard. The effect of the ambient temperature seems to be more than the preparation temperature. This is plausible, since the method of freezing ice is a static condition, where only the rate differs. Both temperatures are in a range where glaze growth occurs.

Table 2.1: Preliminary results of centrifuge tests on SS 304 substrates.

Temperature Conditions	**Number of Tests**	**Successful Detachments**	**Mean Detachment Speed (rpm)**	**Shear Stress (MPa)**
T_p = -5°C, T_a = -5°C	27	24 (88.9%)	3876 ± 544 (14%)	0.12 ± 0.03
T_p = -5°C, T_a = -10°C	31	12 (38.7%)	3945 ± 566 (14.3%)	0.13 ± 0.04
T_p = -10°C, T_a = -5°C	31	27 (87%)	4254 ± 245 (5.8%)	0.15 ± 0.02
T_p = -10°C, T_a = -10°C	34	3 (8.9%)	4205 ± 232.5 (5.5%)	0.145 ± 0.02

2.5 Repeatability Tests - Cuboid Mould

From the initial set of tests, it is apparent that we cannot make a definite conclusion on the repeatability of the experiment. This is because multiple times during the ice adhesion tests of stainless steel 304 substrates at -5°C and -10°C, the ice did not shear off even at the maximum rotation speed of 4500 rpm. Since the latter is a limiting condition of the motor, we have the following two options to ensure that the ice shears off within this range: increase the radius of the arm; or increase the weight of the ice. Since the centrifuge drum is already enclosed, the easiest option will be to increase the weight of the ice to reduce the speed of detachment. Along with the repeatability, this will help us measure the effect of temperature change on adhesion strength with respect to changes in contact angle parameters for different surfaces.

2.5.1 Mould Design

With respect to the available surface area on the substrate and choosing an aerodynamically sensible shape, a cuboid mould was selected for these tests. The dimensions of the mould chosen were 25 x 15 x 10 mm. The material chosen for the mould was BLUESIL^{TM} RTV 3325, a silicon elastomer which

when a catalyst BLUESIL^{TM} CATA 6H is added to it, cures at 23°C, 50% relative humidity for 6 hours. A general purpose release agent Ease Release© 200 was sprayed on the mould prior to addition of the silicone elastomer. The complete description of the procedure undertaken to prepare the silicone mould is given below:

1. Cut 250 x 250 x 25 mm TRESPA© board.

2. Prepare 20 acrylic cuboids with dimensions 25 (length) x 15 (width) x 10 mm (height). Top edges of all acrylic cuboids must be rounded with 1 mm radius for aerodynamic considerations.

3. Attach 20 cuboids onto the TRESPA© using hot glue.

4. Stick clear acrylic panels around edges of the board and seal with silicone polymer.

5. After the curing period, the mould is removed and washed.

2.5.2 Substrate Description

Three different substrates were used during these tests: stainless steel (SS) 304, aluminium (Al) 6082 with temper T651 and aluminium (Al) 1050A with temper H14. The dimensions of these three different substrates is the same as figure 2.2. Ten substrates were used for each material type during these tests. The mean weight of the aluminium 1050A-H14 substrates is 7.37 g ±

0.04 (0.57%), the aluminium 6082-T651 substrates is 7.29 g ± 0.07 (0.91%) and the stainless steel 304 substrates is 21.04 g ± 0.09 (0.4%) respectively. All three different types of substrates are fairly uniform in their weight characteristics.

2.5.3 Ice Characteristics

To calculate the shear stress at point of detachment, the weight of ice removed is essential. As mentioned earlier, it is impossible to measure the weight of each sample as it detaches inside the environmental chamber; thus an average weight of the representative samples of ice will be determined at both conditions of freezing: -5°C and -10°C. For this purpose, ice was grown on the 10 aluminium 6082-T651 substrates by freezing 18 MΩ Millipore UV-filtered water for 24 hours inside the environmental chamber. A weighing machine was then used inside the chamber to measure the total weight of the ice and substrate. At -5°C preparation temperature, the average ice weight was 3.47 g ± 0.05 (1.37%). When the same procedure was repeated for -10°C preparation temperature, the average ice weight was 3.43 g ± 0.06 (1.69%). Since both values are within the relative error ranges, it is important to note that any change in preparation temperature has negligible effect on the weight of ice formed. The only possible difference will occur in the strength

of the adhesion bond. This will be determined by the subsequent tests. The final weight of the ice at detachment is taken as an overall average of the twenty ice weights at both preparation temperatures with a value of 3.45 g ± 0.06 (1.62%).

2.5.4 Surface Roughness Characterisation

Since the adhesion of ice can be broadly defined in two categories: mechanical and electrostatic [61]; it is important to measure important surface characteristics such as surface roughness and contact angle parameters for the purpose of a coherent analysis. Mechanical adhesion occurs due to relative anchoring of the ice to the substrate based on the surface roughness [61]. The mechanical adhesion strength increases as the surface roughness increases upto a point where the excessive presence of air bubbles between the ice and substrate begins to reduce adhesion [32].

The surface roughness of three different substrates was measured using a Taylor and Hobson FormTalysurf50 profilometer at 20.2°C and relative humidity 57.7% controlled laboratory conditions. The least squares (LS) line method was employed along with a critical wavelength λ_c of 0.8 mm, cut off wavelength λ_s of 0.0025 mm and a bandwidth of 300:1 (ISO). For each

substrate, a single 15 mm assessment length along the cross-sectional width (7.5 mm either side of the centre point) was chosen. Six different surface roughness parameters were measured including R_a - arithmetic average of absolute values, R_q - root mean squared values of absolute values, R_v - maximum valley depth, R_p - maximum peak height, R_t - maximum peak to valley height in assessment length and R_z - maximum peak to valley height (R_v + R_p). These six parameters were chosen because they are the most commonly used in surface characterisation and cumulatively will give us a more definite picture of the substrate surface. Table 2.2 provides surface roughness parameters of all three substrates.

2.5.5 Contact Angle Measurements

For electrostatic adhesion, the key mechanism depends on inter-molecular bonds (especially Van der Waals bonds) and surface tension at the substrate surface [61]. The latter can be quantified from contact angle measurements. For this purpose, we use a sessile drop technique [62] on a NAVITAR 1x adapter 1-6015 goniometer. Images were processed using FTA200 software. All 30 samples were placed in a sealed plastic box to avoid air contamination and in an individual arrangement type to avoid contact with the remaining samples. The samples were cleaned with ordinary laboratory tissue and al-

Table 2.2: Surface roughness parameters of all three substrates.

Substrate Type	R_a (μm)	R_q (μm)	R_v (μm)	R_p (μm)	R_t (μm)	R_z (μm)
SS 304	4.12 ± 0.32 (7.73%)	5.14 ± 0.36 (6.96%)	12.38 ± 0.57 (4.60%)	8.03 ± 0.84 (10.46%)	31.07 ± 1.99 (6.40%)	20.40 ± 1.30 (6.38%)
Al 6082-T651	0.19 ± 0.05 (24.02%)	0.25 ± 0.06 (23.20%)	0.82 ± 0.18 (21.31%)	0.61 ± 0.16 (26.62%)	3.95 ± 1.37 (34.76%)	1.43 ± 0.33 (23.18%)
Al 1050A-H14	0.16 ± 0.06 (39.61%)	0.31 ± 0.16 (53.72%)	1.03 ± 0.28 (27.30%)	0.75 ± 0.26 (34.23%)	6.65 ± 3.35 (50.35%)	1.78 ± 0.51 (28.55%)

ways handled while wearing latex gloves. Drop volume was kept constant at 10 μL for static contact angle. Advancing angle was measured as the average of three consecutive values when drop volume was increased at 2 μL/s. Receding contact angle was measured as the average of three consecutive values when drop volume was decreased and base diameter decreased at 2 μL/s. Room temperature was kept at 25 $\pm$ 0.3°C with humidity 26%. For each substrate of each material, three values of static contact angle were obtained in addition to advancing and receding contact angle. Contact angle hysteresis was calculated as the difference of advancing and receding contact angle. Table 2.3 exhibits the contact angle parameter values of the three different substrate types.

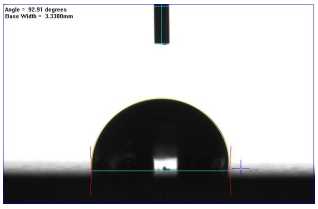
Figure 2.4 shows example calculations of contact angle parameters for SS 304 substrates. Figure 2.5 shows example calculations of contact angle parameters for Al 6082-T651 substrates. Figure 2.6 shows example calculations of contact angle parameters for Al 1050A-H14 substrates.

2.5.6 Results and Analysis

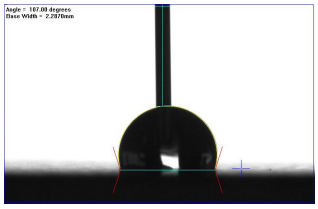
Table 2.4 exhibits detachment speeds and adhesion strength at different preparation and ambient temperatures for three different substrates. For cal-

Table 2.3: Contact angle parameters of three different substrate types.

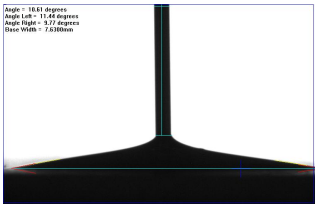
Substrate Type	Static Contact Angle (°)	Advancing Contact Angle (°)	Receding Contact Angle (°)	Contact Angle Hysteresis (°)
SS 304	87.51 ± 4.51 (5.15%)	104.61 ± 2.48 (2.37%)	9.32 ± 1.04 (11.16%)	95.29 ± 10.87 (11.41%)
Al 1050A-H14	95.59 ± 2.86 (2.99%)	103.75 ± 1.56 (1.51%)	20.76 ± 2.66 (12.81%)	82.99 ± 10.70 (12.90%)
Al 6082-T651	95.03 ± 2.88 (3.03%)	102.43 ± 2.76 (2.7%)	19.75 ± 2.83 (14.33%)	82.68 ± 12.06 (14.58%)



(a) Static (92.92°)

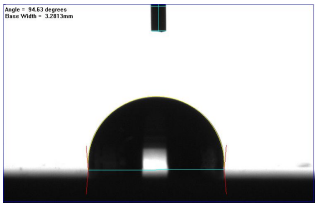


(b) Advancing (107.08°)

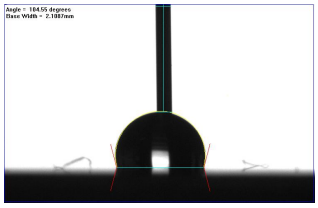


(c) Receding (10.61°)

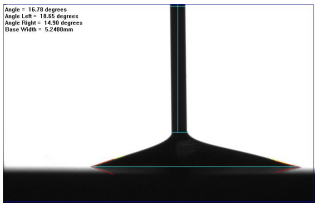
Figure 2.4: Contact angle measurements of SS 304.



(a) Static (94.63°)

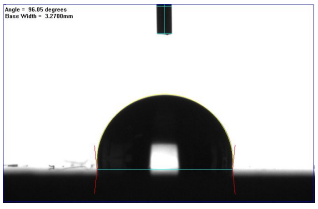


(b) Advancing (104.55°)

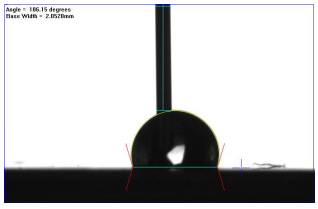


(c) Receding (16.78°)

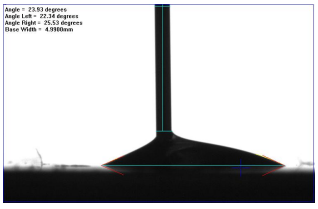
Figure 2.5: Contact angle measurements of Al 6082-T651.



(a) Static (96.05°)



(b) Advancing (106.15°)



(c) Receding (23.93°)

Figure 2.6: Contact angle measurements of Al 1050A-H14.

culation of adhesion strength, the mass of the ice m is $3.45 \pm 0.06\,\mathrm{g}$ (1.62%), r is 175 mm and A is $375\,\mathrm{mm}^2$.

Figure 2.7 plots the adhesion strength of the three different substrates at different values of preparation and ambient temperature. It is apparent from the figure that there is a definite influence of the preparation and ambient temperature on the adhesion strength. Guerin et al. (2016) [61] define the adhesion of ice on a substrate as mainly a combination of mechanical and electrostatic components. From Figure 2.7, it is apparent that there is an influence of the preparation and ambient temperature on the adhesion strength. The mean value of ice adhesion strength shows a clearly increasing trend with reduced preparation temperatures. However, there is insufficient available data with high uncertainty to quantify that trend. At the ice-substrate interface, there exists an amorphous liquid-like layer which has thickness in the nanometre range [63]. It is this layer, that is the key to understanding the adhesion of ice, as it is the part of the ice in total contact with the substrate when it shears. Both aluminium and stainless steel are rigid enough to assume surface properties remain constant and hence mechanical adhesion does not change upto -13°C [64].

When water is frozen at -10°C as compared to -5°C on the metallic substrate, the Van der Waals forces that mainly comprise electrostatic adhe-

Table 2.4: Detachment speeds and adhesion strength at different preparation and ambient temperatures for three different substrates.

Substrate Type	T_p -5°C, T_a -5°C	T_p -10°C, T_a -5°C	T_p -5°C, T_a -10°C	T_p -10°C, T_a -10°C
SS 304 Detachment Speed (rpm)	3119.5 ± 152.11 (4.88%)	3448.5 ± 197.63 (5.73%)	4062 ± 225.3 (5.55%)	4413 ± 184.64 (4.18%)
SS 304 Adhesion Strength (kPa)	171.73 ± 16.98 (9.89%)	209.93 ± 24.3 (11.57%)	291.27 ± 32.64 (11.21%)	343.79 ± 29.28 (8.52%)
Al 6082-T651 Detachment Speed (rpm)	2746.5 ± 130.31 (4.75%)	3031.5 ± 176.44 (5.82%)	3768 ± 280.2 (7.44%)	4027.5 ± 190.37 (4.73%)
Al 6082-T651 Adhesion Strength (kPa)	133.16 ± 12.82 (9.63%)	162.23 ± 19.07 (11.75%)	250.63 ± 37.49 (14.96%)	286.35 ± 27.45 (9.59%)
Al 1050A-H14 Detachment Speed (rpm)	2862 ± 143.65 (5.02%)	3186 ± 214.48 (6.73%)	3724 ± 232.52 (6.24%)	4208.5 ± 290.73 (6.91%)
Al 1050A-H14 Adhesion Strength (kPa)	144.6 ± 14.71 (10.17%)	179.18 ± 24.29 (13.56%)	244.82 ± 30.81 (12.58%)	312.66 ± 43.51 (13.91%)

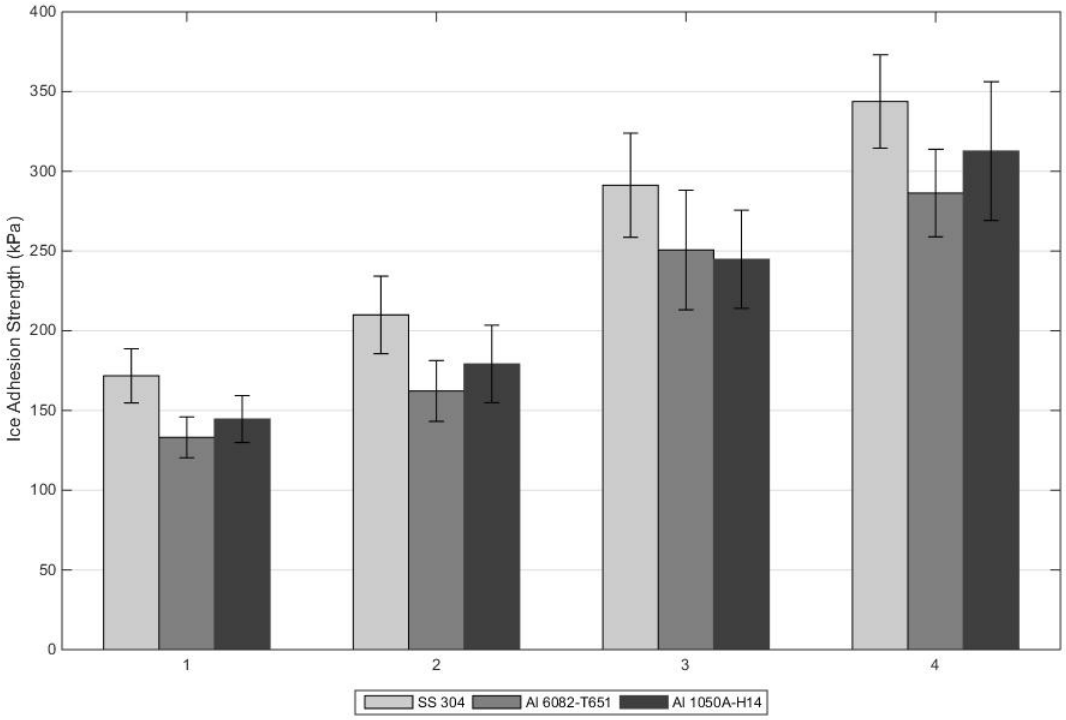


Figure 2.7: The adhesion strength of the three different substrate types at different preparation and ambient temperatures. T_p = -5°C, T_a = -5°C (1); T_p = -10°C, T_a = -5°C (2); T_p = -5°C, T_a = -10°C (3); T_p = -10°C, T_a = -10°C (4).

sion component are stronger, since the molecules of ice in contact with the substrate are at a lower temperature and hence a lower excitation state. In theory, to remove the ice in such a situation will take a larger amount of force since the Van der Waals forces in addition to mechanical adhesion need to be overcome for shearing to occur. The thermal conductivity of stainless steel and aluminium is 8 and 100 times greater than ice respectively. When the temperature in the environmental chamber is set to -5°C after forming ice at -10°C, the substrate attains the ambient temperature much faster than the ice. Heat is now conducted from the substrate to the ice and the temperature at the ice-substrate interface obtains the temperature of the substrate which acts as a heat sink. This is why even when the preparation temperature is changed from -5°C to -10°C, the difference in adhesion strength is within the error limits for all three substrates and cannot be quantified. It is worth noting here that the samples were frozen while attached to different rotors. However, the test was conducted using only one rotor to minimise error.

However when the ambient temperature is changed from -5°C to -10°C when the preparation temperature is kept constant at -5°C, the adhesion strength increase is quantifiable. The reasons for this are that since conduction through the substrate is much faster than ice, the substrate rapidly reaches the new temperature of -10°C. The ice-substrate interface also reaches

this temperature as heat is conducted from the ice to the substrate with the latter acting as a heat sink. It is for the above reason, that the amorphous liquid-like layer is influenced more by the ambient than the preparation temperature and this change is quantified in Table 1.4. When the preparation temperature is changed from -5°C to -10°C and the ambient temperature is kept constant at -10°C, no quantifiable change is noticed, further reinforcing our findings. According to Makkonen (2012) [64], adhesion strength increases with a decrease in freezing temperature because the liquid-like layer reduces in height with temperature decrease. Our findings further validate his theory.

This conclusion is of course valid for conducting surfaces such as power cables and ship decks, where ice is formed from the freezing of left over water as is replicated in our freezing process. These findings are in contrast to Meuler et al. (2010) [65], who measured the adhesion strength of ice using a force transducer on a peltier plate. Glaze ice columns were grown on test substrates and tests were conducted at -5°C, -10°C and -15°C. Adhesion strength plotted versus receding contact angle ($1 + \cos\theta_{rec}$) at 0.5 $\mathrm{mm\,s^{-1}}$ incident probe speed yielded linear best fits of 378 kPa ± 125, 307 kPa ± 101 and 311 kPa ± 84 respectively. All three values are within error limits, whereas the influence of changing temperature conditions has a qualitative and quantitative impact on adhesion strength in our case.

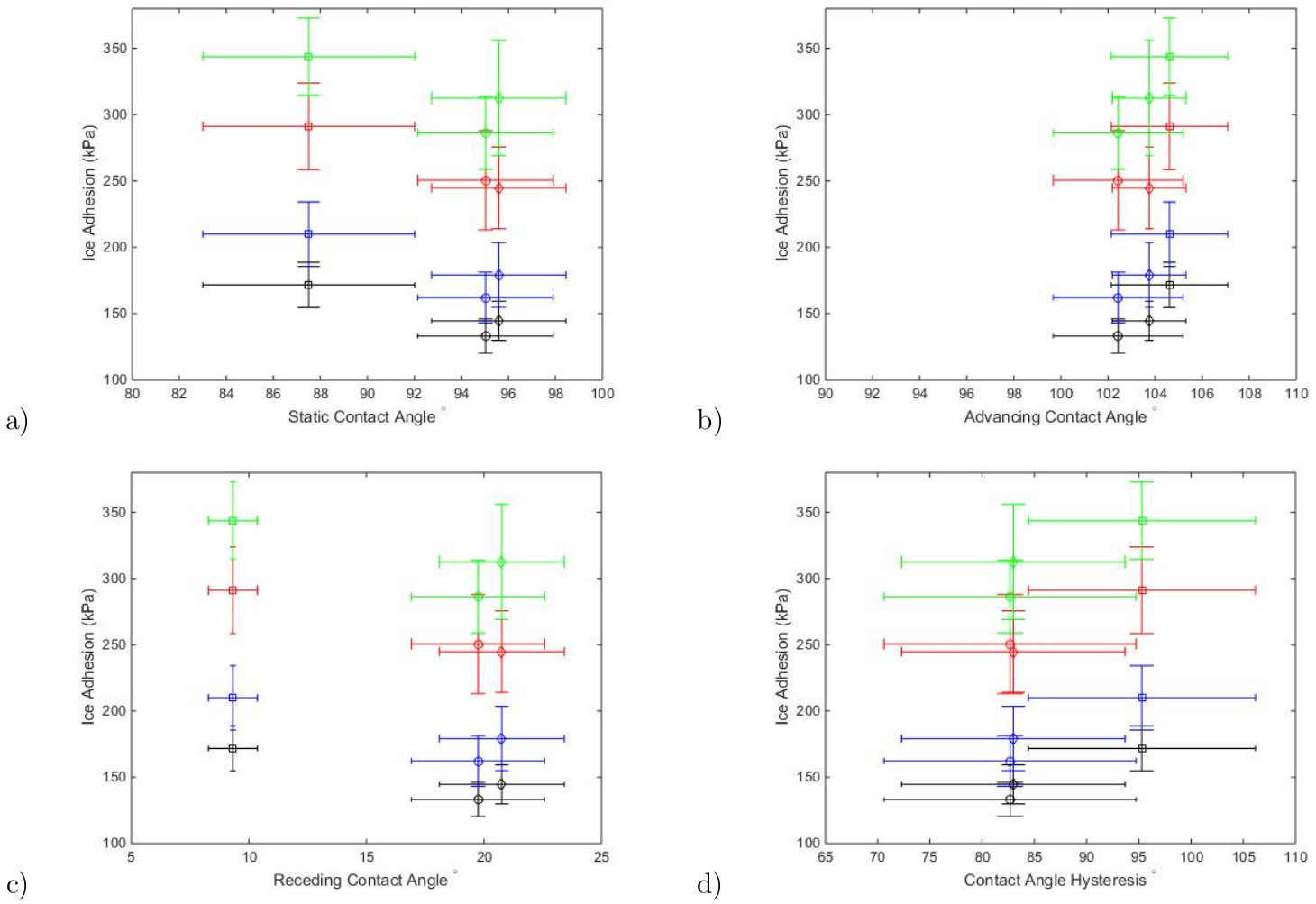


Figure 2.8: Adhesion strength for SS 304, Al 1050A-H14 and Al 6082-T651 versus a) Static contact angle, b) Advancing contact angle, c) Receding contact angle and d) Contact angle hysteresis.

Figure 2.8 exhibits static, advancing, receding and CAH versus adhesion strength at different preparation and ambient temperature conditions respectively for ready comparison with previous work in Section 2.4 and the literature [30, 61, 65]. The markers for the substrates are: stainless steel 304 ($\square$), aluminium 6082-T651 ($\circ$) and aluminium 1050A-H14 ($\diamond$). The colour coding for the different preparation and ambient conditions are as follows: T_p = -5°C, T_a = -5°C (black); T_p = -10°C, T_a = -5°C (blue); T_p = -5°C, T_a = -10°C (red); T_p = -10°C, T_a = -10°C (green). Although our surface roughness data has significant error, SS 304 has Ra value one order higher than both of the aluminium substrates. This is a contributing factor towards increasing mechanical adhesion and therefore overall adhesion strength.

Although Laforte and Beisswenger (2005) [7] mention that freezer ice can lead to 300% relative error, our work shows that using an environmental chamber and highly pure, de-ionised water can produce highly repeatable samples (Table 2.6). The acceleration rate used is 10% of the rate used in the former which also contributes to more repeatable results. The shear stress values are within error limits as the substrate material and icing conditions are similar.

Table 2.5: Percentage influence of preparation and ambient temperatures on adhesion strength for three different substrate types from base conditions of T_p = -5°C, T_a = -5°C [6]. * refers to a value that lies within the error limits of adhesion strength.

Substrate Type	T_p=-10°C, T_a=-5°C (%)	T_p=-5°C, T_a=-10°C (%)	T_p=-10°C, T_a=-10°C (%)
SS 304	22.24*	69.61	100.19
Al 6082-T651	21.83*	88.22	115.04
Al 1050A-H14	23.91*	69.31	116.22

Table 2.6: Comparison of results with Laforte and Beisswenger (2005) [7].

Test Conditions	**Present Work**	**Laforte and Beisswenger (2005)**
Preparation Temperature	-10°C	-8°C
Ambient Temperature	-10°C	-10°C
Acceleration Rate	30 rpm/s	300 rpm/s
Ice Type	Freezer	Spray (Freezing Drizzle)
Rotor Length	385 mm	340 mm
Shear Stress	0.29 Mpa ± 0.03 (9.6%)	0.35 MPa ± 0.06 (18%)
Substrate Material	Aluminium 6082–T651	Aluminium 6061–T6
Water Source for Ice	18 MΩ	Unknown

2.6 Conclusion

An experimental setup has been designed and tested for repeatability to determine the adhesion strength of ice. The first section in this chapter focussed on determining the adhesion strength of stainless steel using a coffee bean mould. The method was not entirely successful in determining adhesion strength and repeatability accurately because in different conditions of preparation and ambient temperature, the ice did not shear off before the maximum rotational speed of 4500 rpm was attained. Ice adhesion tests have been performed on three different materials at four conditions of preparation and ambient temperature using a spinning centrifuge. The increase in weight of the ice by a factor of 2.6 has enabled us to accurately measure mean adhesion speeds and strength with relative errors ranging from 9.69–14.96%. Results indicate that increasing surface roughness and CAH respectively; increases adhesion strength. This finding reinforces established facts from the literature [7, 31, 32, 61].

Reducing the preparation temperature of ice formation does not affect the weight of the sample and qualitatively increases adhesion strength. The centrifuge experiment is not sensitive enough to quantify this change. Reducing the ambient temperature causes a significant increase in adhesion

strength (Table 2.5). The reasons for this are, that at lower ambient temperature, the metallic substrate attains the surrounding temperature much faster than the ice. The substrate acts as a heat sink where heat flows from the body at higher temperature (ice) to the body at the lower temperature (substrate); thereby strengthening the bond at the amorphous liquid-like layer [63]. The results are limited to thermally conducting substrates and short timescales for the experiment to equilibrate to ambient temperature. It will be interesting to see how the data is affected if the ice is exposed to a stable temperature for a longer period of time. This research will aid us to determine adhesion strength of ice formed on conducting structures after studying weather patterns and climate conditions.

Chapter 3

Centrifuge Adhesion Tests of Icephobic Coatings

3.1 Introduction

Both fixed-wing and rotor-wing aircraft are often fitted with both anti-icing (i.e. preventing ice formation) and de-icing (i.e. removing accreted ice) devices to mitigate the problem, but these devices have disadvantages. Heating electro-thermal mats for de-icing, for example, consumes a large amount of power ($\sim 10^5$ W), even when restricted to a small portion of the wing close to the leading edges, leaving a large portion of the wing vulnerable to ice

build-up [20]. The concept of smart icephobic coatings covering a larger area of wing are available [30], but there are currently significant technological barriers to implementing these commercially. The practicality of applying coatings to extensive surfaces and their durability in the harsh conditions aircraft is limited. A motivation for the modelling described in this chapter, is to develop an understanding of the basic physical processes leading to ice accretion to inform strategies for improving anti-icing techniques.

Ice accretion is problematic in several engineering applications such as power cables, radio masts or wind turbines [34]. Research into finding icephobic coatings has been active since the 1960's [35], but several issues persist: in particular, the durability of coatings and the practicalities of applying to extensive areas on structural surfaces exposed to rugged environments. Several materials have been proposed as icephobic coatings including polytetrafluoroethylene (PTFE) [44, 37]; fluorinated polymethylsiloxane and octavinyl-polyhedral oligomeric silsesquioxanes (OVPOSS) [38, 36, 39]; Al_2O_3 nanoparticle in silicone rubber solution [40], combination of hydrogen peroxide and an acid (nitric or hydrochloric) [66], silica nanoparticles and polymethyl methacrylate (PMMA) [67] and sol-gel coatings containing tetraethylorthosilicate (TEOS) and 3-glycidylpropyl trimethoxy silane (GPTMS) [27].

By investigating this range of coatings, we aim to add further evidence to the debate over the correlation between icephobicity and hydrophobicity [41, 42, 43]. In particular, we look at the contact angle hysteresis for a surface [44, 37, 38, 36]; to evaluate its link to icephobicity.

The aim of this work was thus to evaluate the performance of two types of coating, one set using silica-based nano-particles with the other set employing carbon nano-tubes, with the potential to become icephobic smart coatings to reduce runback ice accretion on aircraft wings. Each coating was characterised for contact angle (CA) (static, advancing, receding and CA hysteresis), surface roughness and the adhesion strength of an ice sample grown in controlled conditions. These tests were repeated, reusing each coating sample by growing new ice on it after detachment of the previous ice sample, to evaluate the deterioration in performance of the coating with use.

3.2 Coating Design

In the present work we investigate two approaches to coating design. First, the approach of Zhang et al. (2015) [68] who prepared superhydrophobic coatings using silica nanoparticles immersed in chloroform and spin coated onto glass slides, has been adopted and developed. Results showed reduced

wetting of water droplets on coated surfaces.

In an alternative approach to designing the coating, it was noted that the presence of reinforced materials such as nanoparticles, nanowires and nanotubes in a matrix (typically polymer) increases the surface roughness of the nanocomposites, thus resulting in higher contact angles with water droplets. For example, silica reinforced acrylic polymer composites can exhibit superhydrophobic surfaces and anti-icing capability upon the impact of supercooled water [69]. The surface morphology of the coating also strongly influences the anti-icing capability. Nanocomposites with different surface roughness have been prepared by varying the amount of ZrO_2/fluoropolymer nanopowder suspension and mixing with perfluoroalkyl methacrylic copolymer have also been fabricated using spraying or spin-coating, followed by heat treatment to remove residual solvents [70]. A second batch of coatings uses surface texturing and chemical modification of the aluminium substrate before deposition of carbon nanotube composite coatings to prevent ice adhesion.

Fourteen coatings have been developed with potential anti-icing capability and tested in this work. These coatings were applied to an Aluminium 6082, with T651 temper, polished substrate plate with thickness 1 mm and total surface area 1000 mm^2, on which ice could be grown and the

sample plate fixed to the rotor of the centrifuge to measure adhesion strength. Of a total of 34 substrate plates, 20 were left uncoated for repeatability tests. The remaining 14 plates were coated with the fourteen coatings to be tested which are divided into two groups: Group 1 – A, B, C and D and Group 2 – E, F, G, H, I, J, K, L, M and N.

Group 1: All the four samples (A, B, C and D) were fabricated using silica nanoparticles and polystyrene by a spin coating method. Silica nanoparticles and polystyrene were mixed together at weight ratio of 23.8:1 and dissolved into chloroform followed by stirring for about 1 hour at room temperature. The four thin film samples of A, B, C and D were deposited using silica nanoparticles/polystyrene solution by spin coating at 1500 rad/min for 1 minute onto Al alloy substrates. A heat treatment at 550°C for 2 hours for samples C and D was performed. Then a surface modification with 1H,1H,2H,2H-perfluorooctyltriethoxysilane (PFTS) was performed using the chemical vapour deposition method for all four samples.

Group 2: Samples E, F, G, H, I, J, K, L, M and N were prepared using carbon nanotube technology. The bare substrates were mechanically polished using a grinding machine with 1200 sand paper and subject to ultrasonic cleaning with acetone, ethanol and water for 10 minutes. The deposition method used was an eco-friendly, non-vacuum and cost-effective

aerosol assisted deposition coating rig specifically set up for manufacturing of nanostructured carbon-based coatings for anti-icing applications (see Figure 3.1). The starting solution was prepared using an appropriate solvent as disperser of carbon nanotubes. The surfaces of multi-walled CNT ($\sim$ diameter 9 nm, length 0.5-3μm) were functionalized with fluorosilane leading to the hydrophobic behaviour. Prior to deposition, the final dispersion was placed in an ultrasonication bath for a few minutes to ensure good dispersion of carbon nanotubes. This was verified at UCL London using a scanning electron microscope. The content of carbon nanotubes was varied in order to study their effect on surface roughness, anti-icing properties and electrical conductivity. Furthermore, in order to promote the adhesion between the coating and the aluminium substrate an interlayer with a thickness of 15-25μm of organic-based compound containing acetate was used prior to anti-icing coating deposition. Finally, for selected samples, a final hydrophobic polymeric surface promoter layer was applied.

Tables 3.1 and 3.2 provide coating labels (used throughout the text) and their respective chemical composition, contact angle (Static - SCA, Advancing - ACA, Receding - RCA and Hysteresis - CAH) and surface roughness properties prior to testing. All values are the average of three measurements. It is worth noting here that SCA is dependent on the method of drop injec-

tion and characteristics such as syringe diameter or distance that the drop falls on the surface will affect the final value [62]. In the case of aerofoils, we have supercooled droplets of a much smaller diameter ($\sim$ 10–80μm) impacting the surface at much higher speeds ($\sim$ 100–200 m s^{-1}). Hence this links back to the main objectives of this research regarding the development of icephobic coatings that prevent the spread and penetration of water on the coated surface. According to Yuan and Lee (2013) [71], CAH arises from chemical heterogeneous surfaces and/or surface roughness. The former as in the case of an example of a hydrophobic surface, causes smaller CAH values due to the pinning down (ACA) and decreased contraction (RCA) of the water droplet; while microscopic differences on the latter's slopes can alter the pinning motion of the drop, thus affecting CAH.

3.3 Experimental setup and procedure

See Section 2.3 for detailed experimental setup and procedure. Preparation and ambient temperature were kept constant at -5°C for all tests. Surface roughness of the 20 uncoated substrates was measured using a Mitutoyo Surftest SV-622 profilometer. Surface roughness of the 14 coated substrates was measured using Alicona Infinite Focus Optical Microscope, with focus

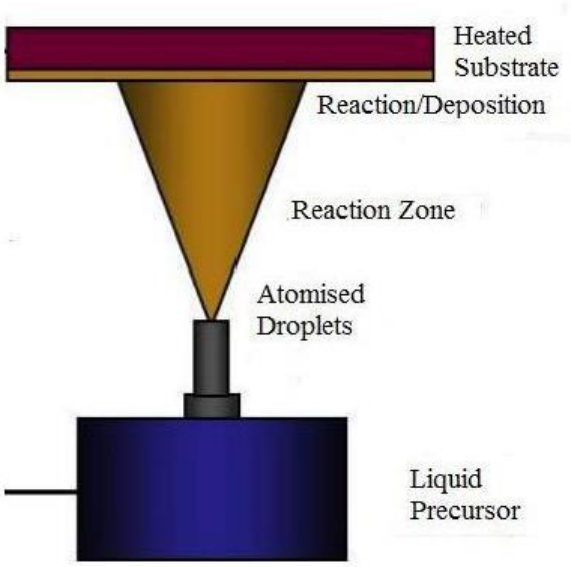


Figure 3.1: A schematic diagram of the Aerosol Assisted Deposition process [4].

Table 3.1: Coating label and its respective composition, contact angle and surface roughness properties (A-G). A single uncoated sample characteristics are also shown.

Coating	**Description**	**SCA (°)**	**ACA (°)**	**RCA (°)**	**CAH (°)**	R_a **(μm)**
Uncoated	Bare, Al 6082-T651 substrate	95.8 ± 3.14	102.2 ± 4.53	33.1 ± 3.32	69.1 ± 5.62	0.295 ± 0.072
A	Silica nanoparticles and polystyrene (no heat treatment) with PFTS treatment	102 ± 2	110.7 ± 1	83 ± 4.9	27.7 ± 3.8	1.1 ± 0.1
B	Silica nanoparticles and polystyrene (no heat treatment) with PFTS treatment	100.4 ± 3.2	108.9 ± 0.7	82.7 ± 5.6	26.2 ± 5	1.1 ± 0.1
C	Silica nanoparticles and polystyrene (2 hours heat treatment at 550°C) with PFTS treatment	130.5 ± 3.8	132.7 ± 5.7	87.9 ± 4.8	44.8 ± 3.7	2 ± 0.1
D	Silica nanoparticles and polystyrene (2 hours heat treatment at 550°C) with PFTS treatment	135.1 ± 1.7	137.2 ± 3.4	92.4 ± 5.4	44.2 ± 2.2	2.1 ± 0.3
E	5% non-functionalised carbon nanotube content with no interlayer and no deposition of final surface promoter layer	72.3 ± 1.2	N/A	N/A	N/A	0.4 ± 0.0003
F	20% non-functionalised carbon nanotube content with no interlayer and no deposition of final surface promoter layer	85.3 ± 4.7	N/A	N/A	N/A	0.4 ± 0.0005
G	20% functionalised carbon nanotube content with no interlayer and with no deposition of final surface promoter layer	143.5 ± 1.9	N/A	N/A	N/A	0.9 ± 0.0004

Table 3.2: Coating label and its respective composition, contact angle and surface roughness properties (H-N).

Coating	**Description**	**SCA (°)**	**ACA (°)**	**RCA (°)**	**CAH (°)**	**R_a (μm)**
H	20% functionalised carbon nanotube content with use of an interlayer and no deposition of final surface promoter layer	140.7 ± 2.7	143.6 ± 5.4	62.3 ± 4.2	81.3 ± 2.2	1.6 ± 0.2
I	20% functionalised carbon nanotube content with use of an interlayer and with deposition of final surface promoter layer	154.1 ± 1.6	157.8 ± 2.9	145.1 ± 4.4	12.8 ± 7.2	2.7 ± 0.4
J	10% functionalised carbon nanotube content with use of an interlayer and with no deposition of final surface promoter layer	113 ± 3.2	133.9 ± 2.6	57.6 ± 2.9	76.4 ± 4.6	1.4 ± 0.1
K	5% functionalised carbon nanotube content with use of an interlayer and with no deposition of final surface promoter layer	108.2 ± 0.9	129.8 ± 2.9	49.3 ± 1.6	80.5 ± 3.3	1.6 ± 0.3
L	2.5% functionalised carbon nanotube content with use of an interlayer and with no deposition of final surface promoter layer	110.9 ± 0.6	132.7 ± 1.4	34.2 ± 2.3	98.5 ± 2.7	1.6 ± 0.2
M	10% functionalised carbon nanotube content with use of an interlayer and with deposition of final surface promoter layer	108.1 ± 0.7	118.7 ± 0.4	34.1 ± 2.7	84.6 ± 2.7	1.4 ± 0.1
N	5% functionalised carbon nanotube content with use of an interlayer and with deposition of final surface promoter layer	159.7 ± 3	164.7 ± 3.1	138.6 ± 1.2	26.1 ± 3.3	3.2 ± 0.2

area 2 x 2 mm and characteristic wavelength L_c = 250 μm. Glaze ice was chosen in our experiment because in reality, it is much harder to remove from a surface than rime, providing an upper bound measurement for ice adhesion. Further, glaze generally forms on regions of the wing for which these coatings are designed and also because consistent glaze samples can be grown artificially, we can measure adhesion more repeatedly than would be achievable with rime ice samples.

3.4 Results

In this section, results from each coating will be tabulated along with images of contact angle parameters and surface roughness measurements. A figure denoting the degradation of the coating with respect to number of repetitive ice adhesion measurements is also provided.

3.4.1 Uncoated substrates

The adhesion strength of a glaze ice sample, grown as described in the previous chapter, on 20 uncoated Al 6082-T651 substrates was measured under nominally identical ice preparation and adhesion test conditions (-5°C) to

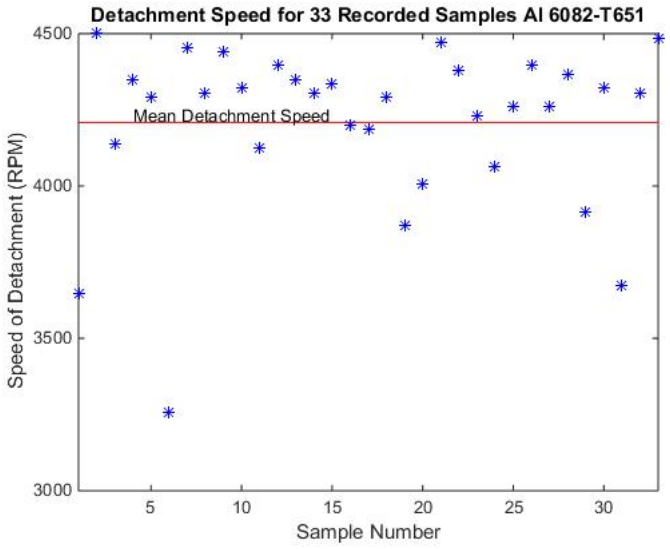


Figure 3.2: Mean adhesion speed of 20 uncoated aluminium 6082-T651 substrates.

evaluate the repeatability of the preparation and test method. Since the uncoated substrates were prepared in a different manner to those in the previous chapter (namely polishing), it was necessary to carry out these tests to ascertain the mean adhesion strength to calculate ARF. Figure 3.2 shows the mean adhesion speed of 20 uncoated aluminium 6082-T651 substrates. The characteristics of the 20 samples and their adhesion strength over 33 tests, are shown in Table 3.3.

Note that the repeatability of this adhesion strength test compares favourably with previous, similar measurements. We believe that this is

Table 3.3: Properties and their variation across 20 uncoated substrates illustrating the repeatability of each measurement.

Property	**Mean and standard deviation for 20 samples**
Static contact angle	93.2 ± 2.6° (SD = 2.8%)
Advancing contact angle	100 ± 5.3° (SD = 5.3%)
Receding contact angle	35.7 ± 4.9° (SD = 13.7%)
Contact angle hysteresis	64.5 ± 5.5° (SD = 8.5%)
Roughness	0.3 ± 0.05 μm (SD = 17%)
Detachment speed	4210 ± 270 rpm (SD = 6.4%)
Adhesion strength	152 ± 20 (SD = 13.2%)

partly due to the method employed for growing ice on the substrates that yields a repeatable layer of glaze ice at contact with only rare imperfections such as cracks or air inclusions. A crucial element of the current work is to consider the durability of the coatings, thus the process surface characterisation (Tables 3.1 and 3.2), ice growth, ice detachment through the adhesion test was repeated 10 times (17 for the non-conductive coatings) for each coated substrate barring E, F and G.

To evaluate the reduction in performance of the coatings with use, the adhesion reduction factor after cycle N, ARF(N), was fitted as an exponential decay

$$\mathrm{ARF}(N) = \mathrm{ARF}(1)(e^{-N\alpha} + C), \tag{3.1}$$

where α is a coating durability rate and C characterizes the retained icephobic fraction of the sample after many cycles i.e. ARF(1).C is the projected adhesion reduction factor of the coating as the number of cycles, N, tends to infinity. This retained icephobicity thus characterizes the long term chemical and/or surface finish alteration to the substrate surface the coating has made.

3.4.2 Coated Substrates

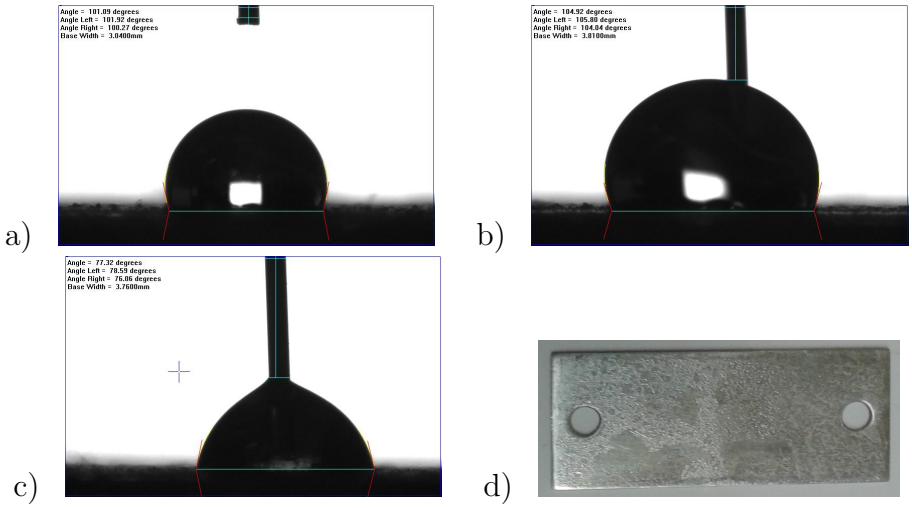


Figure 3.3: Example measurements of 1) Static (101.09°), 2) Advancing (104.92°), 3) Receding contact angle (77.32°) respectively for Coating A. 4) shows the top view of the coating.

Refer to Table A.1 (Appendix A) for the tabulated results from the test period for coating A. Figure 3.3 shows example contact angle measurements and the top view of coating A. Figure 3.4 exhibits the plot of ARF and CAH versus number of cycles for coating A. The LHS axis represents ARF values and the RHS axis represents CAH values respectively. The error bars shown in the figure for ARF are obtained from the value of standard deviation for the adhesion strength calculated in Table 3.3. This value of 13.2% SD in repeatability is due to differences in the surface texture of the 20 uncoated substrates, calculation of time of detachment and temperature

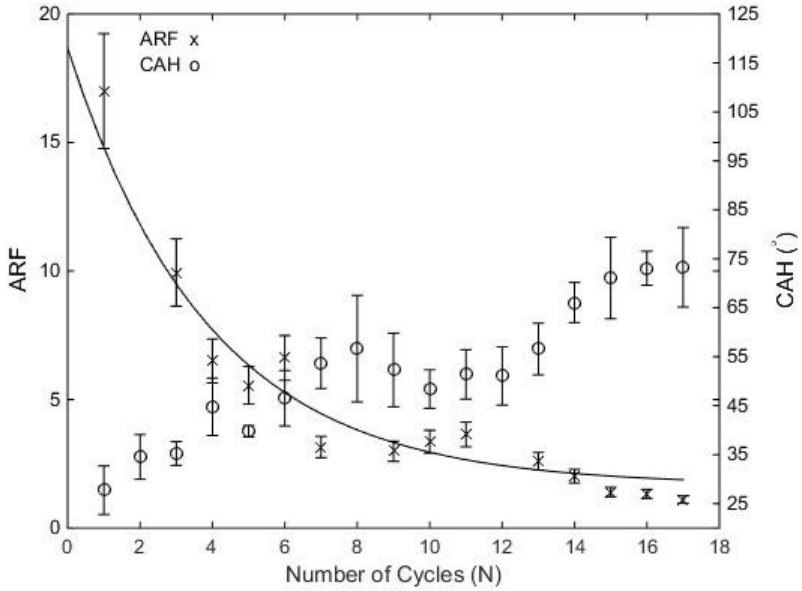


Figure 3.4: ARF and CAH versus number of cycles for coating A.

variations in the environmental chamber etc. The errors of CAH are calculated from an average of three values of advancing and receding contact angle respectively.

Refer to Table A.2 (Appendix A) for the tabulated results from the test period for coating B. Figure 3.5 shows example contact angle measurements and the top view of coating B. Figure 3.6 exhibits the plot of ARF and CAH versus number of cycles for coating B.

Refer to Table A.3 (Appendix A) for the tabulated results from the test period for coating C. Figure 3.7 shows example contact angle measure-

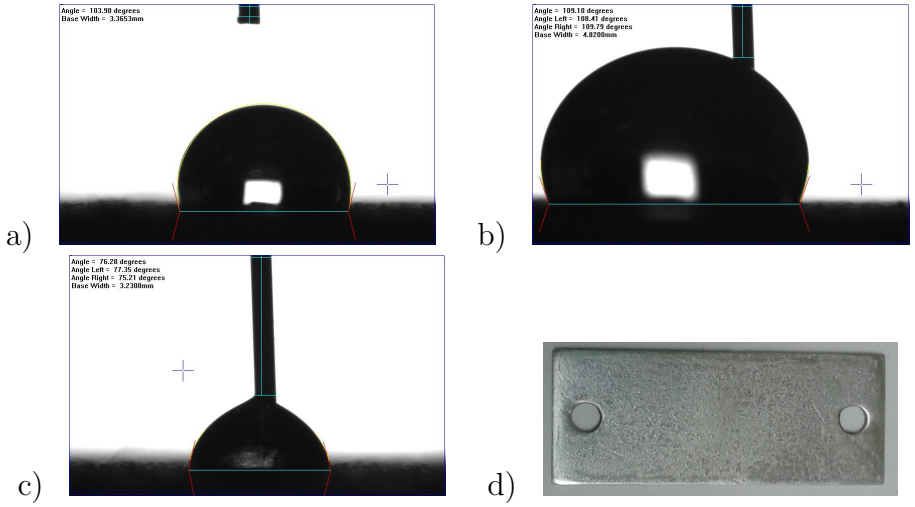


Figure 3.5: Example measurements of 1) Static (103.9°), 2) Advancing (109.1°), 3) Receding contact angle (76.2°) respectively for Coating B. 4) shows the top view of the coating.

ments and the top view of coating C. Figure 3.8 exhibits the plot of ARF and CAH versus number of cycles for coating C.

Refer to Table A.4 (Appendix A) for the tabulated results from the test period for coating D. Figure 3.9 shows example contact angle measurements and the top view of coating D. Figure 3.10 exhibits the plot of ARF and CAH versus number of cycles for coating D.

Refer to Table A.5 (Appendix A) for the tabulated results from the test period for coating E. Figure 3.11 is ice attached to coating E inside the environmental chamber. Figure 3.12 exhibits an example of static contact

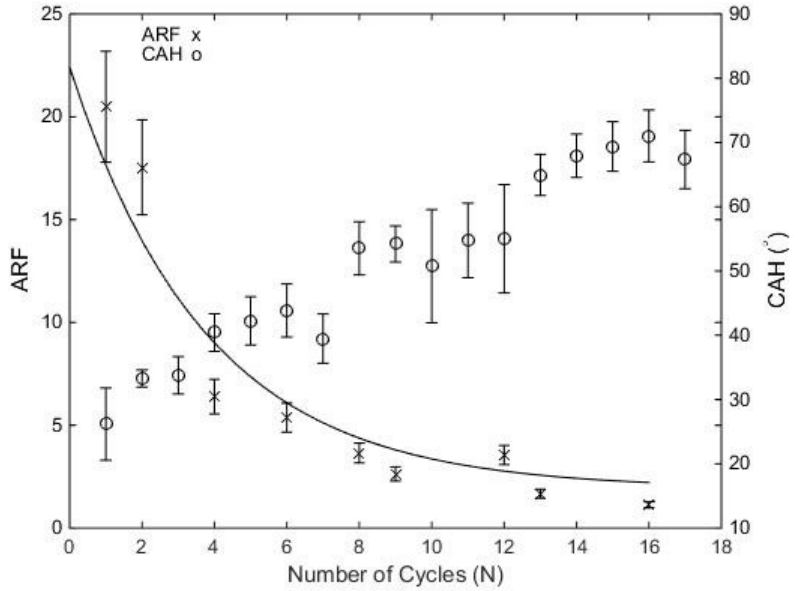


Figure 3.6: ARF and CAH versus number of cycles for coating B.

angle measurements for coating E. Figure 3.13 exhibits the coating E under Alicona optical microscope at 20x magnification.

The surface roughness of coating E was 426 ± 32 nm and static contact angle was 72.3 ± 1.2° before the test period respectively.

Refer to Table A.6 (Appendix A) for the tabulated results from the test period for coating F. Figure 3.14 is ice attached to coating F inside the environmental chamber. Figure 3.15 exhibits an example of static contact angle measurements for coating F. Figure 3.16 exhibits the coating F under Alicona optical microscope at 20x magnification.

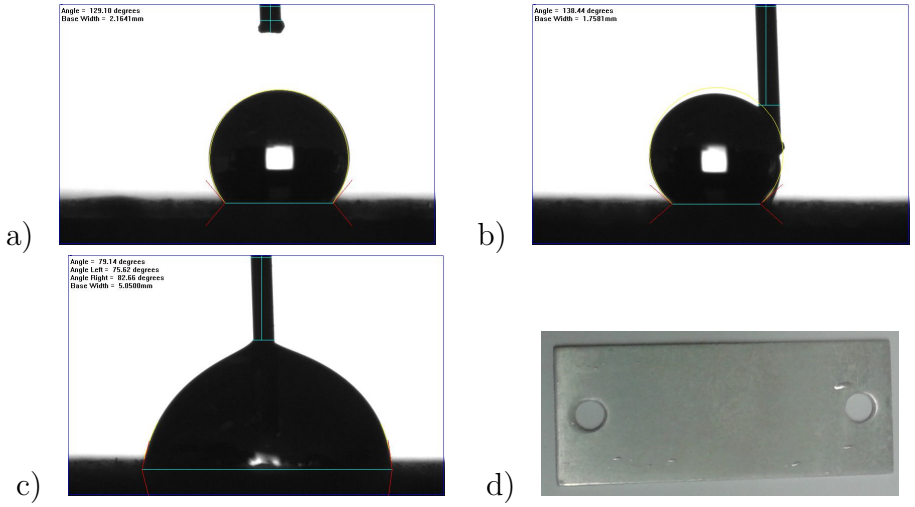


Figure 3.7: Example measurements of 1) Static (129.1°), 2) Advancing (138.44°), 3) Receding contact angle (79.14°) respectively for Coating C. 4) shows the top view of the coating.

The surface roughness of coating F was 398 ± 53 nm and static contact angle was 85.3 ± 4.7° before the test period respectively.

Refer to Table A.7 (Appendix A) for the tabulated results from the test period for coating G. Figure 3.17 is ice attached to coating G inside the environmental chamber. Figure 3.18 exhibits an example of static contact angle measurements for coating G. Figure 3.19 exhibits the coating G under Alicona optical microscope at 20x magnification. Figure 3.20 shows ARF versus number of cycles for coating G.

The surface roughness of coating A was 857 ± 42 nm and static

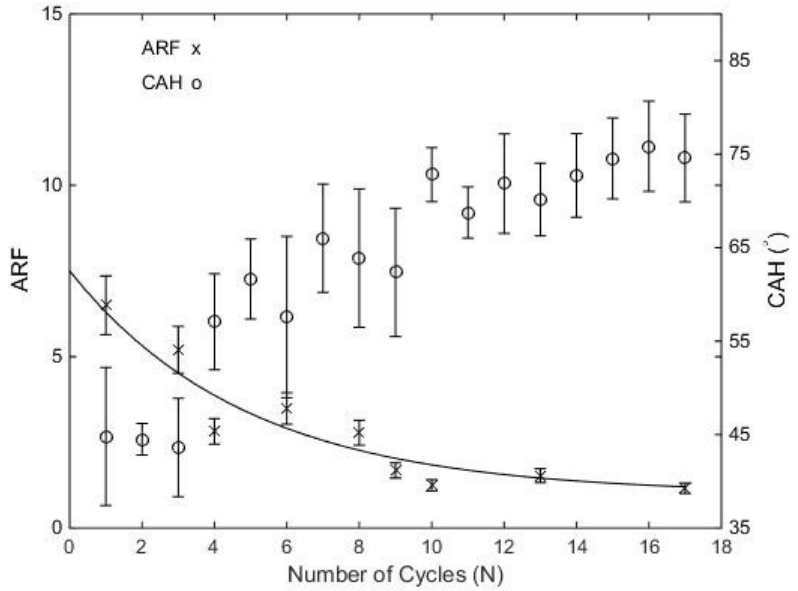


Figure 3.8: ARF and CAH versus number of cycles for coating C.

contact angle was 143.5 ± 1.9° before the test period respectively.

Refer to Table A.8 (Appendix A) for the tabulated results from the test period for coating H. Figure 3.21 shows example contact angle measurements and the top view of coating H. Figure 3.22 shows Coating H under Alicona optical microscope at 20x magnification. Figure 3.23 exhibits the plot of ARF and CAH versus number of cycles for coating H.

Refer to Table A.9 (Appendix A) for the tabulated results from the test period for coating I. Figure 3.24 shows example contact angle measurements and the top view of coating I. Figure 3.25 shows Coating I under

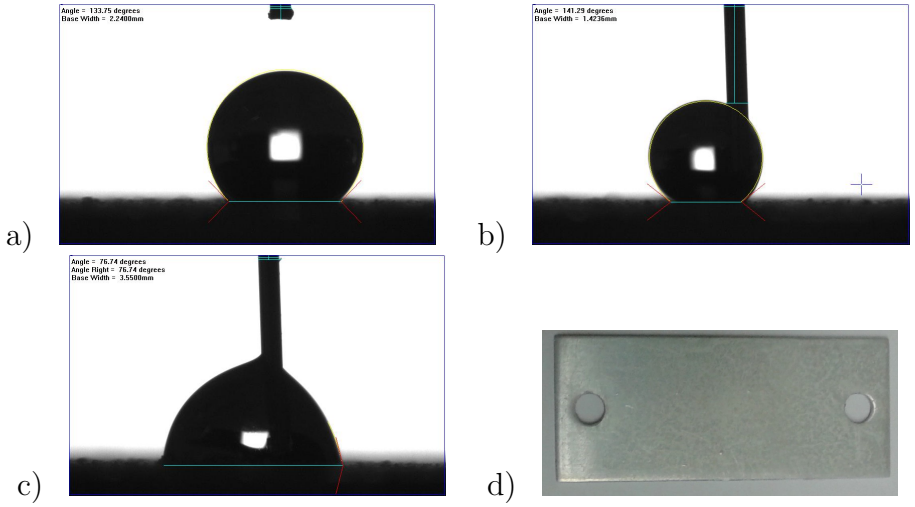


Figure 3.9: Example measurements of 1) Static (133.75°), 2) Advancing (141.29°), 3) Receding contact angle (76.74°) respectively for Coating D. 4) shows the top view of the coating.

Alicona optical microscope at 20x magnification. Figure 3.26 exhibits the plot of ARF and CAH versus number of cycles for coating I.

Refer to Table A.10 (Appendix A) for the tabulated results from the test period for coating J. Figure 3.27 shows example contact angle measurements and the top view of coating J. Figure 3.28 shows Coating J under Alicona optical microscope at 20x magnification. Figure 3.29 exhibits the plot of ARF and CAH versus number of cycles for coating J.

Refer to Table A.11 (Appendix A) for the tabulated results from the test period for coating K. Figure 3.30 shows example contact angle measure-

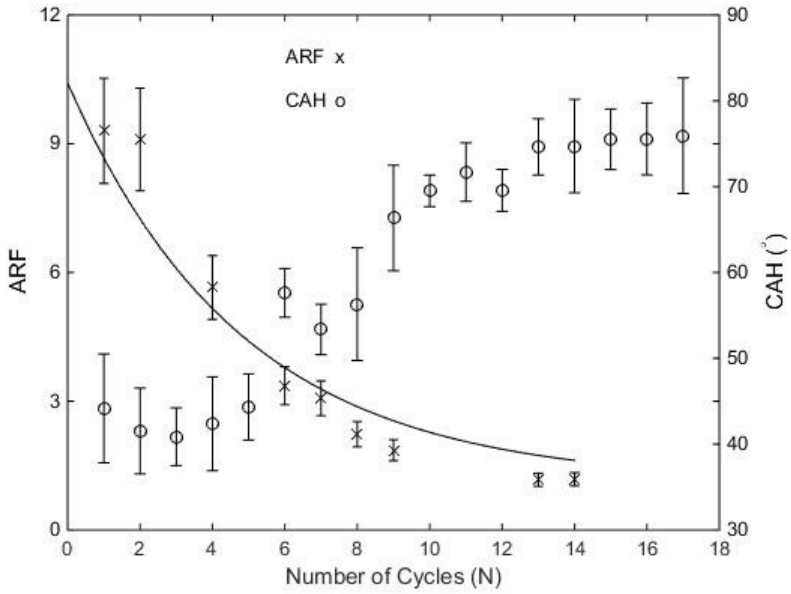


Figure 3.10: ARF and CAH versus number of cycles for coating D.

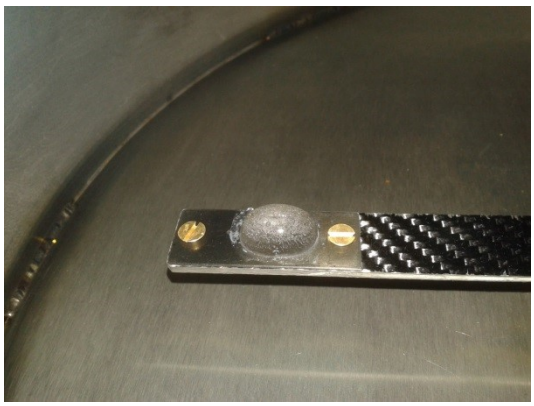


Figure 3.11: Ice attached to coating E inside environmental chamber.

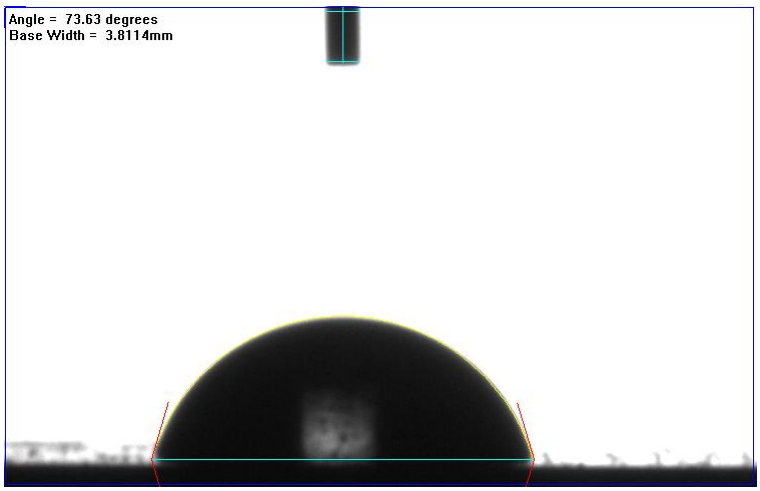


Figure 3.12: Static contact angle measurement example of coating E prior to testing.

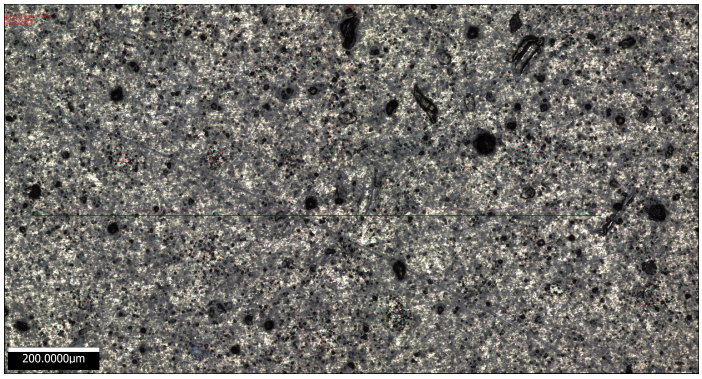


Figure 3.13: Coating E under Alicona optical microscope at 20x magnification.



Figure 3.14: Ice attached to coating F inside environmental chamber.

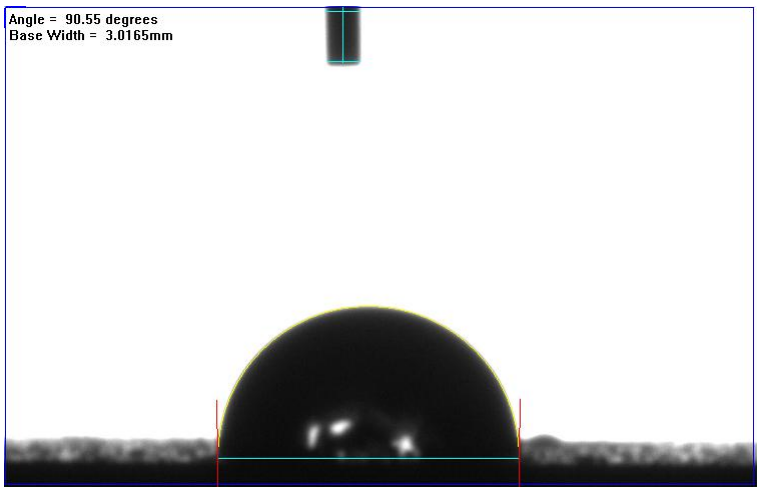


Figure 3.15: Static contact angle measurement example of coating F prior to testing.

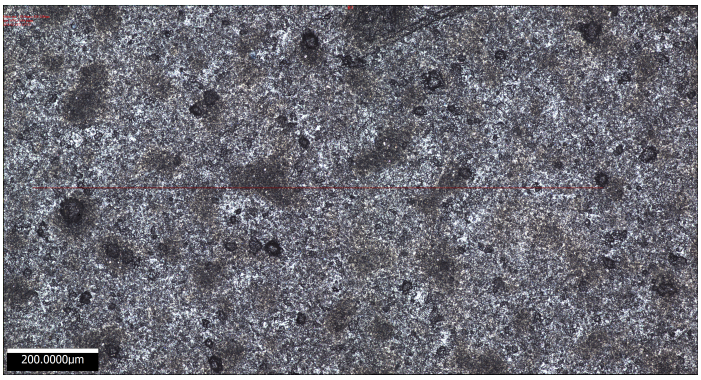


Figure 3.16: Coating F under Alicona optical microscope at 20x magnification.



Figure 3.17: Coating G after cycle 2. The ice shearing off visibly removed the coating clearly indicating poor adhesion to the substrate.

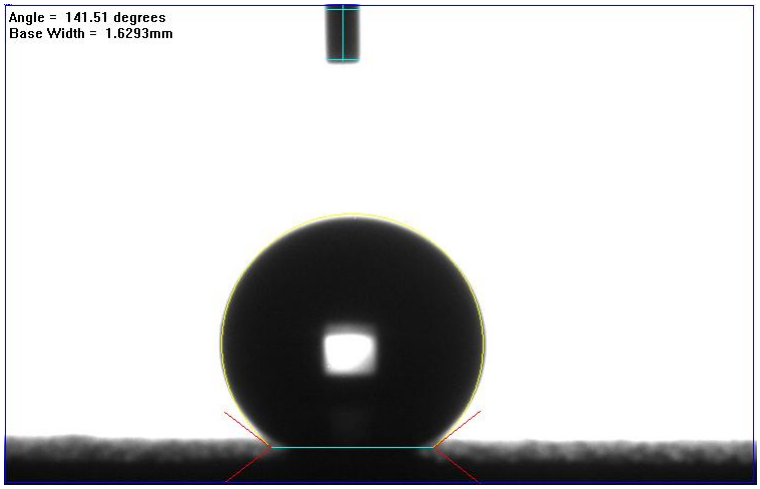


Figure 3.18: Static contact angle measurement example of coating G prior to testing.

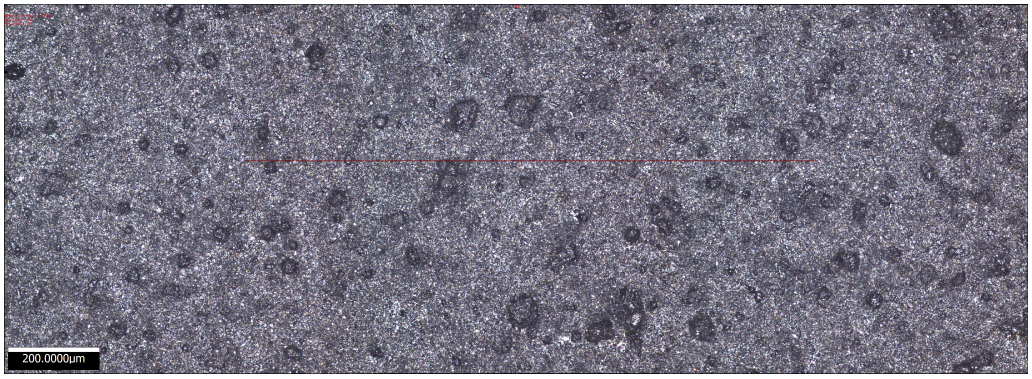


Figure 3.19: Coating G under Alicona optical microscope at 20x magnification.

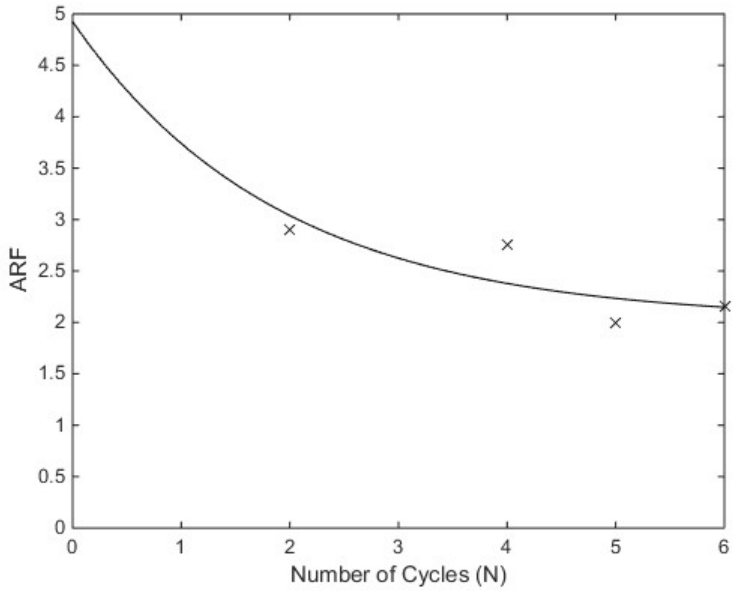


Figure 3.20: ARF versus number of cycles for coating G.

ments and the top view of coating K. Figure 3.31 exhibits the plot of ARF and CAH versus number of cycles for coating K.

Refer to Table A.12 (Appendix A) for the tabulated results from the test period for coating L. Figure 3.32 shows example contact angle measurements and the top view of coating L. Figure 3.33 exhibits the plot of ARF and CAH versus number of cycles for coating L.

Refer to Table A.13 (Appendix A) for the tabulated results from the test period for coating M. Figure 3.34 shows example contact angle measurements and the top view of coating M. Figure 3.35 exhibits the plot of ARF

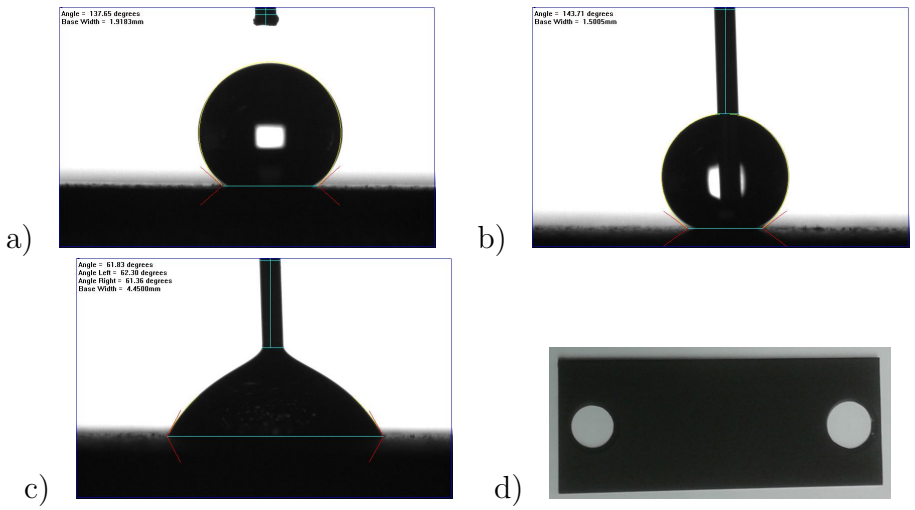


Figure 3.21: Example measurements of 1) Static (137.65°), 2) Advancing (143.71°), 3) Receding contact angle (61.83°) respectively for Coating H. 4) shows the top view of the coating.

and CAH versus number of cycles for coating M.

Refer to Table A.14 (Appendix A) for the tabulated results from the test period for coating N. Figure 3.36 shows example contact angle measurements and the top view of coating N. Figure 3.37 exhibits the plot of ARF and CAH versus number of cycles for coating N.

3.5 Analysis

Table 3.4 shows the summary of test results for coatings A–N.

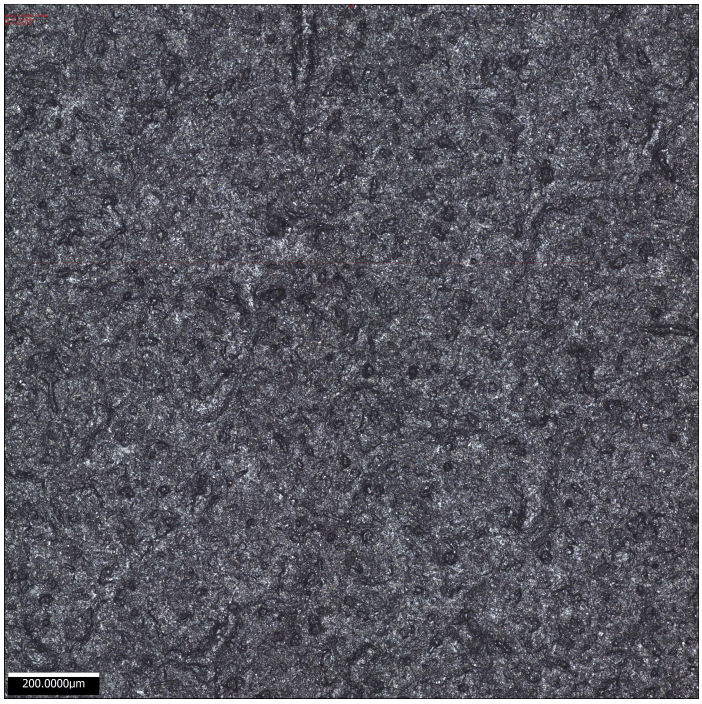


Figure 3.22: Coating H under Alicona optical microscope at 20x magnification.

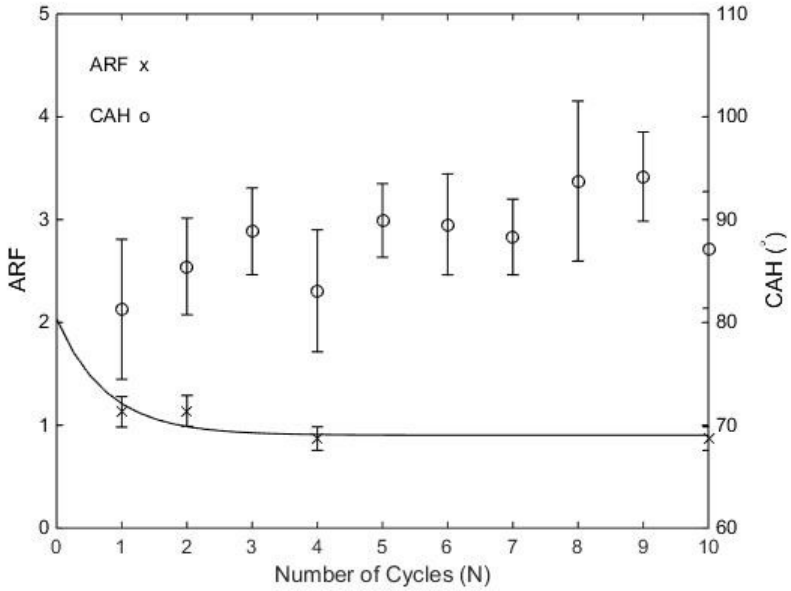


Figure 3.23: ARF and CAH versus number of cycles for coating H.

Table 3.4: Summary of test results for Coating A-N.

Coating	**Number of Cycles**	**Mould Failure**	**Partial Detachment**	**No Detachment**	**Successful Tests**
A	17	2	1	0	14 (82.4%)
B	17	5	3	0	9 (52.9%)
C	17	3	5	0	9 (52.9%)
D	17	6	2	0	9 (52.9%)
E	6	0	0	5	1 (16.7%)

F	6	0	0	5	1 (16.7%)
G	6	2	0	0	4 (66.7%)
H	10	0	0	6	4 (40%)
I	10	3	1	0	6 (60%)
J	10	0	0	7	3 (30%)
K	10	3	1	0	6 (60%)
L	10	0	1	5	4 (40%)
M	10	1	0	4	5 (50%)
N	10	3	0	0	7 (70%)

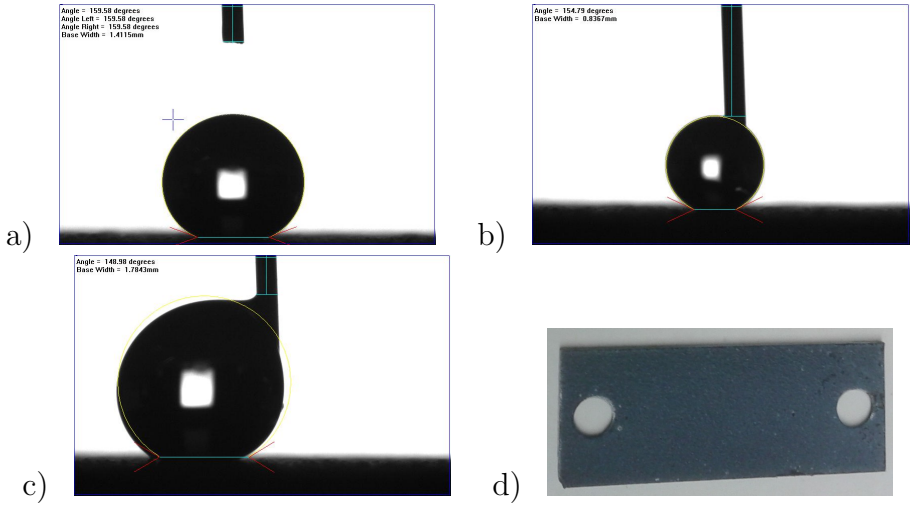


Figure 3.24: Example measurements of 1) Static (159.58°), 2) Advancing (154.79°), 3) Receding contact angle (148.98°) respectively for Coating I. 4) shows the top view of the coating.

The performance of coatings A—N, as indicated by their adhesion reduction factor (ARF) and contact angle hysteresis (CAH), was evaluated over 10 cycles (17 cycles for A—D) of ice growth and detachment, shown in the previous section. These data show qualitatively that adhesion reduction factor is correlated with CAH. As the sample goes through successive cycles of ice growth and detachment its icephobicity, as indicated by adhesion reduction factor, reduces and the CAH increases. Data where the adhesion test failed due to e.g. only partial detachment of the ice from the rotor, or poor attachment of the mould to the substrate when growing the ice, are not included (for example coating A, cycle 8, Figure 3.4).

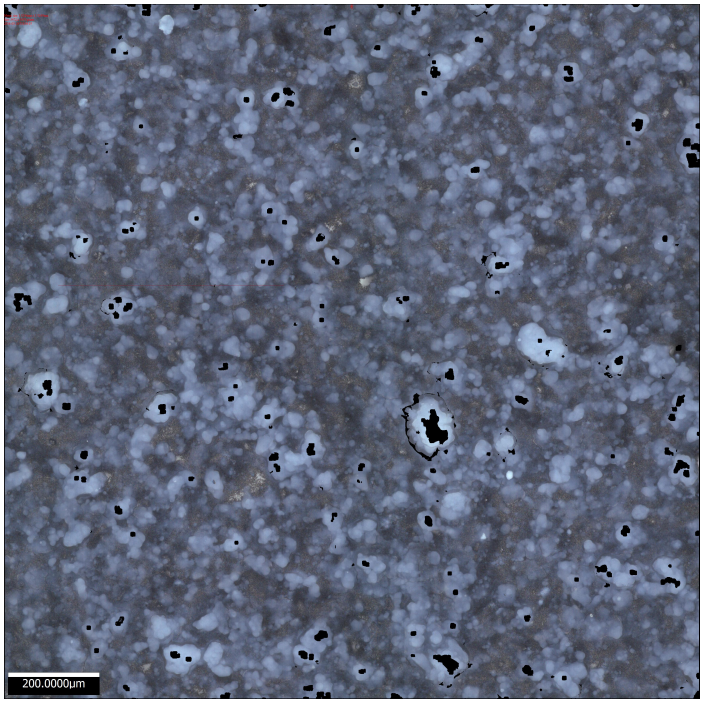


Figure 3.25: Coating I under Alicona optical microscope at 20x magnification.

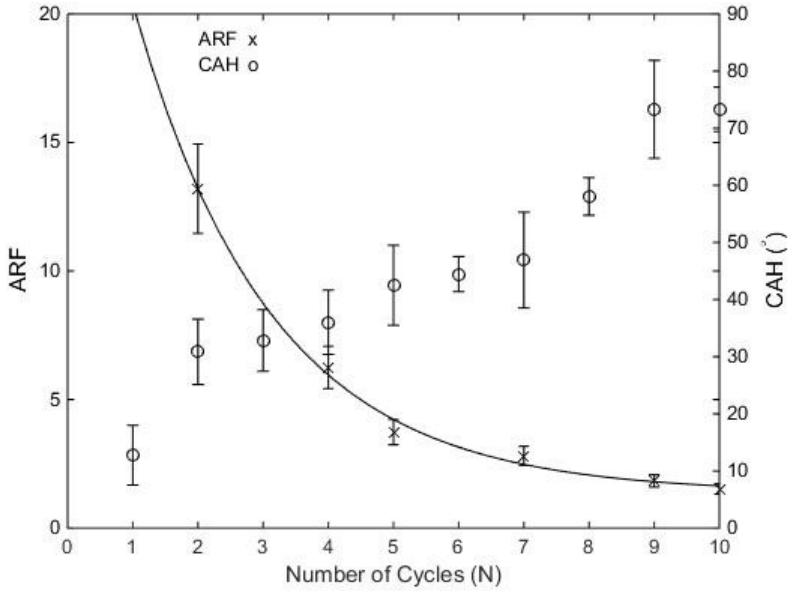


Figure 3.26: ARF and CAH versus number of cycles for coating I.

From the previous section, Coating N qualitatively appears to have performed the best over the initial portion of the test period. The 3 highest adhesion reduction factors were measured for Coating N (60.55) and Coating B (20.5, 17.5) in the first and first two cycles respectively, corresponding to highest levels of icephobicity. From Table 3.5 however, we can see that the retained icephobicity of A and B is significantly greater than N. Since the results for A, B, C and D are within the error limits for ARF itself (i.e. 13.2%), the repeatability and accuracy of our test procedure is confirmed since the two types of coatings were produced under identical conditions.

Table 3.5: Coating decay rates and retained icephobicity values of Coatings A—N. *Extrapolated values since test results from first cycle were invalid.

Coating	**Coating Wear Rate,** α	**Initial ARF,** ARF_1	**Retained icephobicity,** $C.ARF_1$	**Ranking (min** α**)**	**Ranking (max** C**)**
A	0.26	17.00	1.7	4	2
B	0.27	20.50	1.8	5	1
C	0.21	6.50	1.0	2	5
D	0.22	9.30	1.1	3	4
E	N/A	N/A	N/A	-	-
F	N/A	N/A	N/A	-	-
G	0.12	3.60	0.83	1	12
H	1.30	1.1	0.9	10	10
I	0.47	20.40*	0.9	6	10
J	1.00	1.55	1.0	8	5
K	27.20	0.93	1.0	13	5
L	4.65	1.03*	1.0	11	5
M	14.10	0.91	1.0	12	5
N	1.22	197.1*	1.3	9	3
Uncoated	0.78	1.2*	0.8	8	13

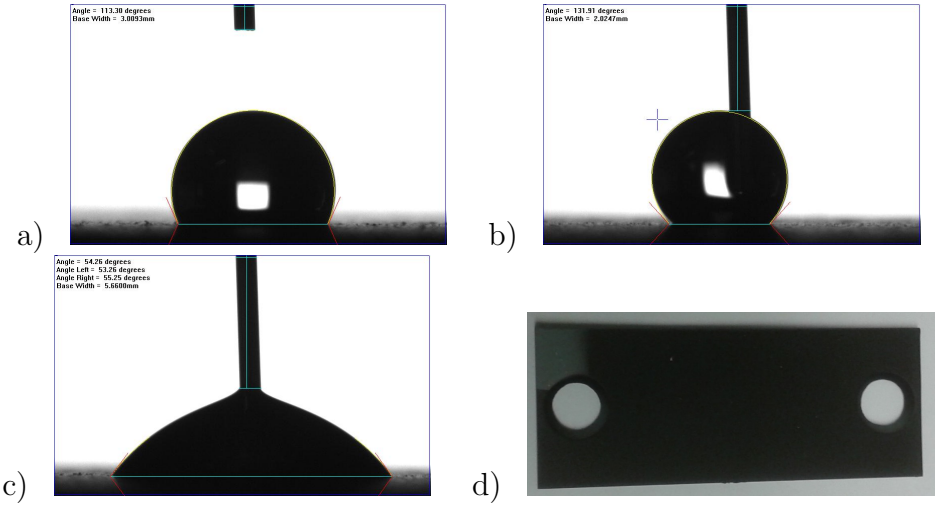


Figure 3.27: Example measurements of 1) Static (113.38°), 2) Advancing (131.91°), 3) Receding contact angle (54.26°) respectively for Coating J. 4) shows the top view of the coating.

Table 3.5 shows initial adhesion reduction factor (ARF(1)) together with the coating durability rates, α, and retained icephobicity, (ARF(N)), derived from a least squares optimization to the fit equation 3.1.

Of the silica nanoparticle coatings, the additional heat treatment of 2 hours at 550°C during preparation of coatings C and D, compared with coatings A and B appears to have reduced the icephobic properties. The initial adhesion reduction factor (ARF(1)) of coating C is 2.6 times less than for coating A and 3.1 times less than coating B respectively. Similarly, for coating D, the initial adhesion reduction factor is 1.8 times less than coating A and 2.2 times less than coating B. However, the heat treated coatings C

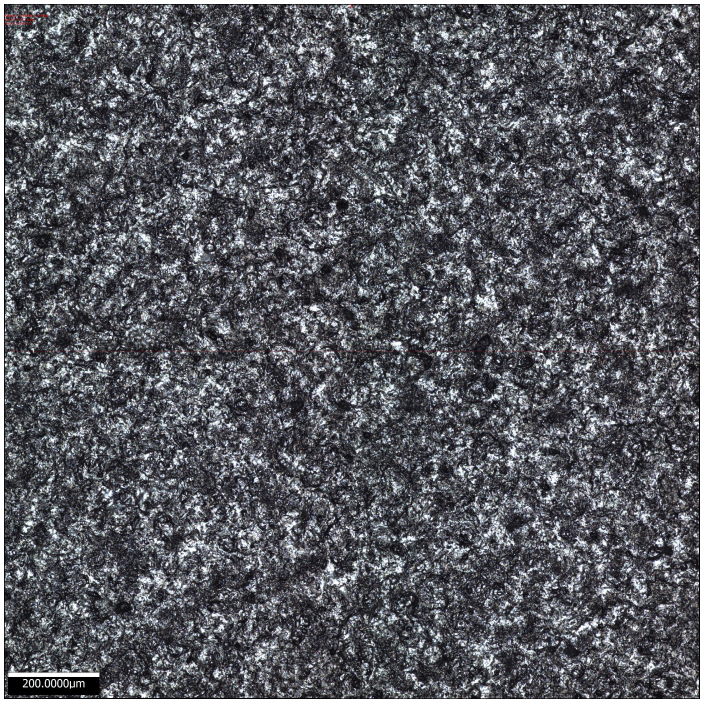


Figure 3.28: Coating J under Alicona optical microscope at 20x magnification.

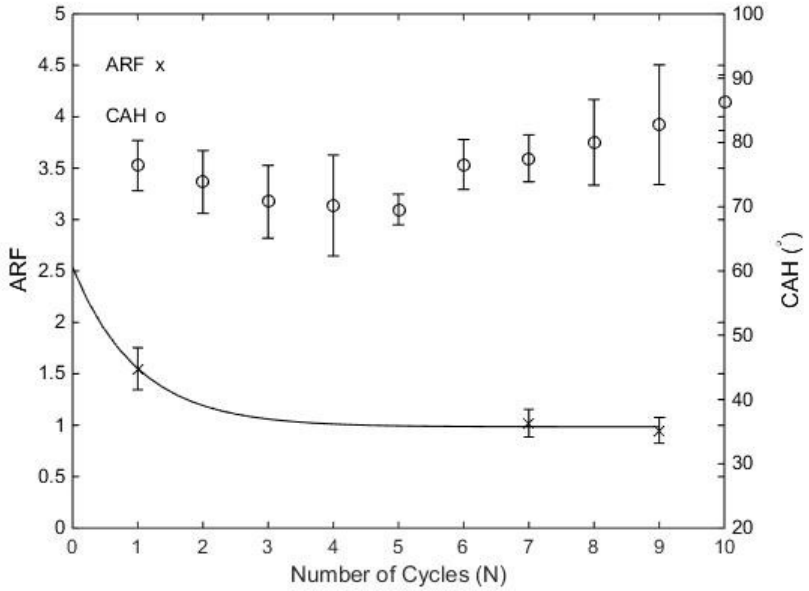


Figure 3.29: ARF and CAH versus number of cycles for coating J.

and D have a slower wear rate than coatings A and B. This implies that the additional heat treatment reduced the initial icephobic quality of the surface but ensured that surface has a longer durability than A and B.

Carbon nanotube coatings H, J, K, L and M had low levels of icephobicity since, in multiple adhesion tests, the ice did not detach from the rotor by the time the maximum speed was reached (4500 rpm). Although all five coatings were hydrophobic, the CAH was initially high (listed in Tables 3.1 and 3.2) and remained high over the test cycles. During the 4 adhesion tests for coating H where the ice did detach, the adhesion reduction factor

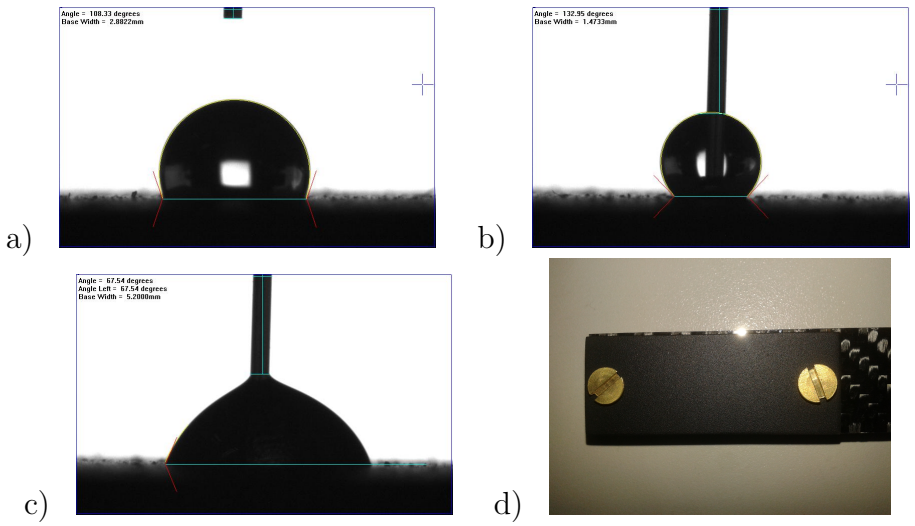


Figure 3.30: Example measurements of 1) Static (108.33°), 2) Advancing (132.95°), 3) Receding contact angle (67.54°) respectively for Coating K. 4) shows the top view of the coating.

was in the range 0.87–1.15, evidencing the low icephobicity. However, for this coating the CAH varied very little, remaining at 88.08 ± 4.14° over the 10 cycles. This shows that the coating has maintained its surface properties well over the cycles. Similarly, for coating J in 3 successful tests, the adhesion reduction factor remains in the range 0.95–1.55, exhibiting low icephobicity, and the coating also maintained its surface properties well over the test cycles. K, L and M showed similar characteristics during the test period.

Figure 3.38 shows the ice adhesion versus static, advancing, receding and contact angle hysteresis for all 11 coatings and 20 uncoated substrates

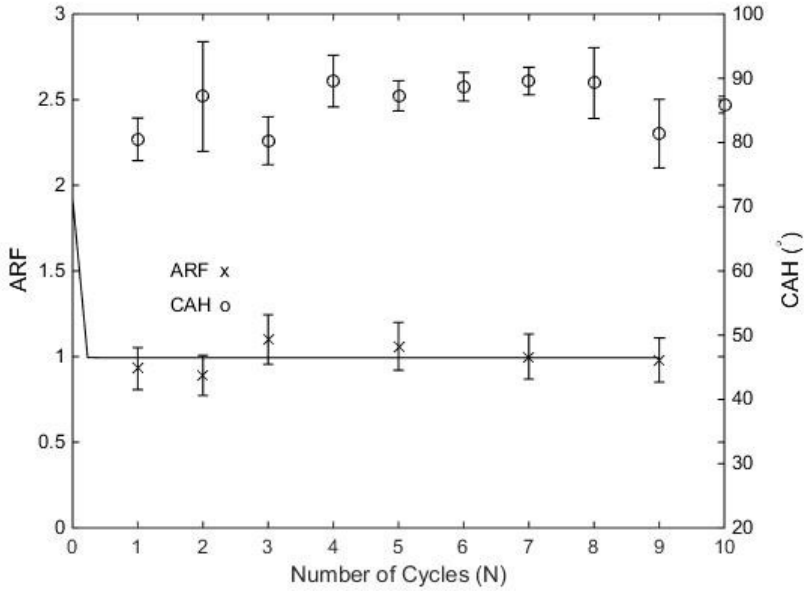


Figure 3.31: ARF and CAH versus number of cycles for coating K.

throughout the test period for ready comparison to the literature [7, 30, 61, 72, 65]. The best fit was found to be a Gaussian curve with relation to the change in ice adhesion versus CAH (figure 3.38d). The equation of the Gaussian fit is given as:

$$Y = Ae^{-[(X-B)/C]^2} \tag{3.2}$$

Where the coefficients (with 95% confidence bounds) are: A = 160.8 kPa (152.4 kPa, 169.2 kPa), B = 91.97° (88.42°, 95.53°) and C = 35.76° (32.18°, 39.34°). Importantly, we see that the ice adhesion strength increases

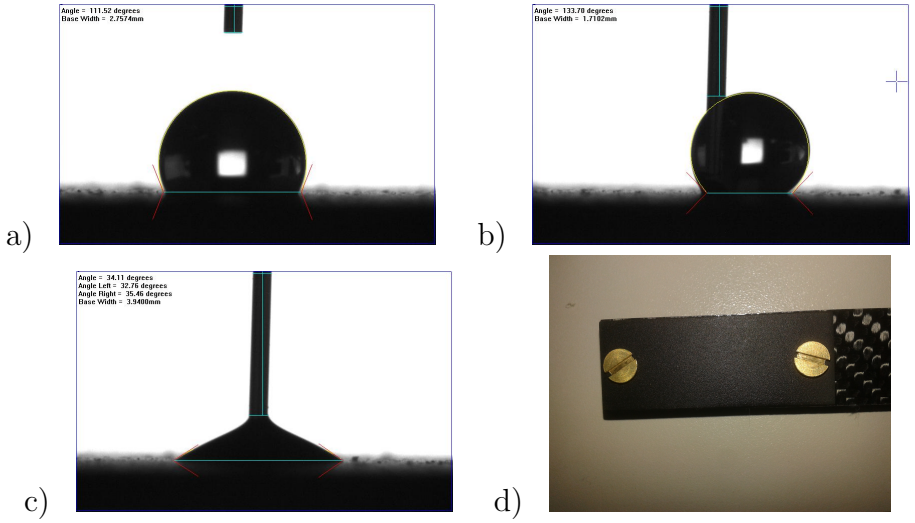


Figure 3.32: Example measurements of 1) Static (111.52°), 2) Advancing (133.78°), 3) Receding contact angle (34.11°) respectively for Coating L. 4) shows the top view of the coating.

with respect to CAH to a maximum value of 160.8 kPa at 91.97° (∼92°). The reason for this can be explained by the increased ice-coating contact area that would be apparent for coatings having a high CAH. In figure 3.38d), when CAH $\geq\sim$ 92°, the adhesion strength reduces with increase in CAH. The reason for this phenomenon in the trendline is that coatings with high CAH coupled with high surface roughness, can cause pockets of air bubbles to form at the ice/coating interface [61]; thereby reducing adhesion strength. Importantly, figure 3.38d) indicates that already at CAH values of ∼25°, adhesion strength is close to zero.

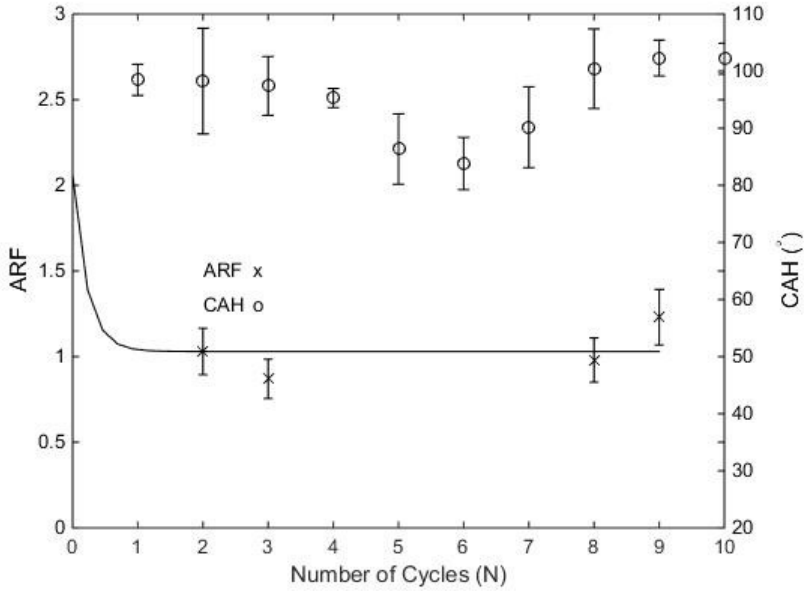


Figure 3.33: ARF and CAH versus number of cycles for coating L.

Figure 3.40 shows the adhesion strength versus CAH for SS 304, Al 6082-T651 and Al 1050A-H14 in comparison to Gaussian best fit from equation 3.2. We note that change in shape of the ice from cuboid to coffee bean mould has limited effects on the calculation of adhesion strength. This therefore reiterates the repeatability of the experimental setup.

Figure 3.39 shows the SEM micrographs of coating K before (a) and after (b) the ice adhesion tests. CNTs are clearly visible in both micrographs while a smoother surface remains after the ice adhesion tests. The procedure of surface smoothening may be attributed to removal of bigger CNT bundles

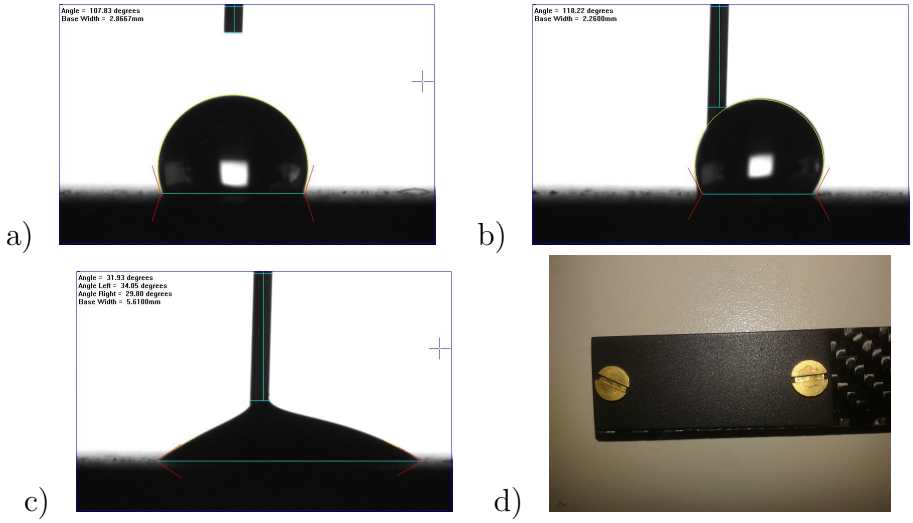


Figure 3.34: Example measurements of 1) Static (107.83°), 2) Advancing (118.22°), 3) Receding contact angle (31.93°) respectively for Coating M. 4) shows the top view of the coating.

protruding from the outer part of the coating as shown in Figure 3.39a which have been removed with ice following a mechanism proposed by Ling et al. (2016) [73]. They observed that during freezing, the tips of the carbon nanotubes deposited on stainless steel substrate become embedded within the ice phase and are ripped off of the substrate when the ice column is sheared from the mesh. However, in our case, such a mechanism, if present, is limited as we can still observe the presence of CNTs after the ice adhesion testing. This is because in our case the CNTs coating is well adhered to the aluminium substrate and retains its integrity after multiple cycles of icing and de-icing.

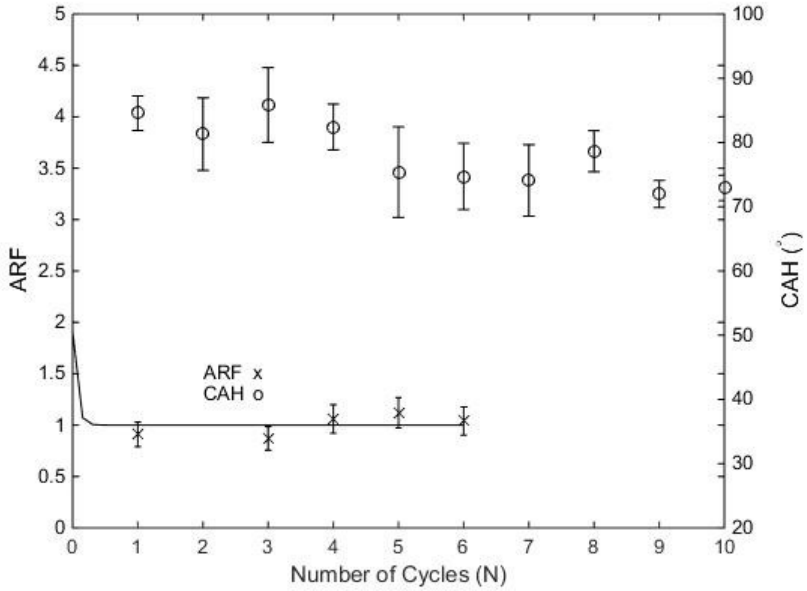


Figure 3.35: ARF and CAH versus number of cycles for coating M.

Kulinich and Farzaneh [30] employ a linear fit for adhesion strength versus CAH, but the fit covers a smaller CAH range (60–95°) and only 10 data points. Meuler et al. (2010) [65] find a linear correlation between adhesion strength and a parameterized CAH x-axis i.e. $\cos(\theta_{rec}–\theta_{adv})$; but consider only cases with $\theta_{adv} \geq 105°$ and the fit does not extend to the origin. When $\theta_{adv} \leq 100°$, the ice adhered much more strongly to the substrate than anticipated according to the fit. They also find a linear fit with adhesion strength versus $(1 + \cos\theta_{rec})$ plotting data from 22 substrates when the adhesion strength and contact angle parameters were calculated only once for each substrate result.

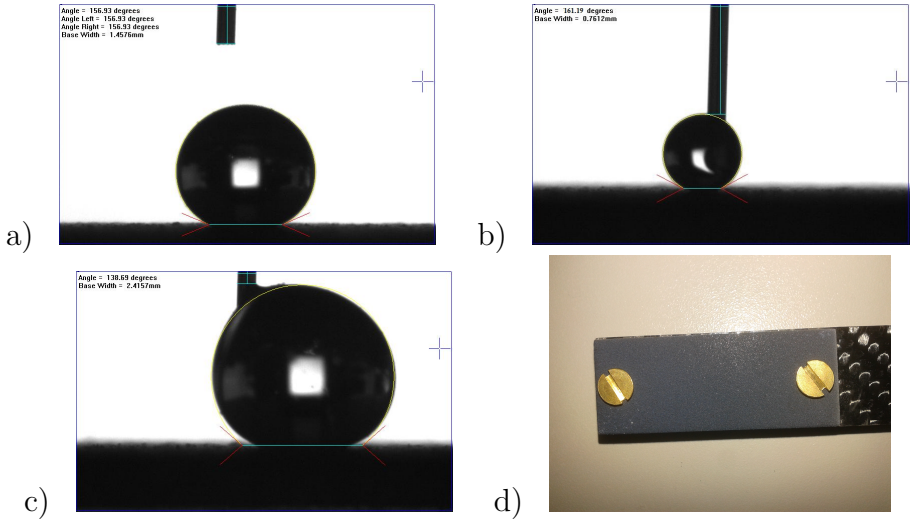


Figure 3.36: Example measurements of 1) Static (156.93°), 2) Advancing (161.19°), 3) Receding contact angle (130.69°) respectively for Coating N. 4)

shows the top view of the coating.

Our results however indicate that two surfaces with different receding angles (55° and 105°) can have similar adhesion strengths (see Figure 3.38c); and it is the CAH which is the dominant parameter determining adhesion strength. It must be noted that figure 3.38d) exhibits the degradation of the coating and the plot of the subsequent change in adhesion strength with measurements of contact angle parameters for the coatings. This is in contrast to Meuler et al. (2010) [65] who calculate adhesion strength and contact angle parameters only once for each substrate result. No apparent trend can be seen with respect to static and advancing contact angle with regards to the ice adhesion, implying the interaction of water with a surface is

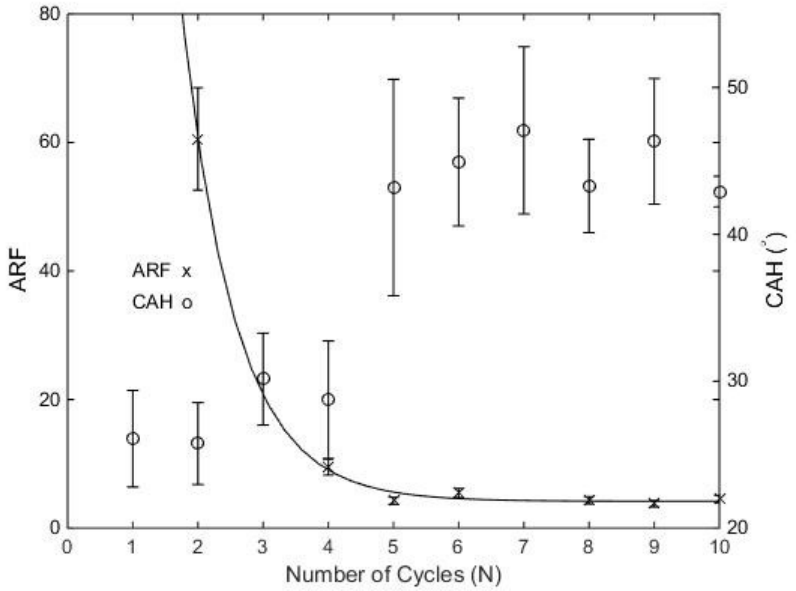


Figure 3.37: ARF and CAH versus number of cycles for coating N.

very different to the interaction of that same surface with ice. This has been well corroborated in the previous work [30, 65]. Results from our test period corroborate this, since certain hydrophobic coatings behaved "icephillic" when exhibiting high CAH.

From Figure 3.38 and observations during testing, it is also apparent that repeated tests using the centrifuge with the ice shearing off the coating surface, had a minimal impact on changes in the static and advancing contact angles as compared to the pronounced changes (reduction) in the receding contact angle in coatings A, B, C, D, I and N. For coatings H, J, K, L and

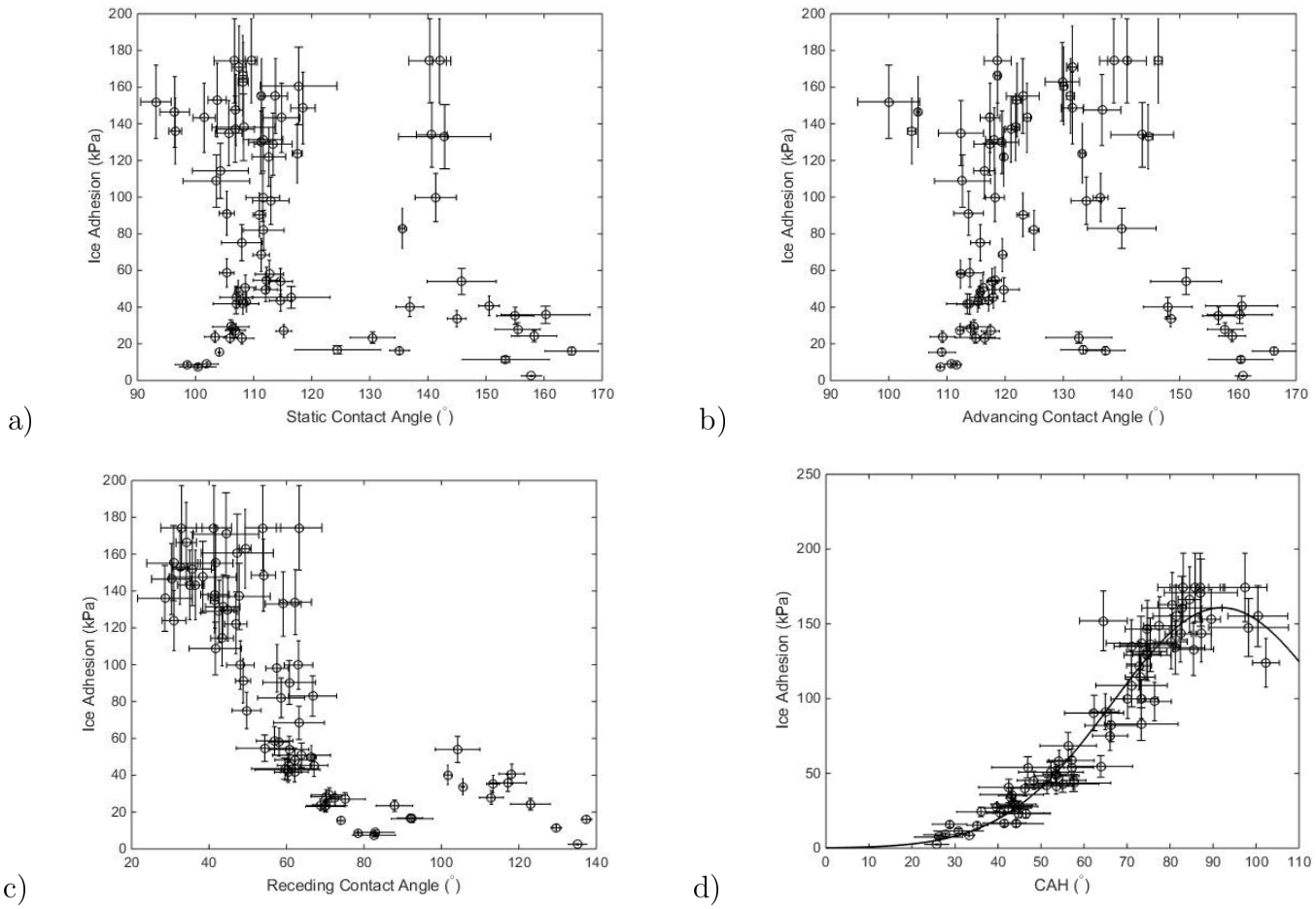


Figure 3.38: Ice adhesion for all 14 coatings versus a) Static, b) Advancing, c) Receding contact angle and d) Contact angle hysteresis.

M; static, advancing and receding values stayed near constant through the test period with poor icephobicity. This finding leads to an overall dominant impact of the CAH on the ice adhesion strength but it is an interesting phenomenon to explore. The reason for the change in receding angle with repeated tests as compared to static and advancing contact angle could be the method of removal of the ice sample as it shears off and removes part of the coating surface (as noticed on visual observation). The receding contact angle would be affected more than the static and advancing contact angle due to its more intricate dependence on time since it is a measurement of "de-wetting". It is possible that the shearing of the ice exposed the encapsulated air pockets in the coatings due to deposition of the nanoparticles. The increased surface area would affect the receding angle greatly and the time taken for the de-wetting process.

3.6 Conclusion

The anti-icing performance of 14 coatings, some with silica nanoparticles and others incorporating carbon nanotubes, has been evaluated; candidates for application to the surface of aircraft wings to prevent the accretion of runback ice. The ice adhesion strength, together with the development of

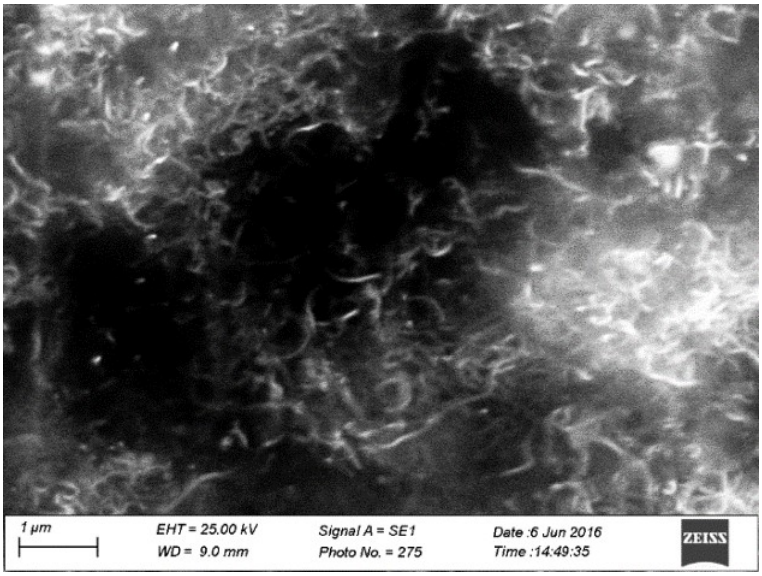
surface characteristics, was measured over multiple cycles of glaze ice growth and detachment from the coated substrate.

The development of icephobicity was characterized by a retained icephobicity, that is, the long term chemical or mechanical alteration the coating has made to the substrate surface, and the durability rate. This data shows that initially strong icephobic performance typically wears quickly, and that the retained icephobicity is not necessarily linked to initial coating performance. Thus, for the silica nanoparticle and polystyrene coatings, heat treatment led to reduced initial and long term icephobicity in comparison with the non-heat treated equivalents, however, the wear rate of the former was lower than the latter. For the carbon nanotube composite coatings, best results were obtained for the coating with 5% and 20% functionalised carbon nanotube content with use of an interlayer between the coating and the substrate and deposition of a final surface promoter respectively. The inclusion of an interlayer and final surface promoter is crucial in ensuring icephobicity of the surface. The surface roughness of these two coatings is higher than the coating with 10% functionalised carbon nanotube content and similar characteristics by an order of 2 and 2.3 respectively. This is why the coating does not perform well in addition to also having a high CAH.

In support of findings from previous studies [30], increasing ice ad-

hesion is well correlated to increasing contact angle hysteresis up to CAH = ∼92°. Lower CAH reduces the ice-solid area of contact and thus the energy of the adhesive bond. Above CAH of ∼92°, our data indicates from figure 3.38d) that adhesion strength reduces. This could be due to the presence of air pockets on rough surfaces contributes to reducing the bond between ice and the surface and requires further investigation. Importantly, at CAH values of ∼25°, the adhesion strength is very close to zero; indicating a reduced effect of lower CAH values than previously assumed. Icephobicity does not necessarily correlate with hydrophobicity. The greater reduction in receding contact angle as compared to static and advancing contact angle over the test period can be attributed to the fact that the removal of ice affects the surface characteristics of the coatings, increasing the surface area of contact and eventually increasing time for the de-wetting process. For runback icing in particular, high static and advancing contact angles are recommended to prevent wetting by runback water before it eventually freezes. To reduce the ice adhesion after freezing, the surface should possess high receding contact angle and low CAH.

a)



b)

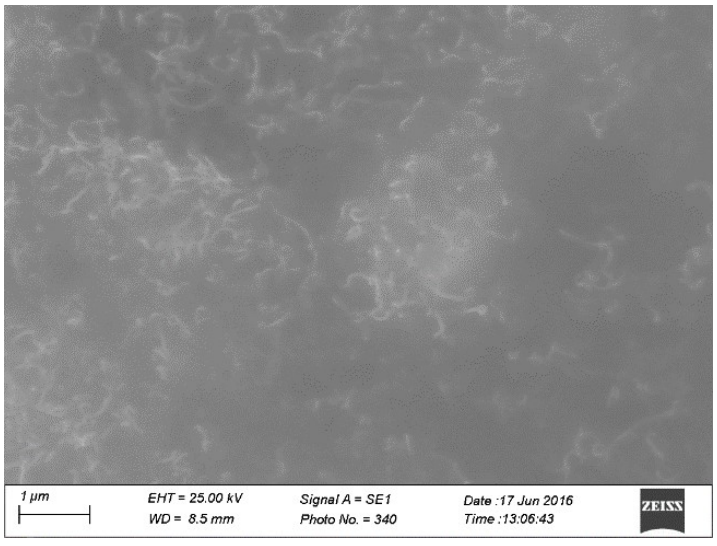


Figure 3.39: SEM micrographs of sample K at a magnification of 30000X obtained (a) before and (b) after the ice adhesion tests.

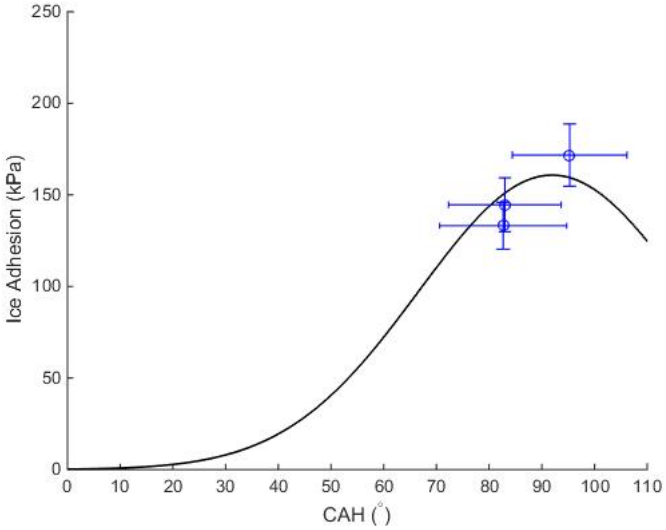


Figure 3.40: Adhesion strength versus CAH plotted for SS 304, Al 1050A-H14 and Al 6082-T651 in comparison to Gaussian best fit from equation 3.2.

Chapter 4

Static Anti-icing Adhesion Tests using Icephobic Coatings

4.1 Introduction

The de-icing ability of icephobic coatings can be evaluated through shear stress measurements, as discussed in Chapter 3. Prior to the removal of ice, delay in the freezing time of an incident droplet termed the "anti-icing" ability, is an industrial term in the aeronautical industry defined as the prevention of ice formation on a surface. This is a significant property of a surface that can be theoretically manipulated by design. In this respect, sev-

eral researchers have studied the freezing time and temperature transition of a water droplet when it impacts a surface at sub-zero temperatures. The freezing of a droplet can be described in the following four stages [74]:

1. The droplet lands on the surface. This process is significantly slower ($0.3\,\mathrm{m\,s^{-1}}$) than an actual supercooled droplet impacting an aerofoil ($\sim 90\,\mathrm{m\,s^{-1}}$).

2. The droplet cools from an initial temperature to below T_f until crystal nucleation occurs.

3. Crystal kinetic growth from the crystal nuclei is rapidly seen until supercooling has finished and the droplet reaches T_f.

4. The liquid droplet now freezes completely at T_f depending upon the heat transfer rate at the solid surface and the ambient.

5. The entirely frozen droplet now equilibrates to the ambient air temperature.

In Chapter 4, we investigate anti-icing ability of the same coatings tested for de-icing characteristics in Chapter 3 through a freezing droplet time calculation.

Hindmarsh et al. (2003) [75] conducted numerical and experimental work on freezing 0.5–2 x 10^{-3} ml droplets between -30°C and -15°C air temperature. Instead of impacting a sub-zero surface, the droplets were sus-

pended on a thermocouple with wind speed of 0.42–0.97 $\mathrm{m\,s^{-1}}$. This work was built upon by Chaudhary and Li (2014) [76] but in both cases, contact angle parameters of the droplet on a surface were not measured. To measure the impact of superhydrophobic/icephobic surfaces on the delay time in freezing of a droplet, different coating types were evaluated for freezing time versus contact angle parameters: silicone acrylate resin [77, 78]; fluoroalkylsilane [79], SU-8 photoresist (MicroChem Corporation) [80], PTFE and styrene butadiene rubber [81]. Huang et al. (2012) found that by increasing the static contact angle of a copper surface from 76° to 154° by increasing the surface roughness and using a fluoroalkylsilane coating, the freezing time increased from approximately 200 s to 500 s [79]. Similarly, Ozbay et al. (2016) [81] found that increasing equilibrium contact angle by 25°, resulted in a freezing time 6 times greater. Along with high surface roughness [80], high static and equilibrium contact angle can reduce the actual water-solid contact area on the surface of the coating; thereby reducing the overall surface area for heat transfer and subsequent freezing. This is the key hypothesis that we wish to test for coatings E–N that have been previously evaluated for de-icing ability in Chapter 3 (ICECOAT-CleanSky).

In this chapter, we conduct anti-icing tests to measure the time taken to freeze a water droplet. The freezing times are correlated with con-

tact angle parameters and results are tabulated with anti-icing results from Chapter 3 to determine the best overall coating based on de-icing and anti-icing performance.

4.2 Methodology

Coatings E–N were produced on 50 x 50 x 1 mm Aluminium 6082-T651 substrates for the purpose of initially testing in an icing tunnel. The process of substrate preparation and coating deposition is detailed in Chapter 3. The icing tests were unsuccessful because the tunnel was unable to maintain sub-zero temperatures at wind speeds greater than $20\,\mathrm{m\,s^{-1}}$ that were necessary for maintaining thin film flow for appropriate heat transfer over the aerofoil section. The freezing droplet tests were conceived as an alternative for conducting anti-icing tests. The contact angle parameters such as static, advancing, receding and contact angle hysteresis were re-measured prior to the freezing droplet tests to determine any change of surface properties due to previous icing tunnel tests. The method for measurement of contact angle parameters is detailed in Chapter 3. Coating F was damaged beyond repair during the icing tunnel tests and was not considered for further evaluation.

A table-top cooling plate was used to provide sub-zero conditions

for these freezing droplet tests. It has a stainless steel frame and tub with a maximum cooling temperature of -35°C (Figure 4.1).

A motorized syringe with set flow rate 2.5 ml per hour was used to control the volume of the droplet. Manual and calculated flow rates were measured during 5 identical tests to determine droplet volume as 6.2 $\pm$ 0.27 x 10^{-3} ml. Using the formula for volume of a sphere, diameter of the droplet was calculated as 2.28 $\pm$ 0.03 mm. Uncoated and coated substrates were placed on the plate for 30 seconds before the droplet was released. Tests were conducted at plate temperatures of -5°C and -10°C. Prior to releasing the droplet, a beaded thermocouple was placed on the pre-determined location of droplet impact to measure the local temperature. Similair to the ice adhesion tests in Chapter 3, de-ionised water at 24°C was used in the motorized syringe. Room temperature was maintained at 27.2°C and relative humidity 58%. The distance between the tip of the syringe and substrate was fixed at 18 mm. For a typical Biot number (which is the ratio of the resistance due to conduction to the resistance due to convection [82]) of 0.07, we can invoke lumped analysis and determine that the droplet is not supercooled when it impacts the surface (see Appendix B) and hence is expected to follow the well documented four-stage freezing process [74]. Freezing time was calculated as an average of three tests. The tests were filmed at 24

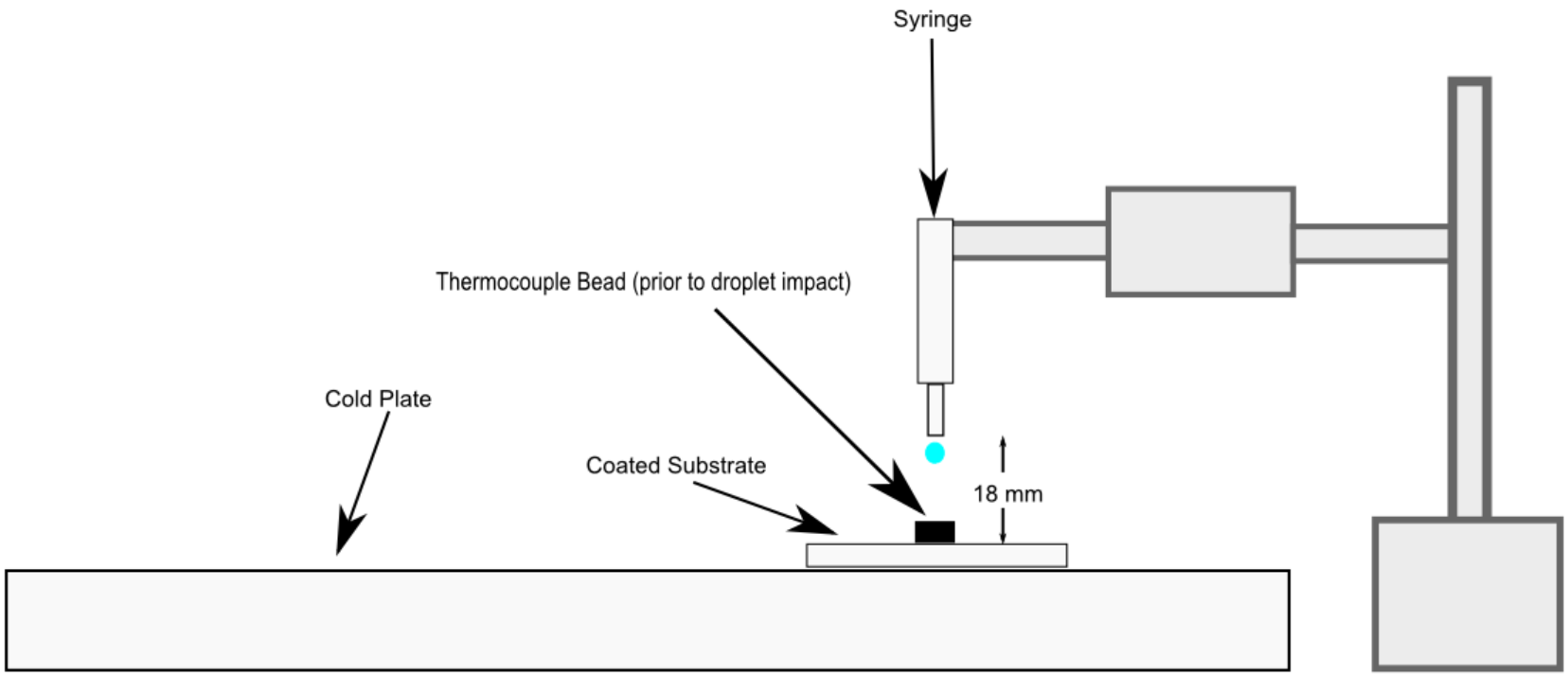


Figure 4.1: Schematic of cold plate setup for icing time measurements of a water droplet.

frames per second and at 10 MegaPixels. Freezing time was determined consequently on visual analysis. Table 4.3 shows how the appearance of the droplet changes as it freezes during a single test at plate temperature -10°C. The time at which the droplet was entirely opaque was assumed to correlate to the freezing time.

Possible sources of error include humidity in the room causing excessive condensation on coating surface, air movement, contamination of water and variation in thermocouple temperature measurements.

4.3 Results and Analysis

Table 4.1 shows the test data for the bare and coated substrates. The larger variation seen for coating N at -5°C is due to its larger static contact angle, implying a larger surface area is in contact with the ambient rather than the substrate, causing a change in the freezing pattern. Table 4.2 shows the contact angle parameters measured for each substrate. Table 4.3 shows the freezing process at -10°C for the bare and uncoated surfaces. For all the surfaces barring coating I and N, freezing was observed from the substrate upwards since a larger area of the droplet was in contact with the substrate. For coating I and N, which had the highest SCAs of 129.42 ± 2.43° and

134.86 ± 6.7° respectively, freezing was initially noticed from the outer surface inwards; before eventually following the pattern of freezing seen in the other coatings.

Table 4.1: Test data for the uncoated and coated substrates.

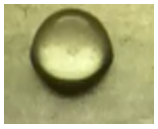
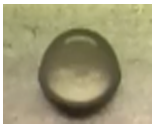
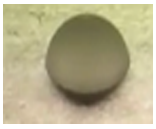
Coating	**Plate Temperature (°C)**	**Thermocouple Temperature (°C)**	**Freezing Time (s)**
Al 6082-T651	-5	-5.03 ± 0.21	10.13 ± 0.3
Al 6082-T651	-10	-10.1 ± 0.2	5.47 ± 0.12
E	-5	-5.13 ± 0.21	7.3 ± 0.36
E	-10	-10 ± 0.2	4.57 ± 0.25
G	-5	-5 ± 0.3	10.73 ± 0.64
G	-10	-10 ± 0.3	8.77 ± 0.35
H	-5	-5.13 ± 0.3	10.8 ± 0.26
H	-10	-10 ± 0.3	8.73 ± 0.67
I	-5	-5.1 ± 0.3	14.53 ± 0.91
I	-10	-10.13 ± 0.15	11.07 ± 0.51
J	-5	-5.2 ± 0.3	13.73 ± 0.15
J	-10	-10.23 ± 0.31	11.33 ± 0.15
K	-5	-5.07 ± 0.3	11.8 ± 0.17

K	-10	-10.1 ± 0.26	8.7 ± 0.17
L	-5	-5.26 ± 0.15	12.4 ± 0.52
L	-10	-10.03 ± 0.32	10.73 ± 0.76
M	-5	-4.93 ± 0.21	10.33 ± 0.15
M	-10	-10.13 ± 0.15	8.87 ± 0.9
N	-5	-5.2 ± 0.2	16.37 ± 2.61
N	-10	-10.23 ± 0.15	11.1 ± 0.6

Table 4.2: Contact angle parameters for all substrates.

Coating	**SCA(°)**	**ACA(°C)**	**RCA(°C)**	**CAH(°C)**
Al 6082-T651	82.27 ± 1.6	84.24 ± 2.89	10.87 ± 1.65	73.37 ± 3.33
E	77.16 ± 5.64	87.17 ± 0.52	8.1 ± 2.84	79.07 ± 2.88
G	114.7 ± 3.06	128.19 ± 1.08	85.69 ± 3.51	42.5 ± 3.67
H	107.54 ± 4.89	113.39 ± 2	12.78 ± 2.11	100.61 ± 2.91
I	129.42 ± 2.43	129.1 ± 1.09	47.44 ± 5.04	81.66 ± 5.16
J	125.36 ± 3.36	131.46 ± 1.18	16.12 ± 3.23	115.34 ± 3.52
K	118.4 ± 6.86	128.13 ± 6.24	47.24 ± 4.69	80.89 ± 7.81
L	113.17 ± 0.57	124.53 ± 3.67	27.17 ± 3.26	97.36 ± 4.91
M	97.44 ± 2.7	104.69 ± 0.73	20.1 ± 3.23	84.59 ± 3.31
N	134.86 ± 6.7	136.78 ± 7.92	21.27 ± 5.85	115.51 ± 9.85

Table 4.3: Freezing sequence of water droplet on uncoated and coated surface at -10°C plate temperature.

Coating	**Time 1 (s)**	**Time 2 (s)**	**Time 3 (s)**	**Time 4 (s)**	**Freezing Type**
Al 6082 - T651	0 	1.9 	3.8 	5.6 	Bottom-up
E	0 	1.6 	3.2 	4.8 	Bottom-up
G	0 	3 	6 	9.1 	Bottom-up
H	0 	3.1 	6.2 	9.3 	Bottom-up
I	0	4.1	8.2	11.2	Outwards-in

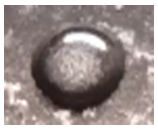
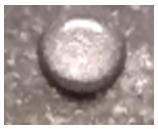
					
J	0 	4.2 	8.4 	11.5 	Bottom-up
K	0 	3 	6 	8.8 	Bottom-up
L	0 	3.3 	6.6 	9.9 	Bottom-up
M	0 	2.6 	5.2 	8 	Bottom-up
N	0 	3.9 	7.8 	11.7 	Outwards-in

Figure 4.2 exhibits the freezing times of droplets at -5°C. Figure 4.3 exhibits the freezing times of droplets at -10°C. As expected, the drop in temperature has a reduction in the overall freezing time of ice. The best fit to the origin for freezing time of the droplets is seen versus static contact angle at -5°C with $R^2 = 0.82$ (Figure 4.4a) and -10°C with $R^2 = 0.79$ (Figure 4.5a). The reason for this dependence is because static contact angle determines the surface area of the droplet in contact with the coating and consequently with the surrounding air. At low static contact angle, a larger surface area of the droplet is in contact with the coating. The thermal mass of the former is much smaller than the latter and the freezing time is rapid. At higher static contact angle, a smaller surface area of the droplet is in contact with the coating. The time taken for freezing to occur from the bottom surface upwards is thus longer. At very high static contact angles, the surface area of the droplet exposed to the surrounding is significantly more than in contact with the coating. In such a scenario, the droplet may begin freezing from the outer surface inwards with heat transported away through convection to the surrounding air and complete freezing may take longer as the bottom surface does not freeze immediately.

A weaker fit to the origin for freezing time is seen with respect to the advancing contact angle. At -5°C, $R^2 = 0.66$ (Figure 4.4b) and -

10°C, $R^2 = 0.73$ (Figure 4.5b). Since the freezing times encountered in this experiment are between 6–17 s, the metastable configuration of the droplet tends towards the true static contact angle value rather than the advancing contact angle which is a dynamic value. Also, since the advancing contact angle is higher than static for a real surface; the quality of the fit reduces when the x-axis parameter is changed. No apparent trend is seen at plate temperature of -5°C with respect to receding contact angle (Figure 4.4c) and CAH (Figure 4.4d); the same observation is prevalent at -10°C for receding contact angle (Figure 4.5c) and CAH (Figure 4.5d). Shen et al. (2015) [83] measured the freezing time at -10°C for 5 different surfaces after calculating apparent contact angle (APCA) and CAH. For specific values of APCA of 56°, 116° and 135°; freezing time was approximately measured as 14, 25 and 30 s. Coating N with a SCA of 134.86 ± 6.7° has freezing time of 11.1 ± 0.6 s at -10°C plate temperature. Since APCA and SCA can vary drastically for a surface depending on its roughness characteristics, no further comparison can be made.

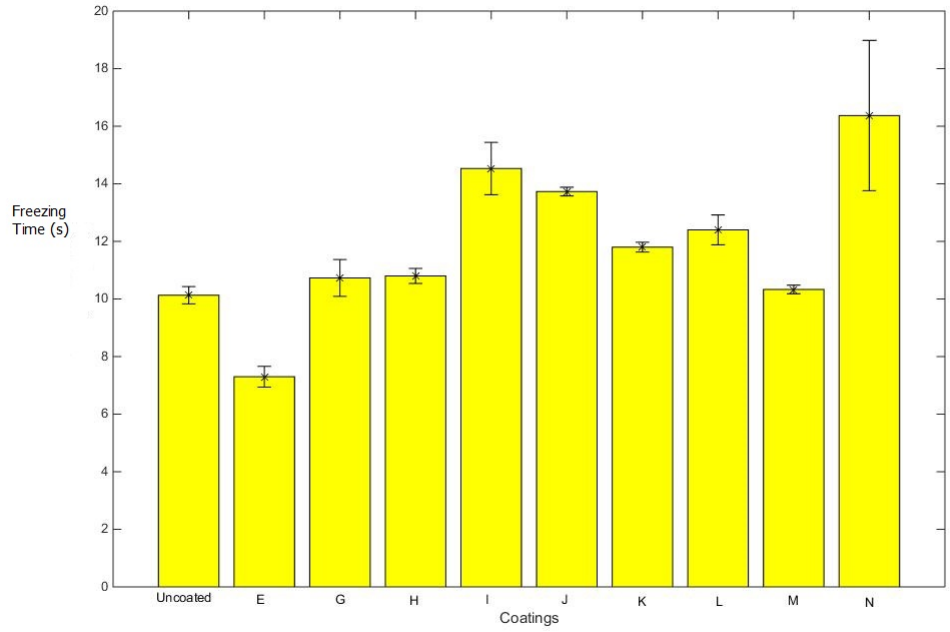


Figure 4.2: Freezing times of droplets at plate temperature of -5°C.

Table 4.4: Overall ranking of the coatings.

Coating	Wear Rate (lowest to highest)	Retained icephobicity (highest to lowest)	Freezing Time at -5°C	Freezing Time at -10°C	Net Coefficient Value
G	1	8	7	6	22
H	5	6	6	7	24
I	2	6	2	3	13

J	3	2	3	1	9
K	8	2	5	8	23
L	6	2	4	4	16
M	7	2	8	5	22
N	4	1	1	2	8

Table 4.4 exhibits the overall coating rankings for the de-icing and anti-icing tests. Although, the surface characteristics of the coatings were degraded before the freezing droplet tests, the results corroborate our hypothesis from the previous chapter regarding suitable characteristics for an effective coating. Coating E and F are excluded because of lack of data in one or more of the four categories. The final column labelled net coefficient value represents the sum total of the rankings from the four columns. The lowest possible value indicates the best coating in this instance. Coating N has been determined to be the best coating with a score of 8. The coating had a high static, advancing and receding contact angle with low CAH. Surface roughness was higher than other coatings by an order of magnitude of 10. Coating J is a close second with similar characteristics. Coatings that

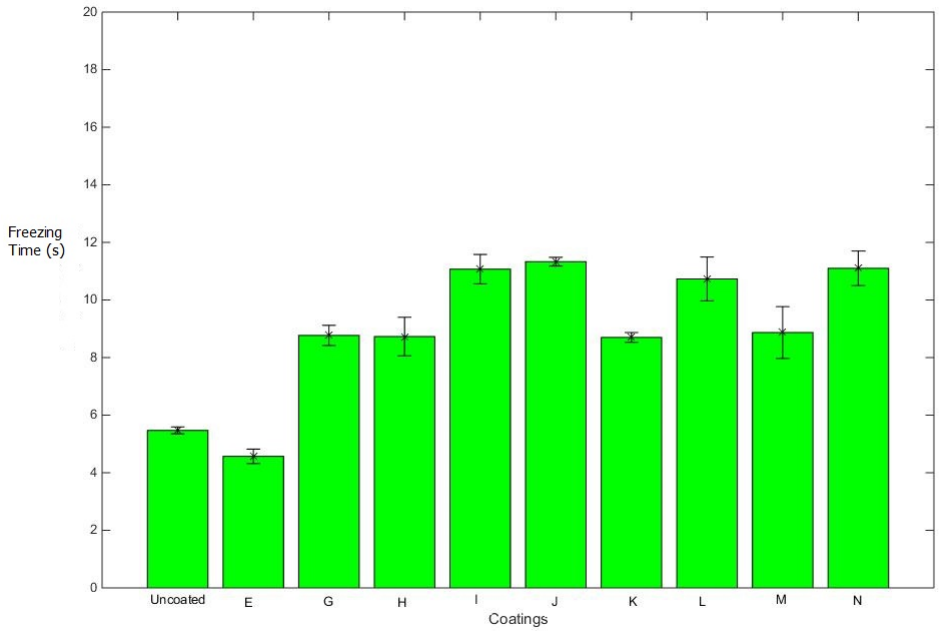


Figure 4.3: Freezing times of droplets at plate temperature of -10°C.

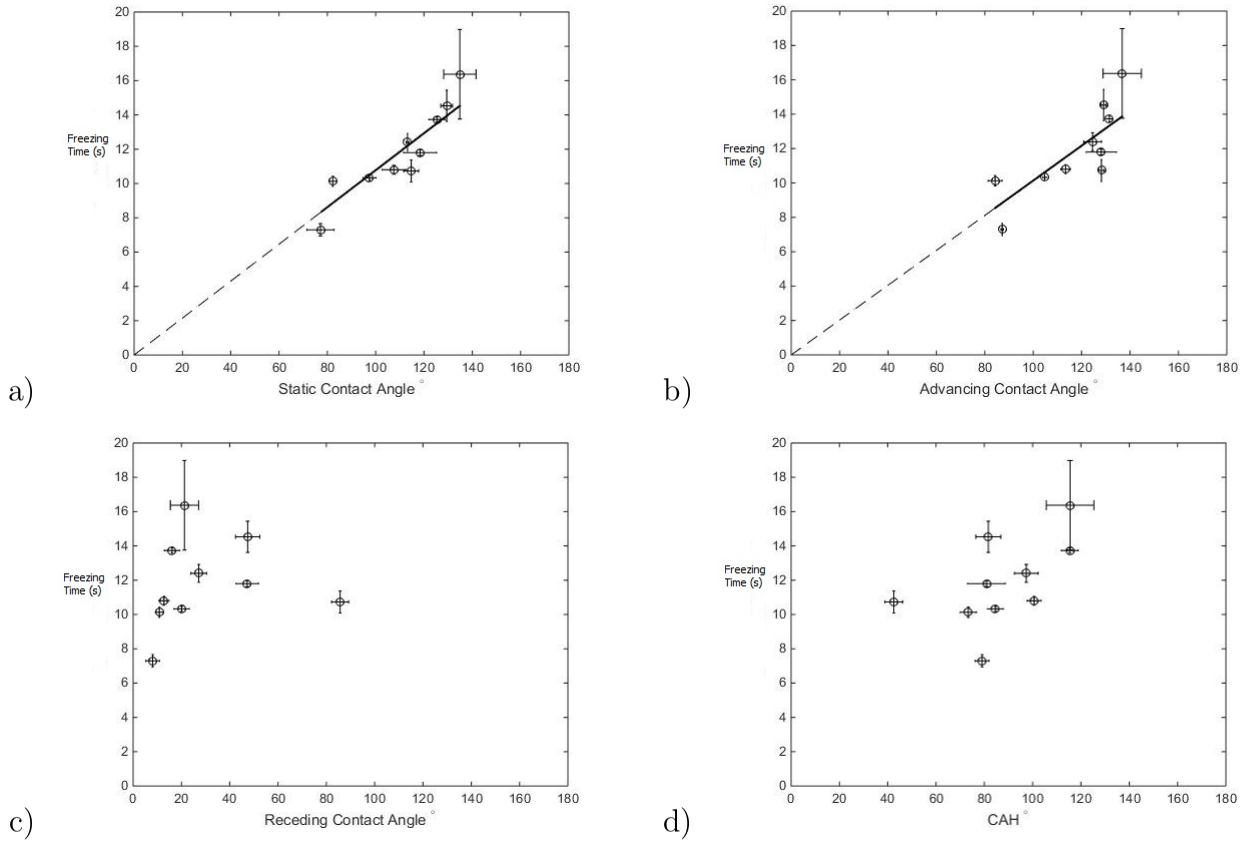


Figure 4.4: Freezing times of droplets at -5°C versus a) Static, b) Advancing, c) Receding and d) CAH.

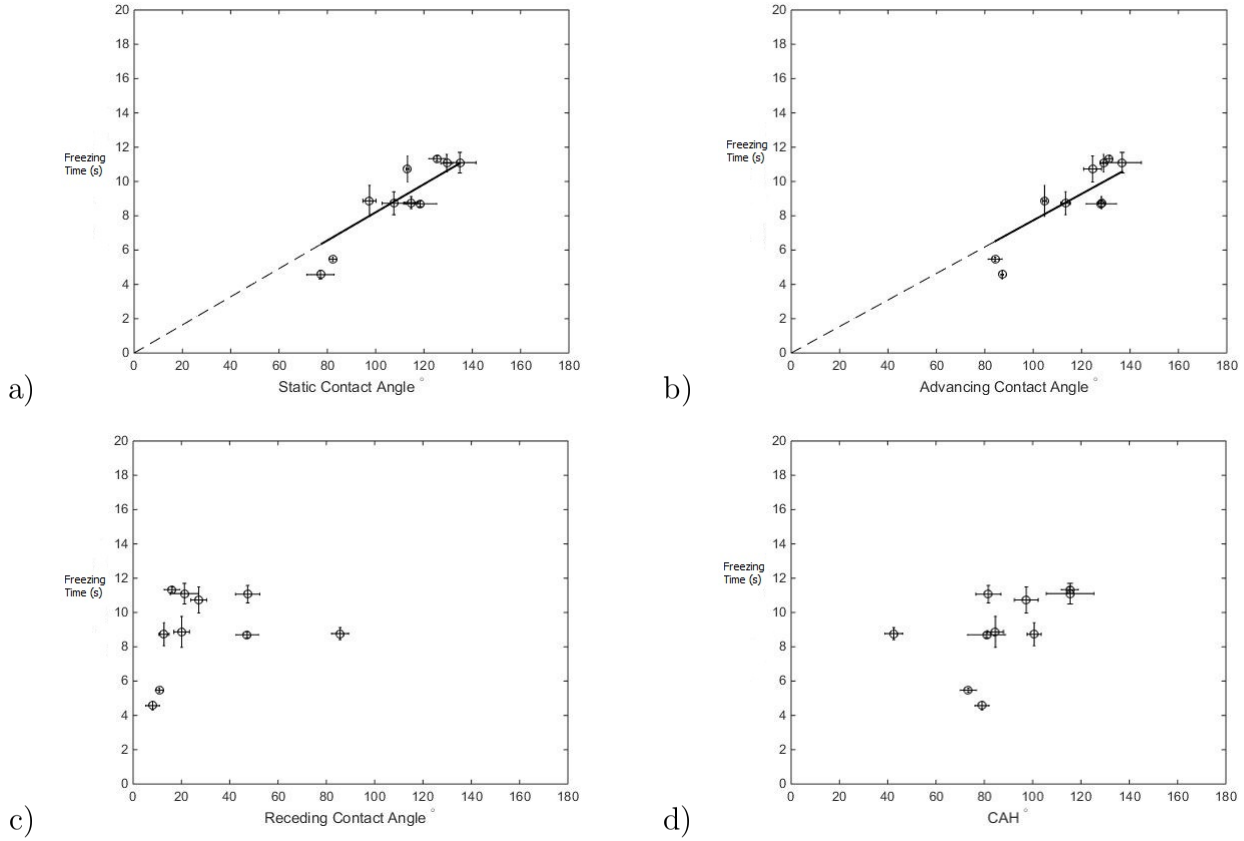


Figure 4.5: Freezing times of droplets at -10°C versus a) Static, b) Advancing, c) Receding and d) CAH.

performed poorly in this assessment had high CAH despite having high static contact angles with high level of consequent ice adhesion.

4.4 Conclusion

A study has been conducted to evaluate the anti-icing ability of nanocoatings through a series of freezing droplet tests. Freezing times at both -5°C and -10°C were most dependent on static contact angle and then advancing contact angle. The reason for this is that static contact angle is a key parameter determining the amount of surface area of a droplet in contact with a coating. Value of the fit in the case of former would have been better with lower condensation on the surface of the coating during test. Anti-icing ability had little or no dependence on receding contact angle or CAH as seen from results. Coatings were ranked using data from the previous chapter, namely wear rate and retained icephobicity, along with freezing times at both test temperatures. The best coatings were found to be N (5% functionalised carbon nanotube content with use of an interlayer and with deposition of final surface promoter layer) and J (10% functionalised carbon nanotube content with use of an interlayer and with no deposition of final surface promoter layer). Apart from contact angle parameters, thicker coatings and thermally

resistive materials may reduce the freezing time. A more systematic and detailed analysis is required to determine the complete influence of these parameters.

High static contact angle, high advancing contact angle, high receding contact angle and low CAH (upto $\sim 92^{\circ}$) are most desirable parameters for an icephobic surface. At CAH values above $\sim 92^{\circ}$ and closer to 180°, adhesion strength begins to reduce as seen in Chapter 3. However in reality, CAH values in this range are rare for modified surfaces. For aerofoils in particular, as the height of the accretion grows with time, the conduction of heat reduces with the wing surface temperature altering dramatically. In this regard, the anti-icing effectiveness of icephobic nanocoatings is extremely relevant at the early stages of accretion.

Chapter 5

A One-dimensional Mixed Ice Accretion Model

5.1 Introduction

This chapter details a one-dimensional ice accretion model encompassing glaze, rime and mixed ice accretion. To solve the full flow field and couple to icing physics would require a commercial computational fluid dynamics (CFD) numerical model and simplified Navier-Stokes equations to model the air flow around the wing. However, the complexity of the flow results in a number of parameters mean that this approach can never be entirely

predictive. Here, we try and consider a simplified model to see if the causal physics can be better understood.

Rime ice models have proved to be accurate in their comparison with experimental data since its formation requires heat transfer only through the droplets which freeze instantaneously on impact with the wing surface. However, the more complex heat transfer processes involved in glaze ice accretion (combining convection and conduction) require more substantial parametrization, which is yet to be verified.

A major problem with many of the current icing models includes discarding the effects of surface tension and viscosity near the stagnation point and using an unverifiable "conduction" parameter to close the system of equations e.g. [47, 46]. Earlier, Poots and Skelton (1992) [84] devised a simple analytical model for ice accretion on a flat surface. The differences in physical properties of rime and glaze along with the influence of airflow on droplet velocities was however neglected. Sherif et al. (1997) [85] determined evaporation and sublimation fractions for glaze ice formation using a semi-empirical model. A simple Messinger heat transfer model [45] was used to relate the incoming and outgoing energy terms. The Messinger model was developed as a one-dimensional energy balance to determine the accretion of rime and glaze on aerofoils that are insulated and unheated [45]. The is-

sues with the model including isothermal water and ice layers, lower freezing fraction values due to instantaneous switching from rime to glaze and insulated substrate can be overcome by using a Stefan condition [86]. The Stefan condition describes the velocity of the moving ice front as dependent on the conduction across it. One of the other outcomes with current icing codes is the over prediction of ice growth during the accretion process [87]. We hypothesise that this over prediction of the ice height is due to the neglect of some key mixed ice physics in the heat and mass transfer balances.

An improvement to the previous commercial icing codes, such as LEWICE, TRAJICE and ONERA, the ICECREMO, has been developed over a number of years to include the effect of the dynamic behaviour of the runback water film on the accretion rate [22, 50, 51, 52]. The Messinger model for the heat transfer process resulted in predicting a significantly lower rate of ice accretion than observed. The ICECREMO code approached the problem by including a Stefan condition which resulted in more accurate comparisons. In further work conducted by Myers et al. (2002) [88], the model was adapted for several geometries and dimensions. Additionally most of the limitations are relaxable factors affecting aerofoil accretion e.g. the thermal mass of the accretion surface must be significantly larger than that of the accretion itself. Brakel et al. (2007) [48] investigated the complexities between the

parallel heating and cooling by the incoming droplets on the thin film and subsequent ice accretion due to their kinetic energy and intrinsic temperature respectively. In a more recent model, Cao et al. (2012) [49] used an Eulerian two-phase approach for the air flow field to numerically solve ice accretions on an aircraft wing. However, limitations of this model does not take into account the runback of a thin film and depends solely on a droplet catchment efficiency calculation to form the liquid component of the system. Inclusion of those aspects form the motivation of our research in this chapter.

A more sophisticated approach to the ICECREMO Code used in Myers and Charpin (2004) [89] will form the basis for our numerical model. Like Myers et al. (2002) [88], it can be applied to various geometries but provides enhancements due to more accurate comparisons with experimental results over the extent of a rivulet zone. The model also incorporates a more detailed description of the formation of a thin rime zone associated with increasing coarsity near the water development in comparison to ice microstructure studies. A noted limiting factor of the icing model exhibited in Myers and Charpin (2004) [89] is the non-inclusion of mixed ice accretion which may influence the heat transfer process.

The ice accretion process is not homogeneous with different types of ice growing under different environmental conditions. Rime ice results

from a relatively simple heat transfer process, whereby, supercooled water droplets freeze instantaneously on impact with sufficiently cold wing surface [45, 46, 47, 48, 49]. This process creates a relatively low density, porous ice, with a distinctive white appearance. In contrast, glaze ice typically grows at temperatures closer to the melting point via a Stefan-type boundary process [86], to form a dense and translucent ice layer. Glaze formation requires the presence of water, either due to partial freezing of the supercooled water droplets, or as *runback* water as generated from electrothermal systems in the leading edge, created from melting any ice structures accreted there. In practice, the ice that forms on an aircraft wing tends to be a combination of rime and glaze ice; potentially with some embedded pockets of air and described as *mixed ice*.

This chapter considers the formation of mixed ice on an aircraft wing from the partial freezing of impinging supercooled droplets, which deposit onto a growing interface formed as a combination of solid rime ice particles and water. We characterise this as a multiphase layer comprising a porous ice medium created by the solid rime ice particles and water; consideration is given at longer accretion times and different atmospheric conditions. This is in contrast to more traditional ′spongy ice′ models that envisage unfrozen water from supercooled droplets entrapped within the growing ice

dendrites [90]. We note mushy layers as seen in sea ice for example, form due to a secondary diffusive process at the solidification front with a presence of multiphase microstructures [91]. Although not explicitly modelled, a multiphase porous medium can provide additional insight towards the inclusion of a mushy structure in future icing models. Generally the water within a rime ice matrix can solidify as additional glaze ice within the pore space. A solidifying glaze ice grows through the rime particles to create a layer of co-existing rime and glaze, i.e. mixed ice. In this work we determine a model for the growth rate and accretion based on prevailing atmospheric conditions. Including the formation and development of a porous ice matrix layer within this model enables more general possibilities to explore in the future, such as forced convective transfer modes.

5.2 Model Assumptions

1. The atmospheric and droplet temperatures are assumed equal as the thermal mass of individual droplets is negligible within the environment. The substrate temperature is also taken as equal to the atmospheric temperature since the wing is generally a very efficient thermal conductor ($T_a = T_d = T_s$).

2. Physical properties of ice and water do not vary with respect to time or

temperature. Rime and glaze ice are assumed to have distinct densities ρ_r and ρ_g respectively.

3. The phase change for both rime and glaze ice in the model is taken to occur at a simple temperature T_f.

4. The water film is well-mixed and isothermal at T_f.

5. The solid ice fraction ϕ is constant for a given density of rime ice and for all stages of accretion.

6. The porous spaces in the rime ice structure are interstitial in nature and not in the form of air bubbles encapsulated in ice. This is plausible in reality for different types of rime ice such as feathery, kernel and opaque having densities ranging from $100\,\mathrm{kg\,m^{-3}}$–$900\,\mathrm{kg\,m^{-3}}$ respectively [92].

5.3 Model Formulation

In the following we introduce four, potentially consecutive, modes of ice accretion. In terms of their application to an aircraft wing, we consider the aircraft passing through cloud cover, where the local temperatures can be very cold and where water droplets are supercooled. As the aircraft travels, water droplets impinge on the wing surface. For the moment, we restrict our interest to one-dimensional accretion where the time evolution of ice growth

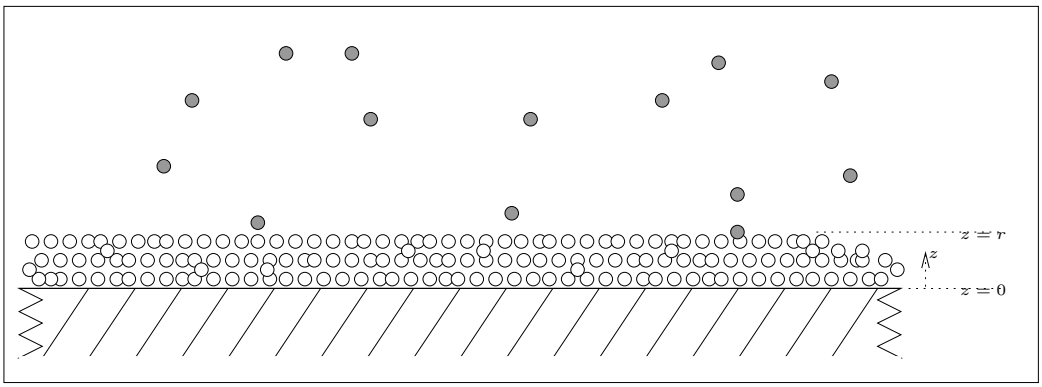


Figure 5.1: Schematic representation of the modes of accretion in mixed ice formation. At times $t < t_w$, supercooled droplets freeze on impact with the wing, forming rime ice (with air in the pore space).

is normal to the wing surface; we assume that the ambient conditions and influx of droplets are steady. In this way we aim to understand the influence of rime versus glaze versus mixed accretion modes on the resulting accretion profiles.

5.3.1 Mass Flux of Droplets

Figure 5.1 exhibits the supercooled droplet mass flux prior to the accretion stage. The first step for the icing code is to define the contributing terms in the mass balance. The rate of impinging droplets incident on an aircraft

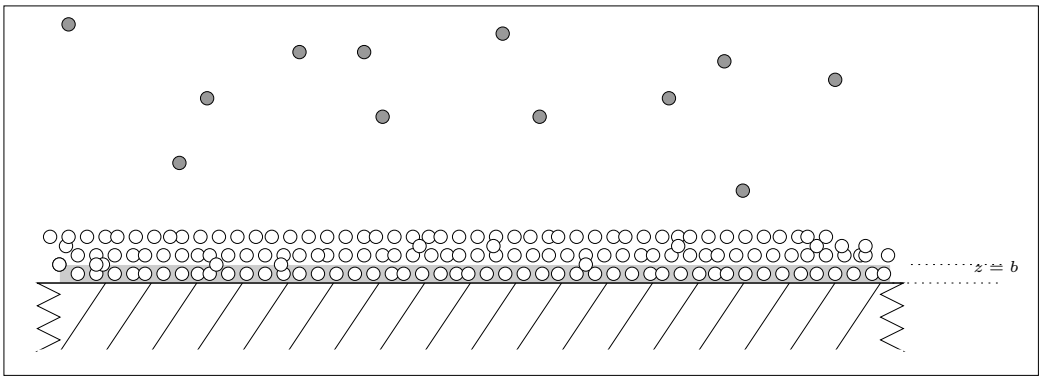


Figure 5.2: Schematic representation of the modes of accretion in mixed ice formation. When the layer of rime ice is thick enough that the latent heat released on freezing can no longer be conducted through it, a proportion of the incoming supercooled droplets remain as water. This percolated water quickly freezes as glaze ice within the pore spaces of the original rime layer ($t_w \geq t < t_b$).

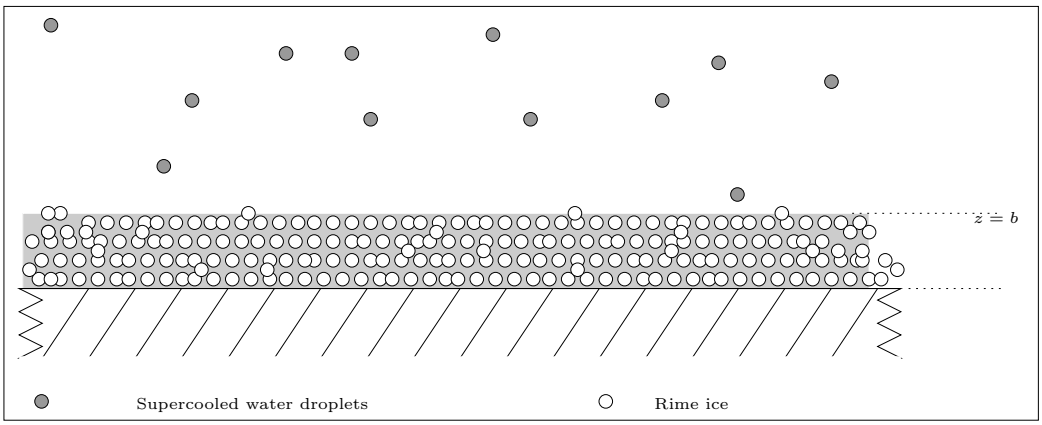


Figure 5.3: Schematic representation of the modes of accretion in mixed ice formation. Once the glaze ice fully occupies the pore space between the rime crystals, rime and glaze can accrete simultaneously in a mixed ice layer, enhancing the thermal conductivity over rime ice alone.

wing $\dot{N}$ can be expressed as

$$\dot{N} = \frac{V_{air}\rho_a\beta}{V_d\rho_w}, \tag{5.1}$$

where $V_d = \frac{\pi d^3}{6}$ is the volume of a single (spherical) droplet and V_{air} is the volume of air incident on the aircraft wing per second. V_{air} is given by

$$V_{air} = AU_\infty cos\alpha, \tag{5.2}$$

where α is the angle of attack. Beyond $\alpha = 20°$, the aircraft is likely to stall; hence α generally ranges in flight between 5° and 15°. The incoming mass flux of supercooled droplets incident per unit area of the wing $\dot{M}$ can

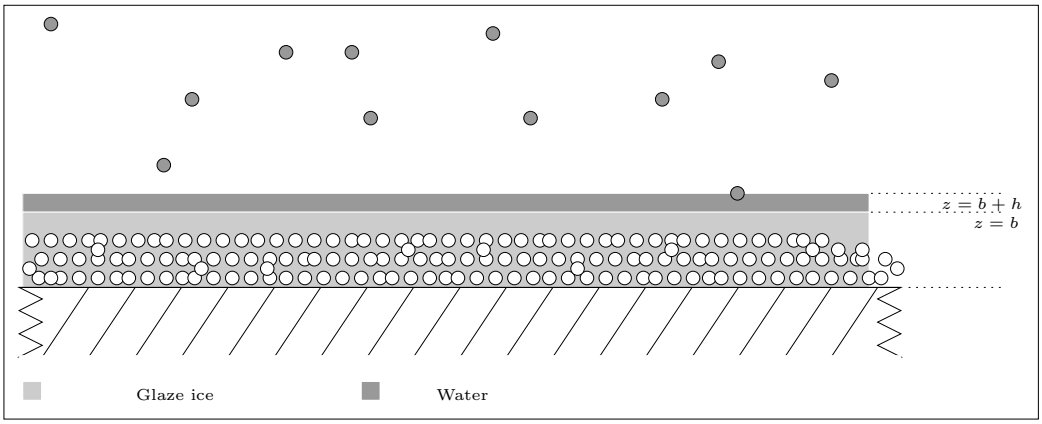


Figure 5.4: Schematic representation of the modes of accretion in mixed ice formation. The *mixed ice* layer restricts the transport of released latent heat and a water film forms on its surface. This leads to the formation of glaze ice. This may be supplemented by runback water formed by melting ice formations at the wing leading edge.

be defined as

$$\dot{M} = \frac{V_d \dot{N} \rho_w}{A}, \tag{5.3}$$

which corresponds to

$$\dot{M} = \beta U_\infty \rho_a cos\alpha. \tag{5.4}$$

For one-dimensional accretion on a flat plate, $\alpha = 0$ and taking $\beta = 0.5$, ρ_a $= 0.001\,\mathrm{kg\,m^{-3}}$ and $U_\infty = 90\,\mathrm{m\,s^{-1}}$; we get $\dot{M} = 0.045\,\mathrm{kg\,m^{-2}s^{-1}}$.

5.3.2 Rime Ice

In the earliest stage of accretion, taking the wing as approximately at the temperature of the ambient air, the supercooled droplets that the wing collects will freeze on impact to form rime ice [22], is shown in Figure 5.1. The wing is an excellent thermal conductor, so the latent heat associated with the supercooled droplets is easily transported.

A key feature of rime is that air is trapped within the pore space, between tiny crystals of ice. Thus we define a solid volume fraction of ice in this rime layer

$$\phi = \frac{\rho_r}{\rho_i}, \tag{5.5}$$

where ρ_r is the bulk density of the rime ice layer and ρ_i is the density of pure ice. Throughout this work we assume that all ice, rime particles or glaze, has

density ρ_i, which is independent of temperature. For typical values of opaque rime bulk density, $\rho_r \geq 610\,\mathrm{kg\,m^{-3}}$ [93], the equivalent solid volume fraction gives, $\phi \geq 0.67$; this corresponds roughly to the maximum packing fraction of spheres [94]. Further work regarding the microstructure of ice, especially considering asperities of rime being wetted, was conducted by Hobbs (1990) [95]. This is an important step towards describing mixed ice formation.

For simplicity, we consider one-dimensional accretion, varying with time only, on a flat plate. The rate of growth of the rime front at $z = r$ (Figure 5.1) is given by a mass balance

$$\frac{\partial r}{\partial t} = \frac{1}{\rho_i \phi} \dot{M}, \tag{5.6}$$

where $\dot{M}$ is the mass flux of incident water droplets. For constant values of $\dot{M}$ and ϕ and initial values $r(t = 0) = 0$, the ice height follows,

$$r = \frac{\dot{M} t}{\rho_i \phi}. \tag{5.7}$$

5.3.3 Mixed Ice

Rime ice will continue to accrete as in Equation 5.7 until the layer becomes so thick that the latent heat released on solidification of the droplets can no longer be conducted away through the wing, and the top surface of the rime is at the freezing temperature T_f [89]. This transition time, t_w, can be

evaluated from an energy balance. At this point, water forms alongside the rime ice and the ice becomes "*mixed*". This water may percolate through the pore space. Since the rime layer is thin and below the freezing temperature beneath its surface, it may freeze as glaze ice inside the pore space. In this Section, we assume that the water freezes from the wing surface upwards and that no air remains trapped in the pore space. The typical air content of mixed ice based on density valuations provided for the transition between soft and hard rime is approximately 0.65 [96].

Effectively, only a proportion λ of the incoming supercooled droplets freeze. This frozen portion continues to grow as a rime layer at the air-rime interface, with the liquid portion freezing as glaze ice in the rime pore space. This glaze freezing process inside the pore space occurs over a very short timescale, so we do not explicitly model the processes. We assume that the fraction of the supercooled droplets that remains as water accretes directly as glaze ice within the rime layer (Figure 5.2). At longer accretion times (Figure 5.4), a water film may grow above the air-rime interface. In such a situation, the supercooled droplets will impact a water film directly instead of the rime matrix and both rime and glaze will accrete simultaneously. Essentially, we have rime ice accretion initially followed by the freezing of percolating water between the interstices of ice to give primary mixed. In

the next stage, the unfrozen water from the supercooled droplets freezes at the interface itself before the existence of a thin film where water droplets impact directly. This is the final stage of glaze ice formation.

Thus, the freezing fraction λ is a dimensionless quantity defined as the fraction of a supercooled droplet that solidifies on impact with the aircraft wing, the rime matrix and the water film during different stages of accretion. We assume that the droplet impact leads to immediate rest in the three different scenarios mentioned. The parameter value λ is dependent on the individual droplet characteristics such as size, velocity and temperature as well as the temperature of the surface that it impacts. This contrasts with previous definitions of the freezing fraction F, as the ratio of the amount of ice formed to the mass flux incoming supercooled droplets, which does not affect the rate of accretion but is rather a by-product of the freezing process. Correspondingly, F is calculated after and not before the solidification process occurs for glaze ice. λ in contrast determines both the rate and type of ice formation which will be apparent in our subsequent discussion. For pure rime accretion, $\lambda = 1$.

5.3.4 Energy Balance

While the water and ice (both glaze and rime) layers remain thin, we can assume that conduction across the layers is the primary mode of heat transfer. Convective heat transfer will begin to dominate when the water film height is greater than 3 mm [5]. The reduced pseudo-steady state conduction equations for heat transfer through the ice and water layers are

$$\frac{\partial^2 T}{\partial z^2} = 0, \tag{5.8}$$

and

$$\frac{\partial^2 \theta}{\partial z^2} = 0, \tag{5.9}$$

where T and θ are the temperatures in the ice and water layers respectively [5]. Considering first the early stage of rime accretion (Figure 5.1), the temperature distribution through the rime layer is specified by taking the rime temperature as the wing surface temperature, as determined by $T(z = 0) = T_a$. Further, the heat flux through the air-rime interface is determined by an energy balance there [5, 89],

$$\left.\frac{\partial T}{\partial z}\right|_{z=r} = \frac{1}{k_i}\left[Q_l + Q_k + Q_a - (Q_r + Q_h + Q_s)\right], \tag{5.10}$$

where

$Q_k = \frac{1}{2}\dot{M}U_\infty^2$ is the droplet kinetic energy,

$Q_a = \frac{1}{2c_a}aH_{aw}U_\infty^2$ is the aerodynamic heating,

$Q_l = \lambda\dot{M}L_f$ is the release of latent heat,

$Q_d = c_w(1-\lambda)\dot{M}(T-T_d)$ is the droplet thermal energy after stage one of rime accretion,

$= q_d(1-\lambda)(T-T_a)$

$Q_r = c_w\lambda\dot{M}(T-T_d)$ is the droplet thermal energy during stage one of rime accretion,

$= q_r\lambda(T-T_a)$

$Q_h = H_{aw}(T-T_a)$ is the convective heat transfer from rime to air,

$= q_h(T-T_a)$

$Q_s = x_s e_0(T-T_a)$ is the heat of sublimation,

$= q_s(\theta-T_a)$

$Q_i = c_w\lambda\dot{M}(T_f-T_d)$ is the energy to raise the temperature of solidifying fraction of the droplet to the freezing point after stage one of rime accretion.

$= \lambda q_d(T_f-T_a).$

Myers (2001) [5] and Myers & Charpin (2004) [89] show that Equation 5.10 can be simplified in the form

$$\frac{\partial T}{\partial z} = E_{rz} - F_{rz}T, \tag{5.11}$$

where

$$E_{rz} = \frac{1}{k_i}\left\{Q_k + Q_a + Q_l + q_r T_d + (q_h + q_s)T_a\right\}, \tag{5.12}$$

and

$$F_{rz} = \frac{1}{k_i}\left(q_r + q_h + q_s\right). \tag{5.13}$$

Solving Equation 5.8 for T subject to the fixed temperature at the wing surface and flux determined by the Equation 5.11, gives

$$T = T_a + \frac{E_{rz} - F_{rz}T_a}{1 + F_{rz}r}z, \tag{5.14}$$

within the pure rime layer at $0 \leq z \leq r$.

After this period of rime accretion, water will first appear when the air-rime interface reaches the freezing temperature, that is $T(z = r_w) = T_f$ [89]. Thus

$$r_w = k_i \frac{T_f - T_a}{Q_l - Q_r + Q_a + Q_k - (q_h + q_s)(T_f + T_s)}, \tag{5.15}$$

with a corresponding transition time, given from Equation 5.7 by,

$$t_w = \frac{\phi \rho_i r_w}{\dot{M}}. \tag{5.16}$$

At times $t > t_w$, some of the supercooled water droplets remain as water and $0 \geq \lambda < 1$. This is the regime for the mixed ice accretion described in Figure 5.2. However, under a range of ambient conditions, water could form within the rime layer before this transition time. The atmospheric conditions required for complete, partial or no freezing of the supercooled droplets and the resulting ice type that forms, is described and summarised in Table 5.1.

We assume, that glaze ice freezes quickly within the pore space of previously deposited rime ice and the propagation of the glaze ice through the rime is determined only by a mass balance (see Figure 5.2). Under steady conditions, glaze ice (b_b) will thus reach the top surface of the accretion at a time

$$t_b = t_w + \frac{(1-\phi)\,\rho_i b_b}{(1-\lambda)\,\dot{M}}, \tag{5.17}$$

where at this time

$$r_b = r_w + \frac{\lambda \dot{M}\,(t_b - t_w)}{\rho_i \phi}. \tag{5.18}$$

There are three unknowns in second stage of accretion: r_b, b_b and λ but only two equations so far (Equation 5.17 and 5.18). To solve for λ, we modify the surface conditions at the air-rime interface (Equations 5.12 and 5.13) to give:

$$E_{rm} = \frac{1}{k_i}\left\{Q_k + Q_a + Q_l - Q_i + q_d T_d + (q_h + q_s)T_a\right\}, \tag{5.19}$$

and

$$F_{rm} = \frac{1}{k_i}[q_d + q_h + q_s]. \tag{5.20}$$

We now modify Equation 5.11 using equation 5.19 and 5.20 to give

$$\frac{\partial T}{\partial z} = E_{rm} - F_{rm}T. \tag{5.21}$$

The temperature at the interface is given by solving Equation 5.8 with a fixed temperature at the wing and Equation 5.21 to give

$$T = T_a + \frac{E_{rm} - F_{rm}T_a}{1 + F_{rm}r}z. \tag{5.22}$$

Substituting $T = T_f$ and $z = r$ in equation 5.22, we obtain an equation for λ to solve along with Equations 5.17 and 5.18 during the second stage of accretion.

Once the glaze ice front reaches the top of the rime (Figure 5.3) mixed ice will continue to grow. Rime and glaze ice form alongside each other in the form of secondary mixed ice arising from conduction through the glaze ice freezing unfrozen water at the air-rime interface. As the rate of conduction reduces with the increase in ice height, eventually, a water film begins to appear within the interstitial rime matrix above the growing glaze.

This can rapidly lead to the film occupying the porous spaces and flowing above the rime matrix, as well when the packing fraction is high and freezing fraction is low.

Any water layer formed over the ice surface interacts with the air flow over the wing. With a water film present (Figure 5.4), the boundary condition fixing the ice temperature at the wing surface to the ambient air temperature, $T(z = 0) = T_a$, remains the same. At the growing ice front, $z = b$, the temperature in both the ice and water phases is the freezing temperature, $T(z = b) = \theta(z = b) = T_f$. Integrating equation 5.8 subject to these boundary conditions, the temperature in the ice layer is given by

$$T = \left(\frac{T_f - T_s}{b} \right) z + T_s, \tag{5.23}$$

for $0 \leq z \leq b$.

Any water film on top of this glaze ice will be at the freezing temperature at the ice front and at its upper surface, $z = b + w$, the heat flux is determined by an energy balance

$$\left. \frac{\partial \theta}{\partial z} \right|_{z=b+h} = \frac{1}{k_w} \left[Q_l + Q_k + Q_a - (Q_i + Q_d + Q_h + Q_e) \right], \tag{5.24}$$

where $Q_e = x_e e_0 (\theta - T_a) = q_e (\theta - T_a)$ is the heat of evaporation. The notable difference between this heat flux boundary condition and that for the rime growth at $z = r$ (equation 5.19), is that evaporation replaces sublima-

tion due to the water film replacing ice at the exposed surface. As earlier, equation 5.24 can be simplified to give

$$\frac{\partial \theta}{\partial z} = E_{gz} - F_{gz}\theta, \tag{5.25}$$

where

$$E_{gz} = \frac{1}{k_w}\left\{Q_k + Q_a + Q_l - Q_i + q_d T_d + (q_h + q_s)T_a\right\}, \tag{5.26}$$

and

$$F_{gz} = \frac{1}{k_w}\left(q_d + q_h + q_e\right). \tag{5.27}$$

Assuming conduction is the leading heat transfer mechanism (equation 5.9), these boundary conditions determine the temperature in the water layer as

$$\theta = T_f + \frac{E_{gz} - F_{gz}T_f}{1 + F_{gz}h}\left(z - b\right), \tag{5.28}$$

for $b \leq z \leq b + w$.

5.3.5 Freezing Fraction

Ultimately, the freezing fraction λ determines the type of ice accretion, but itself is determined by the prevailing physical restraint conditions. For example, the water temperature equation 5.28, is physically constrained. If a

water film exists, then both $h > 0$ and $\theta \geq T_f$, implying that $F_{gz}T_f \leq E_{gz}$. From their definitions in equation 5.28

$$T_f - T_a \leq \frac{Q_k + Q_a + Q_l}{q_d + q_h + q_e}. \tag{5.29}$$

Since Q_l and q_d are dependent on λ, we thus have a corresponding ambient constraint on the value λ can take given typical ambient conditions for icing on an aircraft wing, Table 5.1 [89]. At very cold temperatures, pure rime will form until a water layer would be thermodynamically possible. Thus a value $\lambda = 1$ is possible if $T_a \leq -15.3°\text{C}$. At temperatures greater than this, some glaze ice will be present and the overall accretion will be mixed in appearance. Conversely, pure glaze ice corresponding to $\lambda = 0$ will form if $-1.77° \leq T_a \leq 0.0°\text{C}$; $-1.77°\text{C}$ is thus the highest ambient temperature at which mixed ice can form. These constraints are summarised in Table 5.1.

Myers & Charpin (2004) [89], Myers (2001) [5] and Myers & Hammond [51] cite the highest ambient temperature for pure rime accretion as $-16.6°\text{C}$, $-18.35°\text{C}$ and $-15.98°\text{C}$ respectively, fitting with our analysis. The three values listed are from modelling estimations. Lynch & Khodadoust (2001) [97] cite the temperature for pure glaze accretion as $-3° < T < 0°\text{C}$ where Mirzaei et al (2009) [98] suggest temperatures close to $0°\text{C}$, also fitting with our analysis. The values for glaze ice are based on readings obtained from actual observations of in-flight icing.

Given estimates for the approximate ranges for mixed ice accretion, we can analyse the composition of mixed ice at ambient temperatures in the range $-15.3^\circ < T_a < -1.77^\circ$C, if and when it grows above r_w, the originally deposited rime layer. Taking the water film as isothermal at T_f and existing [5], the proportion of the incoming droplets that will freeze

$$\lambda_m = \frac{(T_f - T_a)(q_d + q_h + q_e) - Q_k - Q_a}{Q_l}. \tag{5.30}$$

Thus, for the typical environmental conditions in Table 5.1, Equation 5.30 predicts that mixed ice accreting at $-5^\circ, -10^\circ$ and -15°C has corresponding values $\lambda_m = 0.24, 0.61$ and 0.98 respectively.

The physical implications of this are open to debate, but adhesion tests indicate that rime ice and mixed ice or glaze ice have very different properties and would require different approaches to anti- or de-icing. The nature of the bond between the ice and the wing surface, in particular the proportion of glaze ice present to increase the strength of that bond, could be a significant consideration in optimising strategies. In most cases, icing encounters below -20°C are extremely rare [10], the temperature range we consider applying to the overwhelming majority of commercial aircraft applications.

Table 5.1: Ice type variation with droplet freezing fraction, λ.

Droplet Freezing Fraction	Type of Ice	Ambient Temperature Range (°C)
$\lambda = 1$	Ice Crystals	$T_a \leq -40.0$
$\lambda = 1$	Rime	$-40.0 \leq T_a \leq -15.3$
$0 \leq \lambda \leq 1$	Rime, Mixed and Glaze	$-15.3 \leq T_a \leq -1.77$
$\lambda = 0$	Glaze	$-1.77 \leq T_a \leq 0.0$
$\lambda = 0$	No Freezing	$0.0 \leq T_a$

5.3.6 Secondary Mixed Ice

To differentiate from the mixed ice that grows through the early-deposited rime layer, we will use the term '*secondary mixed*' to describe the mixed ice that accretes after a time t_b due to partially freezing supercooled droplets. This consists of the simultaneous deposition of a matrix of rime ice, with water freezing in the pore space as glaze ice.

The growth rate of the rime matrix follows Equation 5.18 at times

$t > t_b$, with $\lambda = \lambda_m$. Thus the accretion becomes

$$r = \frac{\lambda_m \dot{M}\,(t - t_b)}{\rho_i \phi} + r_b. \tag{5.31}$$

The next step is to determine the actual level of the unfrozen portion of the supercooled droplets that impact the air-rime interface before incorporating conduction via the Stefan equation. We note, either the unfrozen portion will occupy a space within the rime matrix or will fill this space up and engulf the rime matrix. The limit of the unfrozen supercooled droplets is given by

$$w = \frac{(1 - \lambda_m)\dot{M}\,(t - t_b)}{\rho_w (1 - \phi)} + r_b. \tag{5.32}$$

If $w \geq r$, then $l = r + h_w$ where

$$h_w = (1 - \phi)(w - r). \tag{5.33}$$

The glaze ice growth rate is determined by a Stefan condition [99] matching the rate of release of latent heat as the liquid solidifies to the rate at which that heat can be transported from the glaze solidification front. After fixing the limit of w, we incorporate a single time step of glaze ice growth b due to Stefan conduction and given by

$$(1 - \phi)\rho_i L_f \frac{\partial b}{\partial t} = k_i \frac{\partial T}{\partial z}, \tag{5.34}$$

providing w is within r. Integrating Equation 5.34 (please see Equation 6.6 for complete derivation) with conditions $b = r_b$ at $t = t_b$ gives the rate of propagation of this 'glaze front' here b_m as

$$b_m = r_b + \sqrt{\frac{2k_i(T_f - T_s)(t - t_b)}{(1-\phi)\rho_i L_f}}. \tag{5.35}$$

If w is outside r, b is given by

$$\rho_i L_f \frac{\partial b}{\partial t} = k_i \frac{\partial T}{\partial z}; \tag{5.36}$$

the term on the right hand side corresponds to the transport of heat through the already-formed ice behind the front. The above ignores conduction through the water film since it is typically small since the water film is approximately isothermal [5]. Similar to equation 5.35, equation 5.36 now becomes

$$b_m = r_b + \sqrt{\frac{2k_i(T_f - T_s)(t - t_b)}{\rho_i L_f}}. \tag{5.37}$$

The water film appears when the limit of b_m is less than w and implies that there is now some unfrozen water in the rime matrix or above it. In this case, glaze development underneath and the amount of heat conducted away through the ice to the wing is insufficient to freeze all of the unfrozen supercooled droplet fraction. When w is less than b_m, we do not differentiate between the rime and glaze fronts since the process is such that everything freezes almost instantaneously. The mass balance for glaze ice accretion

(Stage 4 of ice accretion) when the glaze ice and water remain within the rime matrix is given by

$$\dot{M} = (1-\phi)\rho_i \frac{\partial b}{\partial t} + (1-\phi)\rho_w \frac{\partial w}{\partial t} + \phi\rho_i \frac{\partial r}{\partial t}. \tag{5.38}$$

A further possibility is the presence of the unfrozen water completely saturating the rime matrix and existing above it. In this case, if the glaze ice limit remains within the rime matrix, the mass balance is given by:

$$\dot{M} = (1-\phi)\rho_i \frac{\partial b}{\partial t} + (1-\phi)\rho_w \frac{\partial w}{\partial t} + \rho_w \frac{\partial h}{\partial t} + \phi\rho_i \frac{\partial r}{\partial t}. \tag{5.39}$$

where h is the height of the water film above the rime matrix. Subsequently, if the glaze limit grows above the rime matrix, with the presence of unfrozen water above it, the mass balance becomes:

$$\dot{M} = (1-\phi)\rho_i \frac{\partial b}{\partial t} + \rho_i \frac{\partial g}{\partial t} + \rho_w \frac{\partial h}{\partial t} + \phi\rho_i \frac{\partial r}{\partial t}. \tag{5.40}$$

where g is the height of glaze ice above the rime matrix.

5.3.7 Accretion Types

The atmospheric conditions listed in Table 5.1 represent three possible accretion regimes. At cold atmospheric temperatures, $T_a \leq -15.29°\text{C}$, only rime ice can form. Thus, accretion follows Equation 5.7 under steady conditions.

Conversely, if the atmospheric temperature is close to the freezing point, $-1.77^\circ \leq T_a \leq 0^\circ$C, incoming droplets deposit as water which then forms glaze ice. The mass balance described in equation 5.38, where the solid volume fraction $\phi \approx 0$, describes the total ice and water layer with the Stefan solidification condition Equation 5.34, determining the extent of the glaze ice within this. This model is used in most current major icing codes, such as glaze ice model [5] and includes conduction through the water film which is not included in our model.

In intermediate conditions, $-15.29^\circ \leq T_a \leq -1.77^\circ$C, mixed ice forms, described by the model developed. Thus initially, for $t \leq t_w$, rime ice forms following Equation 5.7 until $r = r_w$. At this point, λ decreases as glaze ice forms in the previously deposited rime pore space, until $t = t_b$ and the (primary) mixed ice thickness $b = b_b = r_b$ (equation. 5.17 and 5.18). Glaze and rime continue to grow together as secondary mixed ice, with freezing fraction λ_m. Rime and glaze ice heights are described by Equations 5.31, 5.35 & 5.37 respectively where applicable.

5.4 Solution Procedure

Based on Table 5.1 and Figure 5.1, it is useful to indicate the relevant equations applicable to different temperature limits.

1. Ice Crystals – $T_a \leq$ -40°C

This accretion type is out of the scope of this research and not as harmful as supercooled droplet icing.

2. Rime Ice – -40°C$\leq T_a \leq$-15.29°C

Within these atmospheric temperature limits, equation 5.6 is valid. All of the supercooled droplets freeze on impact.

3. Rime, Mixed and Glaze Ice – -15.29°C$\leq T_a \leq$-1.77°C

Equations explained in rime, primary mixed, secondary mixed and glaze are applicable within these temperature limits.

4. Glaze Ice – -1.77°C$\leq T_a \leq$0°C

Myers and Charpin (2004) [89] describe ice accretion in this range accurately.

5.5 Results and Analysis

It has been reported that just 0.13 mm and 0.77 mm of ice accretion can reduce lift characteristics of an aircraft in flight by 20% and 40% respectively

[100]. Several devices do currently exist to detect ice near the leading edge of the wing to aid in the visual capacity of crew members including cylinders, sensors using stiffness, hot rods etc. Modern optical sensors provide a consistent signal at 1.27 mm of ice thickness [101]; while ultrasonic sensors under development in a high frequency mode of 2 MHz are sensitive to even 0.2 mm of ice accretion [102]. Correspondingly a key comparative portion of this analysis focuses on what we term as the "rapid accretion" phase of 30 seconds when the aircraft is descending or ascending through a cloud structure containing supercooled droplets. After this time period, the aerodynamic characteristics are negatively affected and the ice detection and protection systems begin functioning to mitigate the problem.

In the next section, the variation in accretion profile of such mixed ice with variation in ambient conditions is considered. We describe A) the initial rime accretion phase at $0 \leq t \leq t_w$, B) a primary mixed accretion phase at $t_w \leq t \leq t_b$, C) a secondary mixed accretion phase at $t_b \leq t \leq t_m$ and finally D) a glaze accretion process when $t \geq t_m$.

Figure 5.5 exhibits ice accretion at ambient temperature of -5°C and $\phi = 0.65$. Using an accretion time of 100 seconds shows a clear transition between the various stages such as the rime stage (0–9 secs), primary mixed stage (9–34 secs), secondary mixed stage (34-67 secs) and glaze stage (67–100

secs). Figure 5.6 exhibits the change in freezing fraction λ with respect to time for conditions associated with Figure 5.5. We note λ is independent of ϕ during the rime ice stage and remains constant λ=1. The value of λ then continues to steadily decrease during a primary mixed stage because as the rime ice height increases. In this stage, the ability to conduct latent heat away from the air-rime interface decreases and the fraction of unfrozen supercooled droplets continuously decreases. Any decrease will be more dramatic with higher values of ϕ as the porous space will fill more quickly from unfrozen supercooled droplets. For the secondary mixed and glaze stages, our model assumptions lead to a constant value of λ; the value of λ is dependent only on the atmospheric temperature since the air-ice or air-water interface is fixed at the freezing temperature T_f. Figure 5.7 describes the temperature profile during the different stages of accretion for conditions described in figure 5.5. We can observe that the transition from rime to primary mixed occurs when the temperature of the air-rime interface reaches T_f. This is in congruence with the glaze ice model [5]. The temperature profile through the glaze growing from the wing upwards during primary mixed follows a linear profile dependent on the location of the top interface. A linear temperature profile is also apparent during the secondary mixed and glaze stages with water film assumed isothermal at T_f.

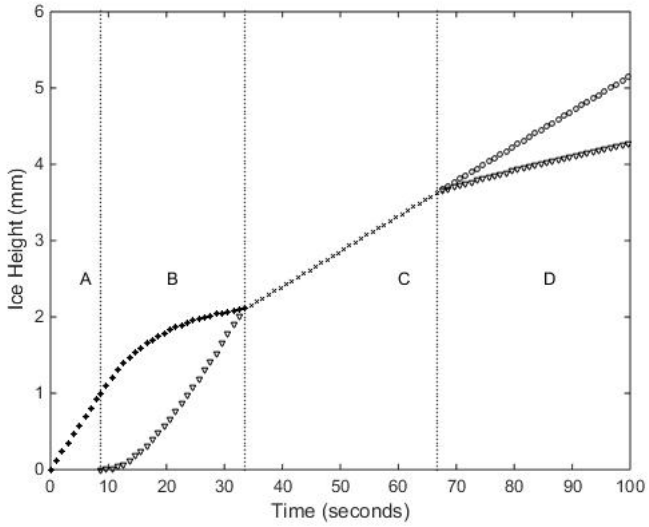


Figure 5.5: Mixed ice accretion model at T_a = -5°C and $\phi = 0.65$.

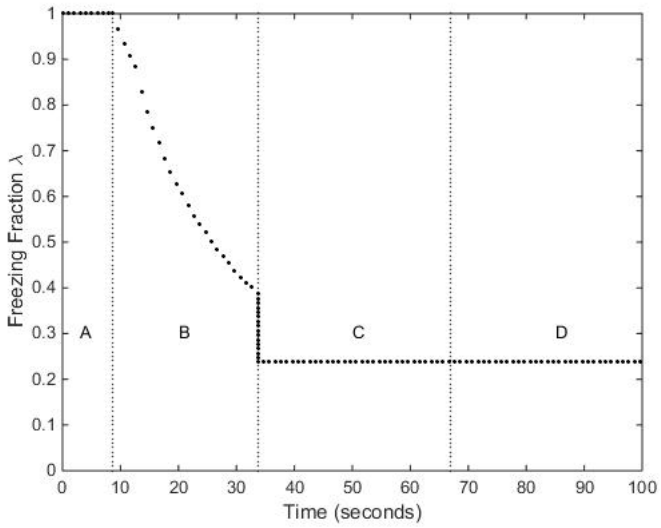


Figure 5.6: Freezing fraction versus accretion time at T_a = -5°C and $\phi = 0.65$.

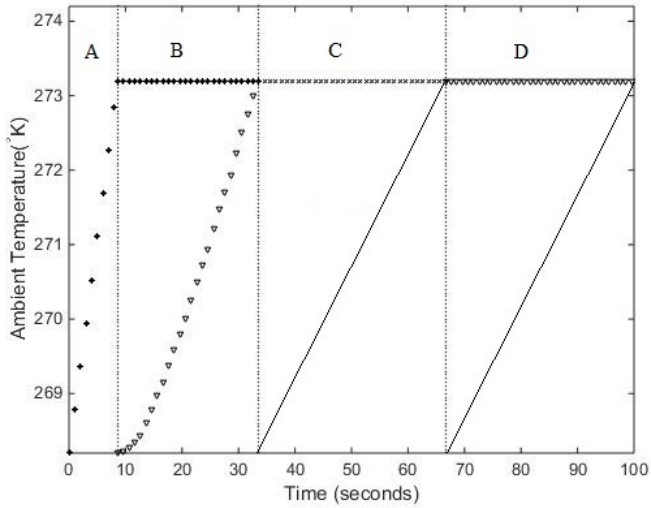


Figure 5.7: Temperature profile of mixed ice accretion model at T_a = -5°C and $\phi = 0.65$.

5.5.1 Variation of Ice Height and Freezing Fraction λ with Rime Ice Density and Ambient Temperature

Figures 5.8–5.11 illustrate ice growth under several conditions of ambient temperature and packing fraction with accretion time of 30 seconds. Values corresponding to the different ice and water limits are represented by the following symbols: rime (♦), glaze ($\bigtriangledown$), mixed (x) and water film (+).

We can determine the influence of the two key parameters: packing

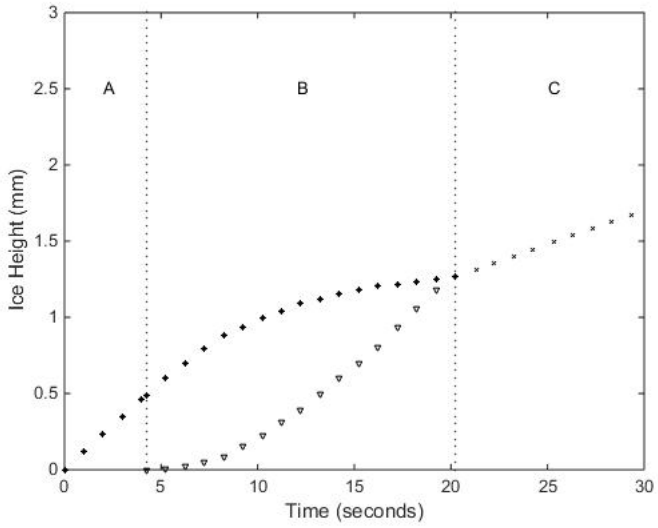


Figure 5.8: Mixed ice accretion model at T_a = -3°C and $\phi = 0.65$.

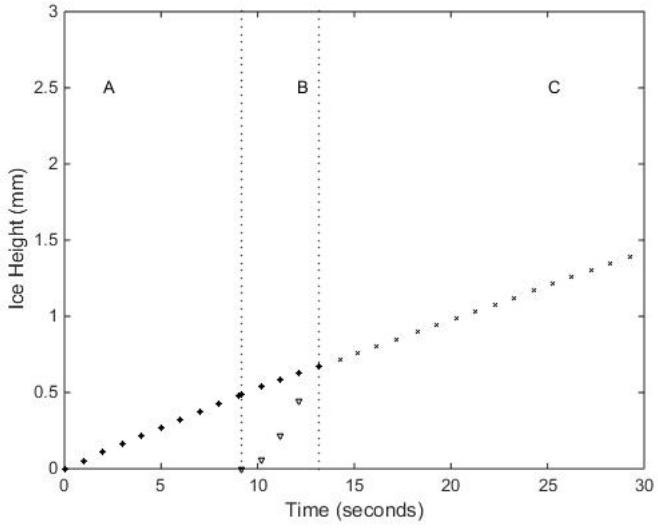


Figure 5.9: Mixed ice accretion model at T_a = -3°C and $\phi = 0.96$.

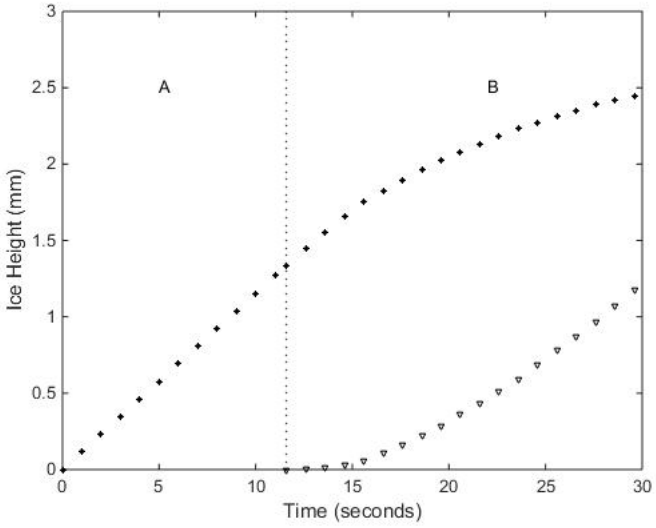


Figure 5.10: Mixed ice accretion model at T_a = -6°C and $\phi = 0.65$.

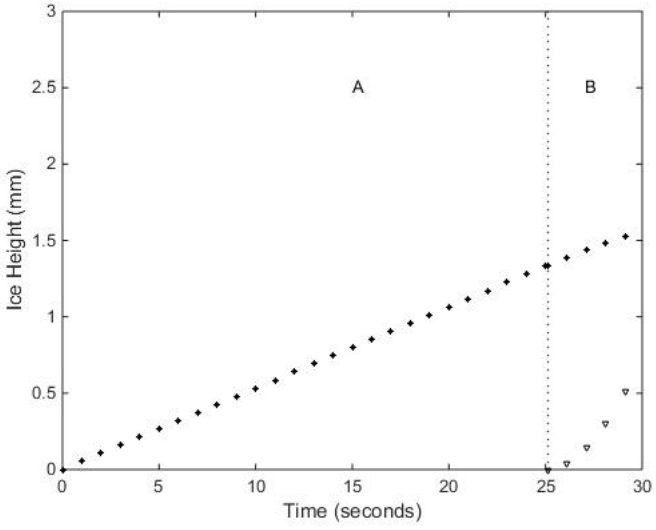


Figure 5.11: Mixed ice accretion model at T_a = -6°C and $\phi = 0.96$.

fraction and ambient temperature on the ice accretion rate and time and transition between different ice regimes. A comparison of Figure 5.8 and 5.9, shows that an increase in the packing fraction from 0.65 to 0.96 while the temperature is fixed at -3°C causes a reduction in overall ice height by 18%. The former also sees a prolonged primary mixed stage corresponding to the lower value of ϕ. Similarly, comparing Figure 5.10 and 5.11,we can observe an increase in the packing fraction from 0.65 to 0.96, while the temperature is fixed at -6°C, causes a reduction in rime and glaze ice height by 37% and 54% respectively. For both cases, it is apparent that higher values of ϕ result in longer rime ice stage, smaller primary mixed stage and drastically affect the ice height, thereby affecting the adhesion characteristics of the accreted ice immensely.

Comparing Figure 5.8 and 5.10, we note the decrease in temperature from -3°C to -6°C whilst the packing fraction is kept constant at 0.65, results in an overall ice height of 1.45 mm (1.25 mm glaze and 0.4 mm mixed) and 2.45 mm (1.2 mm glaze and 1.25 mm rime) respectively. This results in a similar accretion height of glaze, however the former case makes an earlier transition to secondary mixed ice; this is understandable, as this is a pre-requisite to moving onto a glaze ice stage which is favoured at higher temperatures. Similarly, when comparing Figure 5.9 and 5.11, we observe

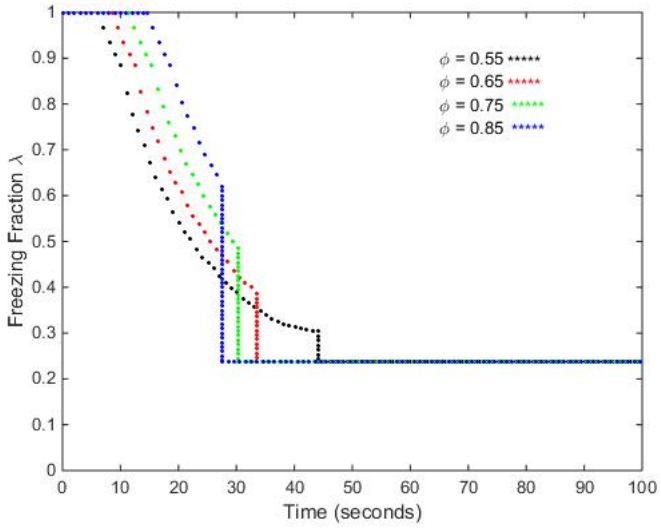


Figure 5.12: Variation in freezing fraction λ with changes in packing fraction ϕ for 100 s.

the decrease in temperature from -3°C to -6°C whilst the packing fraction is kept constant at 0.96 results in an overall ice height of 1.45 mm (0.75 mm glaze and 0.7 mm mixed) and 1.55 mm (0.6 mm glaze and 0.95 mm rime) respectively.

Figures 5.12, 5.13, 5.15, 5.17, 5.19 and 5.21 show the effect of different atmospheric parameters on the freezing fraction λ. The base atmospheric conditions for the plots in all these figures is $\beta = 0.5$, $U_\infty = 90\,\mathrm{m\,s^{-1}}$, $\phi = 0.65$, T_a = -5°C, AoA = 0° and $\rho_a = 0.001\,\mathrm{kg\,m^{-3}}$. Figure 5.12 shows the change in λ with respect to ϕ. We see that keeping all other atmospheric pa-

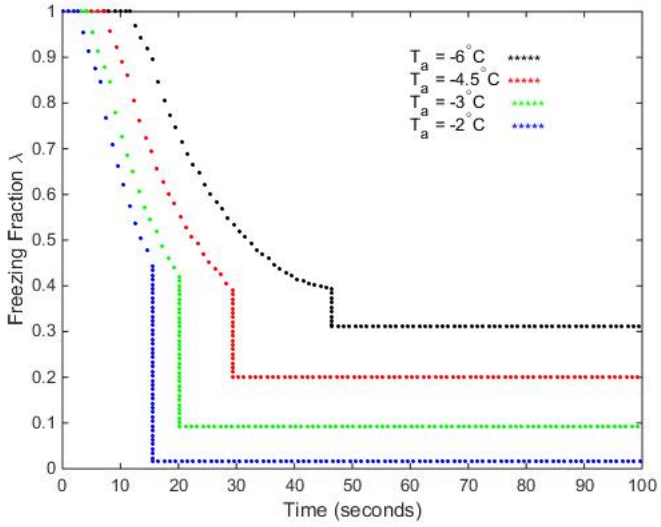


Figure 5.13: Variation in freezing fraction λ with changes in atmospheric temperature T_a for 100 s.

rameters constant, higher values of ϕ increase the time of rime ice accretion and reduce the time of primary mixed ice accretion. The physical interpretation of this trend in the former is since at a fixed height the transition from rime to primary mixed occurs i.e. the total latent heat is no longer conducted through the ice to the wing, this height is obtained faster at greater porosity and lower values of ϕ. Similarly, the primary mixed stage time increases with porosity as a greater amount of void space needs to be filled up by unfrozen water at the surface. Figure 5.13 shows the change in λ with variation in T_a. We can see from the figure that colder temperatures favour longer rime ice accretion and correspondingly longer primary mixed ice accretion. Rime ice

accretion is more pronounced at lower temperatures as supercooled droplets freeze more readily.

5.5.2 Variation of Ice Height and Freezing Fraction λ with Liquid Water Content

Figure 5.14 shows the effect of LWC on the ice height. By doubling the LWC at -3°C, the overall ice height increased from 1.75 mm to 2.45 mm (40%) and the onset of the glaze ice stage is brought on much quicker. At -6°C, doubling the LWC increases the overall ice height from 2.5 mm to 3.3 mm (32%). Similarly, the onset of the glaze ice stage is brought on earlier. In essence, increasing LWC increases ice height and prepones the onset of glaze ice stage.

Figure 5.15 exhibits the effect of ρ_a on λ. We see that as LWC increases, rime ice accretion time decreases and primary mixed ice accretion decreases as well. The reason for this is that at higher LWCs, it is tougher to freeze all of the supercooled droplets and a greater fraction remain unfrozen during the next stage, filling up the porous space at a faster rate.

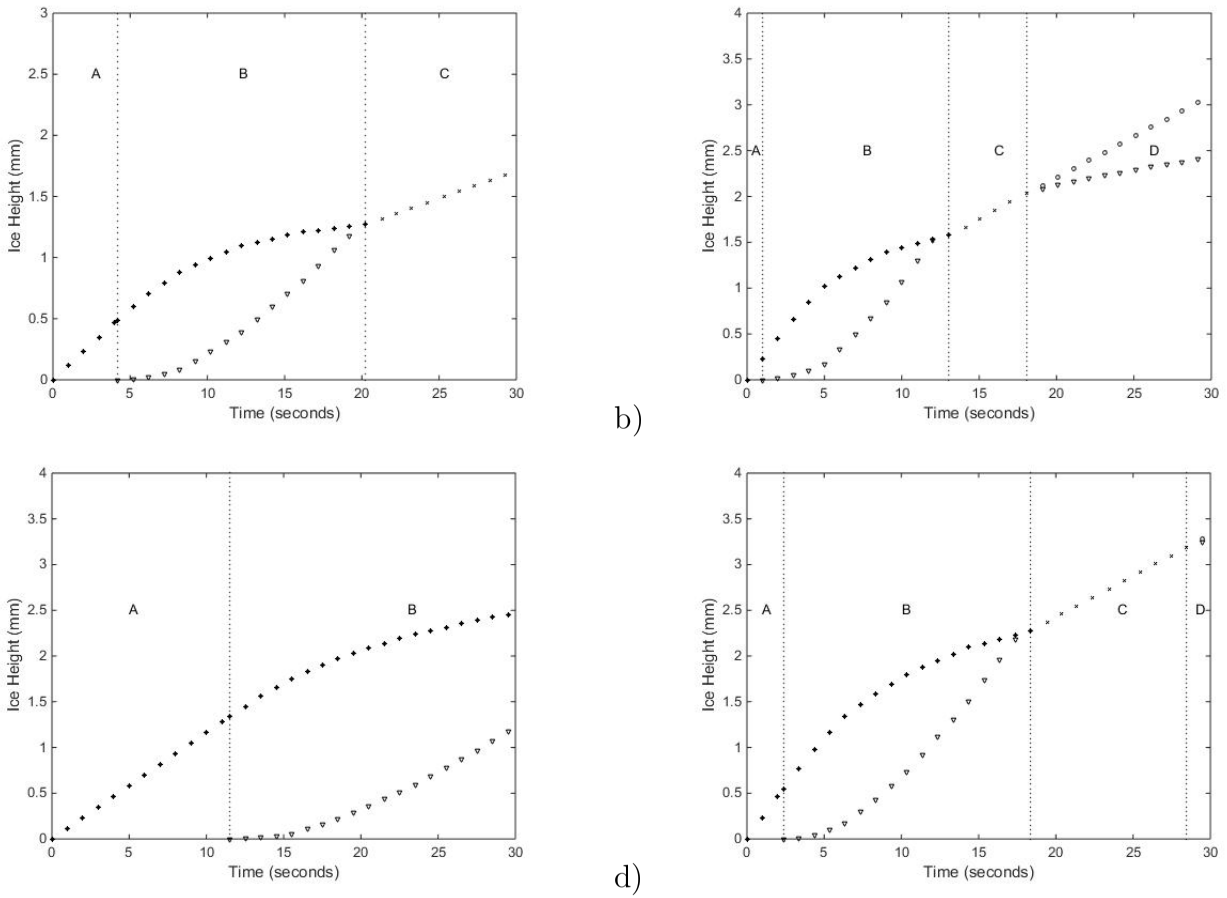


Figure 5.14: Ice accretion versus LWC. 1) T_a = -3°C, $\phi = 0.65$, $\rho_a = 0.001\,\mathrm{kg\,m^{-3}}$. Occurrence of Stage A (0–4 s), B (4–20 s) and C (20–30 s). 2) T_a = -3°C, $\phi = 0.65$, $\rho_a = 0.002\,\mathrm{kg\,m^{-3}}$. Occurrence of Stage A (0–1 s), B (1–13 s), C (13–18 s) and D (18–30 s). 3) T_a = -6°C, $\phi = 0.65$, $\rho_a = 0.001\,\mathrm{kg\,m^{-3}}$. Occurrence of Stage A (0–12 s) and B (12–30 s). 4) T_a = -6°C, $\phi = 0.65$, $\rho_a = 0.002\,\mathrm{kg\,m^{-3}}$. Occurrence of Stage A (0–2 s), B (2–18 s) C (18–28 s) and D (28–30 s).

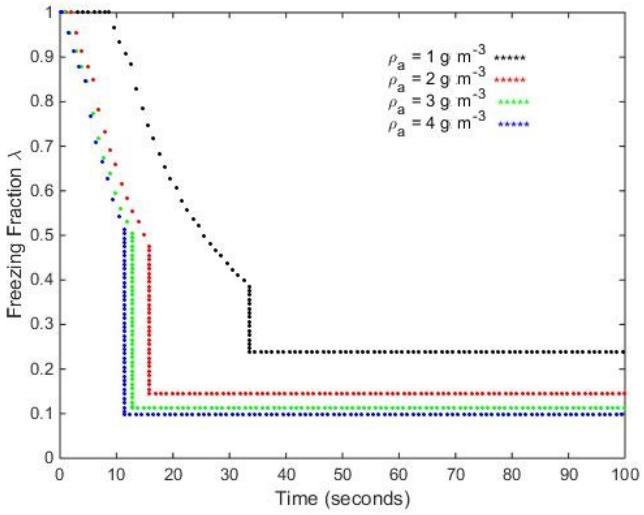


Figure 5.15: Variation in freezing fraction λ with changes in ρ_a for 100 s.

5.5.3 Variation of Ice Height and Freezing Fraction λ with Air Velocity

Figure 5.16 shows the effect of air velocity on the ice height. We note that on doubling the air velocity at -3°C, the overall ice height increased from 1.75 mm to 2.2 mm (26%) and the onset of the glaze ice stage is brought on much quicker. At -6°C, doubling the air velocity increases the overall ice height from 2.5 mm (1.2 mm glaze and 1.3 mm rime) to 2.9 mm (16%). Similarly, the onset of the glaze ice stage is brought on earlier. In essence, increasing air velocity increases ice height and hastens the onset of glaze ice stage.

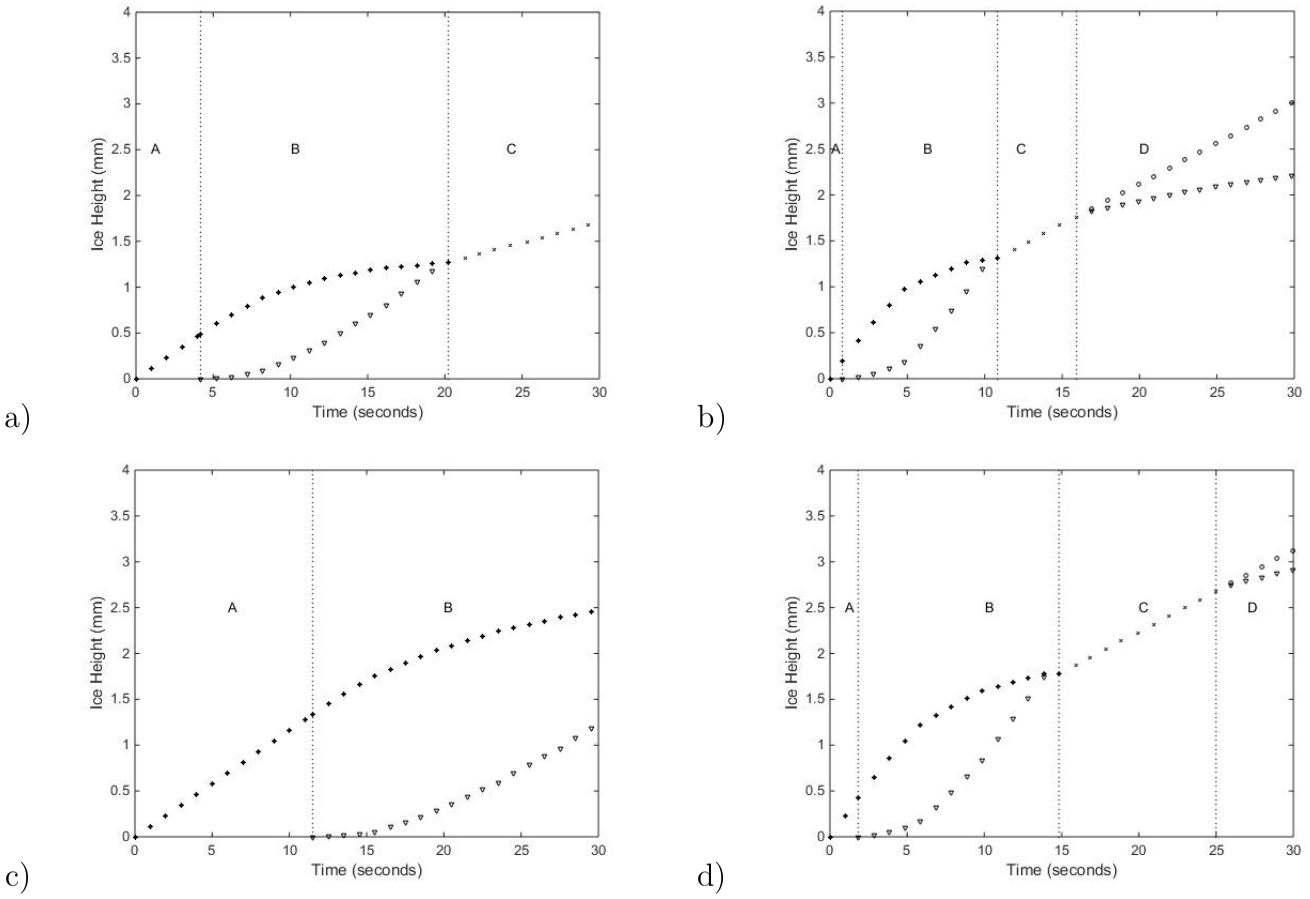


Figure 5.16: Ice accretion versus air velocity. 1) T_a = -3°C, $\phi = 0.65$, $U_\infty = 90\,\mathrm{m\,s^{-1}}$. Occurrence of Stage A (0–4 s), B (4–20 s) and C (20–30 s). 2) T_a = -3°C, $\phi = 0.65$, $U_\infty = 180\,\mathrm{m\,s^{-1}}$. Occurrence of Stage A (0–1 s), B (1–11 s), C (11–16 s) and D (16–30 s). 3) T_a = -6°C, $\phi = 0.65$, $U_\infty = 90\,\mathrm{m\,s^{-1}}$. Occurrence of Stage A (0–12 s) and B (12–30 s). 4) T_a = -6°C, $\phi = 0.65$, $U_\infty = 180\,\mathrm{m\,s^{-1}}$. Occurrence of Stage A (0–2 s), B (2–15 s), C (15–25 s) and D (25–30 s).

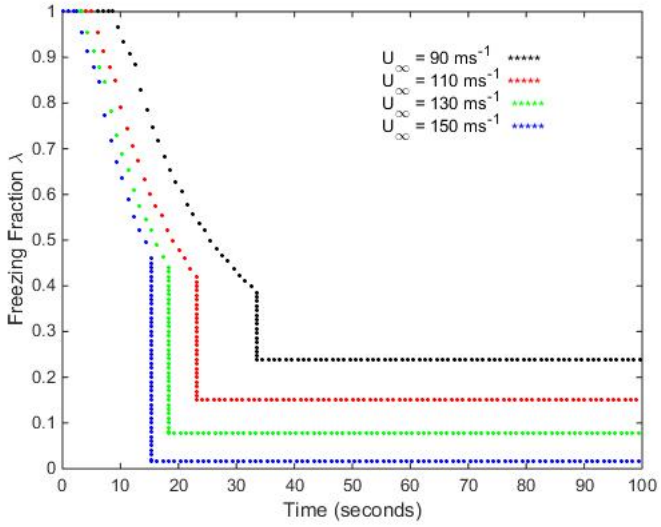


Figure 5.17: Variation in freezing fraction λ with changes in U_∞ for 100 s.

Figure 5.17 exhibits the effect of U_∞ on λ. We see that as air velocity increases, rime ice accretion time decreases and primary mixed ice accretion decreases as well. The reason for this is that at higher air velocity, the supercooled droplets have higher kinetic energy and the effect of aerodynamic heating is larger. In reality, such conditions also enable a wider region of droplet impact on the wing.

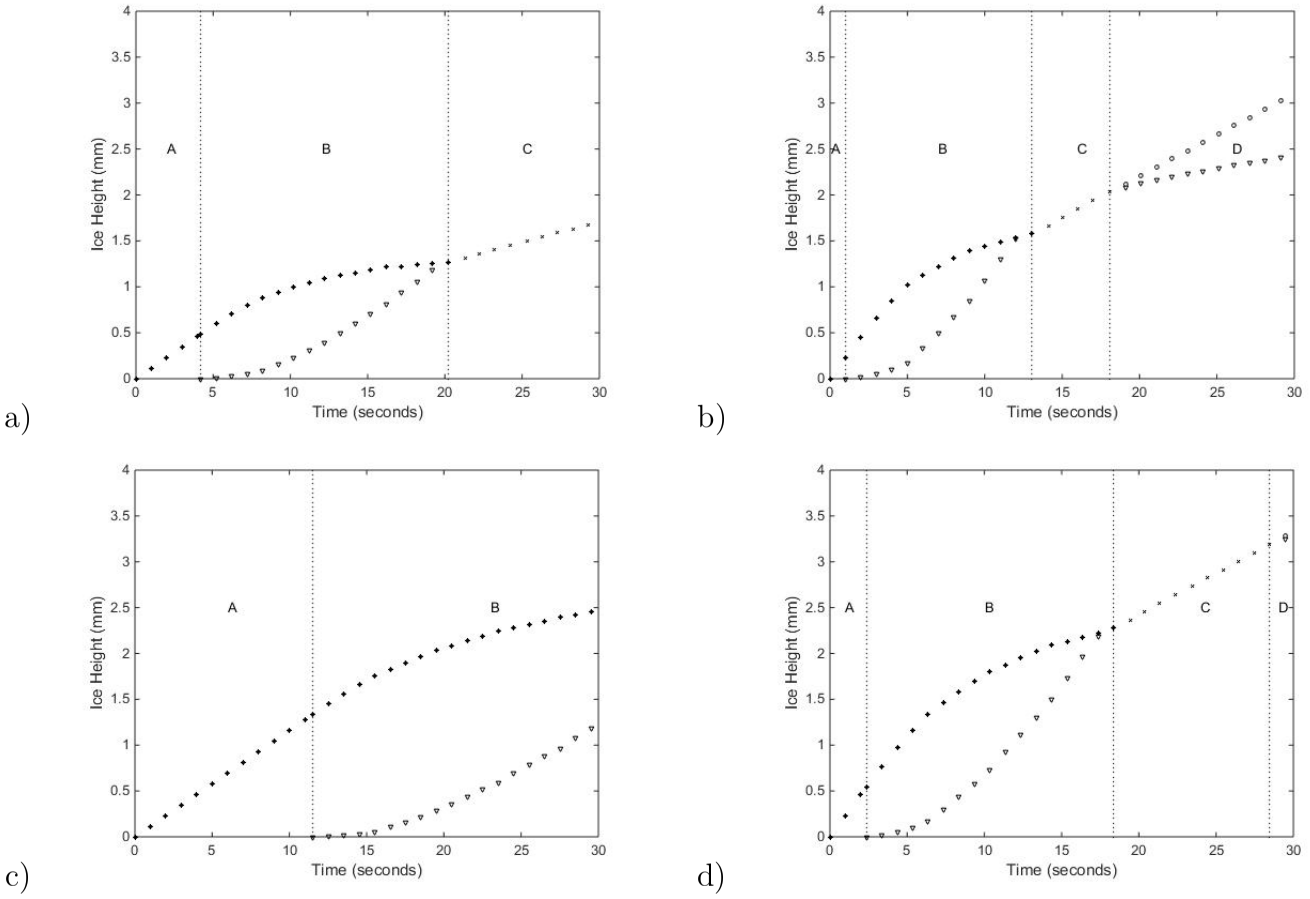


Figure 5.18: Ice accretion versus air velocity. 1) T_a = -3°C, ϕ = 0.65, β = 0.5. Occurrence of Stage A (0–4 s), B (4–20 s) and C (20–30 s). 2) T_a = -3°C, ϕ = 0.65, β = 1. Occurrence of Stage A (0–1), B (1–13 s), C (13–18 s) and D (18–30 s). 3) T_a = -6°C, ϕ = 0.65, β = 0.5. Occurrence of Stage A (0–12 s) and B (12–30 s). 4) T_a = -6°C, ϕ = 0.65, β = 1. Occurrence of Stage A (0–2 s), B (2–18 s), C (18–28 s) and D (28–30 s).

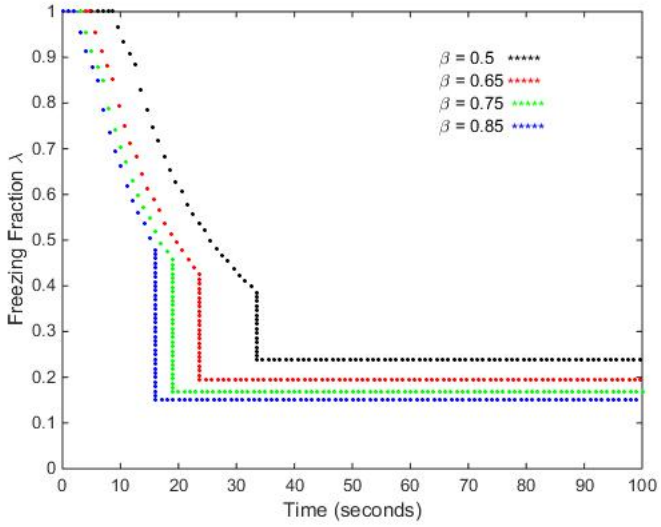


Figure 5.19: Variation in freezing fraction λ with changes in β for 100 s.

5.5.4 Variation of Ice Height and Freezing Fraction λ with Collection Efficiency

Figure 5.18 shows the effect of collection efficiency on the ice height. By doubling the collection efficiency at -3°C, the overall ice height increased from 1.75 mm to 2.45 mm (40%) and the onset of the glaze ice stage is brought on much quicker. At -6°C, doubling the collection efficiency increases the overall ice height from 2.5 mm (1.2 mm glaze and 1.3 mm rime) to 3.3 mm (32%). Similarly, the onset of the glaze ice stage is brought on earlier. In essence, increasing collection efficiency increases ice height and prepones the onset of glaze ice stage.

Figure 5.19 exhibits the effect of β on λ. We see that, as collection efficiency increases, rime ice accretion time decreases and primary mixed ice accretion decreases as well. The reason for this, is that at higher collection efficiency, a greater number of supercooled droplets are incident on the surface; thereby increasing the total latent heat required to be conducted away by the wing.

5.5.5 Variation of Ice Height and Freezing Fraction λ with Angle of Attack

Figure 5.20 shows the effect of angle of attack (AoA) on the ice height. Realistically, changes in AoA will affect collection efficiency but in this one-dimensional scenario, we consider constant $\beta = 0.5$. By increasing the AoA by 10° at -3°C, the overall ice height decreased from 1.75 mm to 1.7 mm (3%) which within an application is a negligible change. At -6^{deg}C, increasing AoA by 10° decreases the overall ice height from 2.5 mm (1.2 mm glaze and 1.3 mm rime) to 2.45 mm (1.15 mm glaze and 1.3 mm rime). This culminates in a 2% decrease in the overall ice height and a 4% decrease in the height of the glaze ice. Similar to the previous case, the effect is negligible for a significant change in AoA. In conclusion, solely by changing the AoA, within reasonable

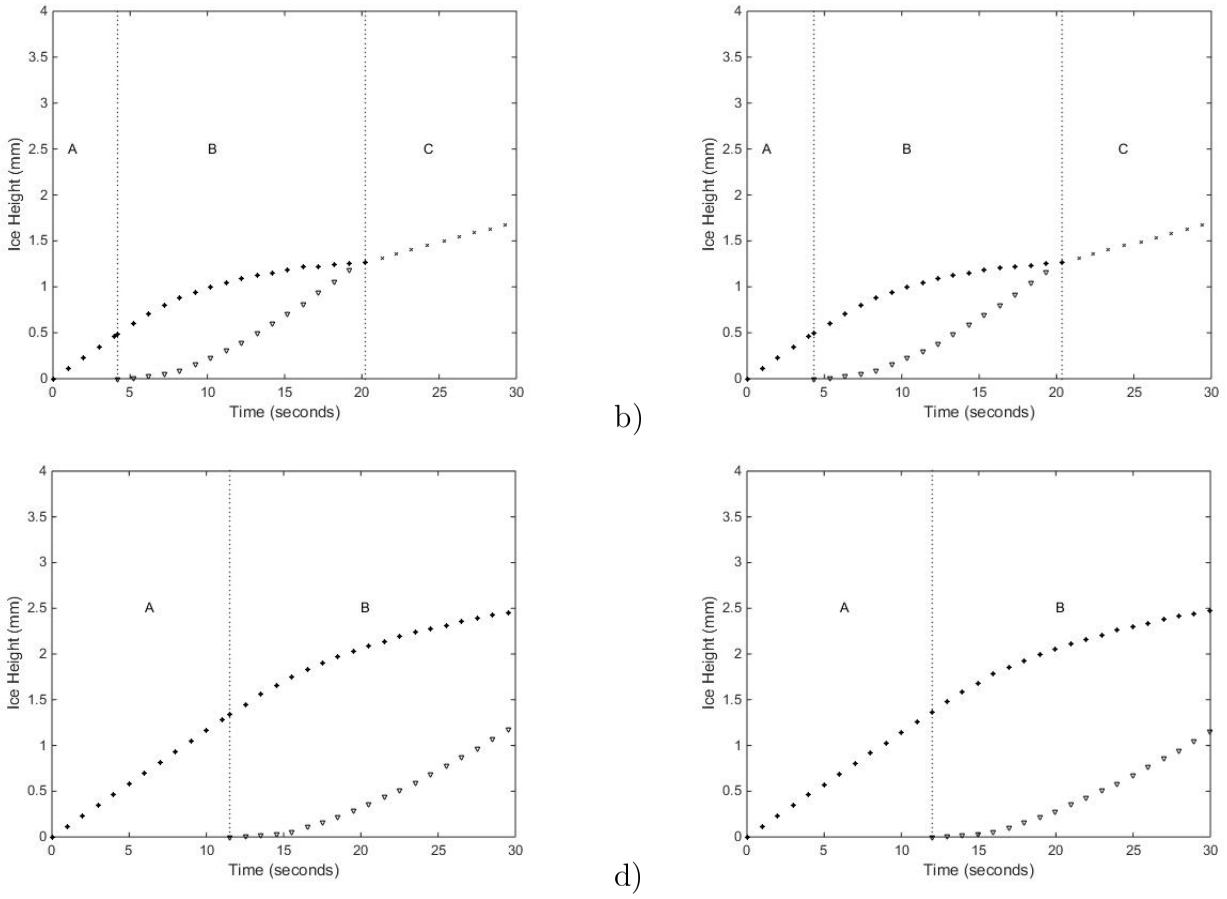


Figure 5.20: Ice accretion versus angle of attack. 1) T_a = -3°C, $\phi = 0.65$, $AoA = 0\circ$. Occurrence of Stage A (0–4 s), B (4–20 s) and C (20–30 s). 2) T_a = -3°C, $\phi = 0.65$, $AoA = 10\circ$. Occurrence of Stage A (0–4 s), B (4–20 s) and C (20–30 s). 3) T_a = -6°C, $\phi = 0.65$, $AoA = 0\circ$. Occurrence of Stage A (0–12 s) and B (12–30 s). 4) T_a = -6°C, $\phi = 0.65$, $AoA = 10\circ$. Occurrence of Stage A (0–12 s) and B (12–30 s).

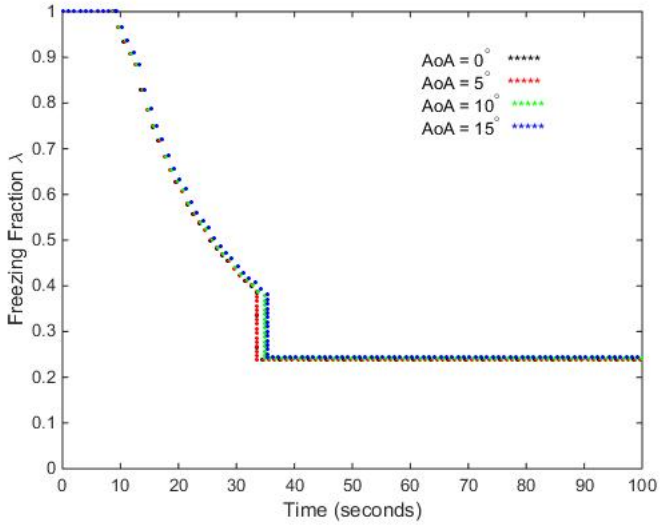


Figure 5.21: Variation in freezing fraction λ with changes in AoA for 100 s.

limits, has a negligible effect on the overall ice height and the onset of different stages in the accretion process.

Figure 5.21 exhibits the effect of AoA on λ. We see that changes in the AoA have a minimal effect on λ. This is because the changes in AoA within relevant values, do not affect the overall mass flux of incident supercooled droplets sufficiently enough to change the thermodynamics of the accretion process.

5.5.6 A Comparison with Myers and Charpin Code

Figures 5.22 and 5.23 describe the ice growth according to the traditional glaze ice model [5]; taking values $\phi = 0.96$ and ambient temperature of -3°C and -6°C respectively. For figures 5.22 and 5.23, the different accretion limits are represented as rime $(*)$, glaze $(--)$ and water film $(+)$.

Comparing Figure 5.9 and 5.22, the author's model prediction results in an overall ice height of 1.45 mm as compared to the glaze model [5] height of 1.1 mm; we note only 0.7 mm of the former is glaze which has different adhesion characteristics than rime or mixed. Similarly when comparing figure 5.11 and 5.23, the author's model prediction results in an overall ice height of 1.55 mm as compared to the glaze model [5] height of 1.5 mm; only 0.6 mm of the former is glaze which has different adhesion characteristics than rime or mixed. At smaller accretion times, the difference between the two models is greater and as the temperature tends to 0°C, the models give similar accretion height predictions. Table 5.2 exhibits the differences between the author's model which consistently predicts a lower glaze ice height than the glaze ice model [5] at accretion time of 30 seconds and $\phi = 0.96$.

Figure 5.24 exhibits the change in overall accretion height at 60 seconds with variation in ϕ. Apparent from the results is the height consistently

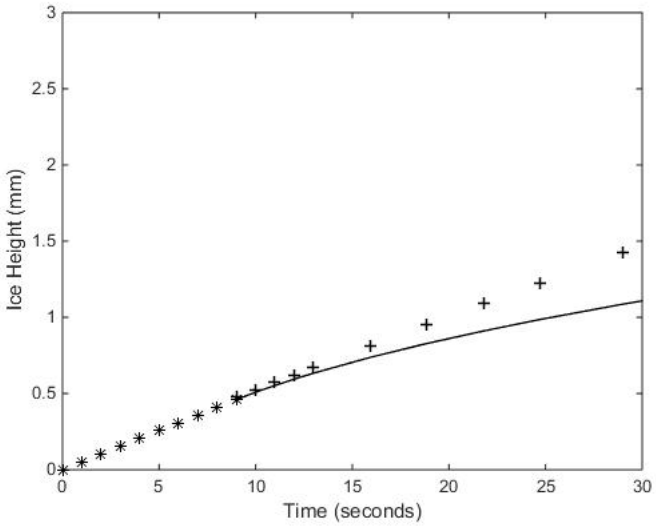


Figure 5.22: Ice growth due to glaze ice model [5] at T_a = -3°C and $\phi = 0.96$.

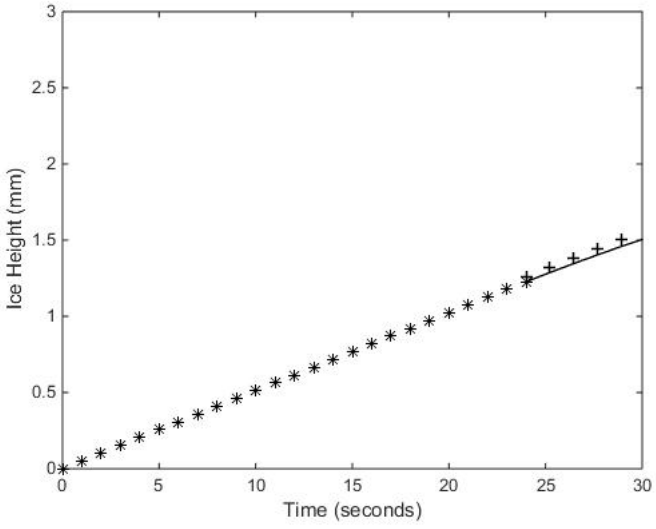


Figure 5.23: Ice growth due to glaze ice model [5] at T_a = -6°C and $\phi = 0.96$.

increases with a reduction in ϕ. It is also worth noting that secondary mixed ice occurs due to the dual freezing action exhibited by instantaneous freezing of a fraction of the supercooled droplets at the air-rime interface and freezing at the Stefan interface. This implies that the formation of the thin film may occur later than initially expected on an aircraft wing. In the glaze ice model [5], the water film appears immediately after the rime stage whereas in the author's model, the water film appears much later after secondary mixed ice stage.

In terms of a qualitative comparison, Myers (2001) [5] grew ice in a wind tunnel under conditions of mass flux = $0.0495\,\mathrm{kg\,m^{-2}s^{-1}}$. The temperature of the wind tunnel was kept at -10°C and the overall accretion time was 12 minutes. It was reported that the height of the rime ice during transition to glaze was between 2–3 mm and occurred at approximately 46 seconds. Using our predictions, a packing fraction range of 0.87–0.98 gives us an ice height of 2.9–2.6 mm at the same accretion time which is an encouraging sign covering different density values of hard rime.

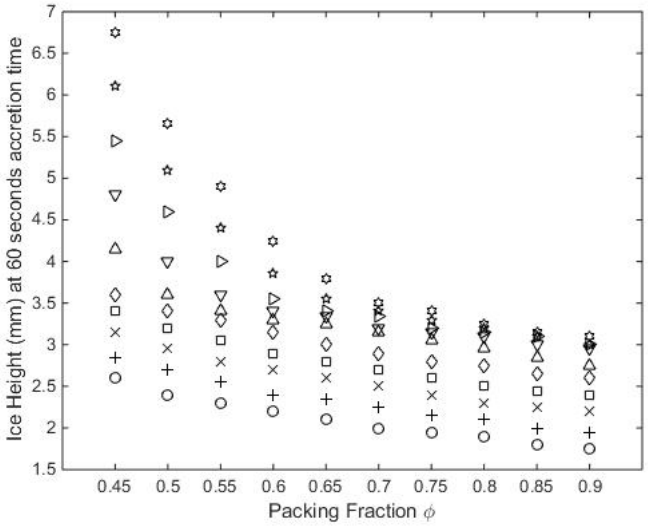


Figure 5.24: Overall ice height variation with changes in ϕ at -3°C ($\circ$), -3.5°C ($+$), -4°C (x), -4.5°C ($\square$), -5°C ($\diamondsuit$), -5.5°C ($\triangle$), -6°C ($\bigtriangledown$), -6.5°C ($\triangleright$), -7°C ($\star$) and -7.5°C ($*$).

Table 5.2: Ice height comparison between author's model and glaze ice model [5].

T_f	**Rime [5]**	**Glaze [5]**	**Water [5]**	**Rime**	**Glaze**	**Water**	**Mixed**
-2	0	**0.9**	0.5	0	**0.65**	0.2	0.55
-3	0	**1.1**	0.4	0	**0.75**	0	0.7
-4	0	**1.3**	0.2	0	**0.9**	0	0.25
-5	0	**1.4**	0.1	0	**1.25**	0	0.25
-6	0	**1.5**	0.05	0.75	**0.8**	0	0

5.5.7 A Comparison with Experimental Data

It is important at this stage of the model development to test computational results with actual experimental results in an icing facility. For this purpose, we consider two studies. Palacios et al. (2010) [103] conducted icing experiments on an Adverse Environment Rotor Test Stand (AERTS). Essentially, the experiment consisted of 1 inch diameter-50 inch radius rotor connected to a 125 HP motor; inside a cold chamber with nozzle location on the ceiling. Similar tests were conducted by Ruff (1985) [104] in the Air Force Arnold Engineering Development Center. Since packing fraction ϕ is currently not

linked to the freezing fraction λ in our code and no density measurements regarding the accreted ice in the experimental facility are currently available for comparison [103, 104]; we assumed rime ice density as $880\,\mathrm{kg\,m^{-3}}$ and subsequently $\phi = 0.96$.

AoA was kept at 0° and β was calculated from Palacios et al. (2010) [103] as $\sim$0.7. Table 5.3 shows the comparison of results from the author's model and experimental data. We see that for a wide array of icing conditions, discrepancies are between 2.3–6.7%. The ice height from the experimental data was measured from the stagnation point. The errors accumulated are due to calculation of collection efficiency and LWC and no comparison of the packing fraction. This is an area of future research to build upon.

5.6 Conclusion

A one dimensional mixed ice accretion model has been developed that incorporates rime ice, glaze ice and mixtures of both. We pose a dimensionless parameter λ, that is the proportion of incoming droplets that freezes to describe the accretion of mixed ice on an aerofoil. An energy balance predicts the values of λ that are achievable at given atmospheric conditions, and these

Table 5.3: Ice height comparison between author's model and experimental data. *Experimental data in comparison to author's model.

T_a (°C)	U_∞ ($\mathrm{m\,s^{-1}}$)	ρ_a ($\mathrm{g\,m^{-3}}$)	t (s)	Author's Model (mm)	Experimental Results (mm)	Percentage Difference* (%)	Reference
-10	66.5	2.35	180	8.7	8.3	-4.8	[103]
-15	66.5	2.55	180	13.6	13.3	-2.3	[103]
-5.5	60.9	1.3	150	4.5	4.4	-2.3	[103]
-15	60.9	1.2	150	9.5	8.9	-6.7	[104]
-6.7	60.9	1.2	300	8	8.5	+6.3	[104]

values match well with previous ice formation observations. This mixed ice model reduces to the glaze ice model [5] when λ=0 and states that the model [5] is valid only for atmospheric temperatures between -1.77° and 0°C. It predicts lower glaze ice heights than previous models [5, 22, 50] at lower atmospheric temperatures. Lower temperatures favour higher ice growth and increasing the packing fraction corresponds to lower ice height and glaze icing regime.

Future work will include determining a time-varying value of freezing fraction to extend the analysis to longer accretion times, and the consideration of variations in water film temperatures and the effect of droplet size. Eventually, the model will be expanded to account for two-dimensional accretion on an aircraft wing including runback water effects.

Chapter 6

Two-dimensional Mixed Ice Accretion Model

6.1 Introduction

This chapter builds upon the one-dimensional code in Chapter 5 to investigate the two-dimensional ice profile due to the flow of water within a porous rime matrix above a layer of growing glaze ice.

Whilst one-dimensional models are useful in quantifying the ice height at different atmospheric conditions, they provide little insight into the spatial profile of the accretion and the variation of height with space co-

ordinate from the leading wing edge. To quantify two-dimensional accretion, we need to include the effect of the flow of water derived from droplet collection on the characteristics of ice. Previously, we have described four distinct stages of ice formation in Chapter 5: namely rime, primary mixed, secondary mixed and glaze. The first three stages do not include the presence of a water film and hence any changes in the ice height are directly dependent on the quantity of incident supercooled droplet flux. The glaze stage includes the presence of a water film but under the parameters investigated in Chapter 5; we have thus far seen supercooled droplets directly impacting the film.

In this chapter, we explore a scenario where supercooled droplets impact a porous rime matrix above a layer of growing glaze ice. This is analogous to flow within a mushy layer although the method of formation of the porous structure is not due to the rejection of solute at the solidifying interface; but due to partial solidification of supercooled droplets on impact.

Natural geophysical processes typically involve solidification such as the formation of a glacier or iceberg; morphological instability generally occurs during the growth of the solid phase [105]. This is characterised by the formation of a thin, multi-phase transition layer known as the "mushy layer" which consists of a liquid and solid fraction in a reactive, porous medium [99]. Numerous studies have already been conducted on the effect of heat

transfer through the mushy layer leading to the formation of ice from a liquid-brine solution in order to understand natural processes better [106, 107, 108, 109, 110, 111]. However, all of these systems treat the mushy layer as a two-phase zone (solid and liquid) neglecting the inclusion of air and rely on natural convection due to a concentration or temperature related gradients generating heat transfer.

Little definitive study exists on the inclusion of a mushy layer during glaze or runback ice formation. Neufeld et al. (2010) [112] reported that the solidification process in ice accretion is inherently unstable due to the evolution and deformation of the free-boundary between liquid and solid during heat transfer. There is an ongoing debate regarding the role of conduction versus convection as the primary mode of heat transfer through the mushy layer. The transient variations of the solid and void fraction undoubtedly influence the heat transfer to some extent but the large shear force of the air field will suppress any minor density variations between the liquid and solid growing phases; this can lead to forced convection as an obvious mode of heat transfer [113]. In this chapter, the layer will be treated as a three-phase zone comprising of solid ice, liquid and air pockets. Some of the important heat transfer parameters in this case become the thickness, solid fraction, porosity and temperature gradient across the liquid-mushy and mushy-ice interface.

Measurements on the solid fraction and porosity of a mushy layer have also been studied [114, 115]. These studies form useful reference points for data collection in our research.

Worster (1997) [91] in his review of free convection through mushy layers ascertained that convection processes begin only after a certain depth (and subsequent Rayleigh number) and formed "chimneys" beyond even a greater value of depth in the medium. These chimneys or freckles are vertical regions of zero solid fraction that form in the mushy layer. Alternative reasons proposed regarding the formation of freckles range from the addition of impurities into the solidifying liquid [116], to the reduced permeability as an intrinsic property of the cooling system [117]. Neufeld and Wettlaufer (2008a) [118] and Neufeld and Wettlaufer (2008b) [119] studied the effects of shear-enhanced convection on a mushy layer using experimental and modelling techniques. The experimental setup included a laboratory flume, where water was pumped through straw baffles to induce laminar shear force over a test section containing the growing mushy layer of aqueous ammonium chloride. The results show, that for multiple values of the external flow velocity between 5.6–13 $\mathrm{cm\,s^{-1}}$, the shear force drove instability through the mushy layer resulting in forced convection becoming the sole mode of heat transfer and leading to the formation of freckles. The Reynold's number

(see Appendix B) for the system can be calculated from typical values of the length L (1.6 m), upper limit of velocity V (13 $\mathrm{cm\,s^{-1}}$) and kinematic viscosity ν (approximately 0.01 $\mathrm{cm^2\,s^{-1}}$ at $20°C$). The associated Reynold's number $\mathcal{RE} = \frac{VL}{\nu}$, we attain a value of $\mathcal{RE} = 2.08{\times}10^5$. Considering the respective length scale (aircraft wing upper surface) and velocity of water film ($\leq 10\,\mathrm{cm\,s^{-1}}$ based on estimates) being similar on an actual aircraft in flight, the assumption for shear enhanced convection being the sole driver of heat transfer through the mushy layer seems plausible, based on the above comparison.

In this work, we adapt the work of Beavers and Joseph (1967) [120] who performed experiments on the effect of overlying shear on flow within a porous block. These authors determined that the flow could be expressed as a statistical average of the overlying fluid speed dependent upon the pore size for different materials. They also found qualitatively that, as the flow rate of the overlying water increased, a proportional increase was seen in the flow rate of the porous flux expressed as a fraction of flow such as described by Darcy's law. We will use this approach to describe flow within the rime matrix as an averaged porous flux of a fraction of the overlying wind speed. The source of water within the porous matrix will not be limited to the incident supercooled droplet flux but also to runback water from parts of the

wing closer to the leading edge. Electro-thermal heating mats are currently employed in commercial aircraft to melt ice which accretes near the leading edge of the wing. When the ice does not evaporate completely to the atmosphere, it runs back as a thin film along the wing. The effect of runback water, without consideration of supercooled droplets on the growth rate of glaze ice has previously been studied [59]. In this work, we take this phenomena one step further to study ice growth rates when runback water acts as an external mass source to ice already accreting further down the wing due to impinging supercooled droplets.

6.2 Mathematical Formulation

The two-dimensional code derived in this section is applicable to the scenario of supercooled droplet impact on secondary mixed ice (see Figure 6.1). For simplicity, we take a height h_m as initial conditions for our calculations at time $t = 0$.

The overall mass balance is given by,

$$\dot{M} = \phi_i \rho_i \frac{\partial r}{\partial t} + (1 - \phi_i)\rho_w \frac{\partial R}{\partial t} + (1 - \phi_i) U_s \rho_w \frac{\partial R}{\partial x} + (1 - \phi_i)\rho_i \frac{\partial b}{\partial t}, \qquad (6.1)$$

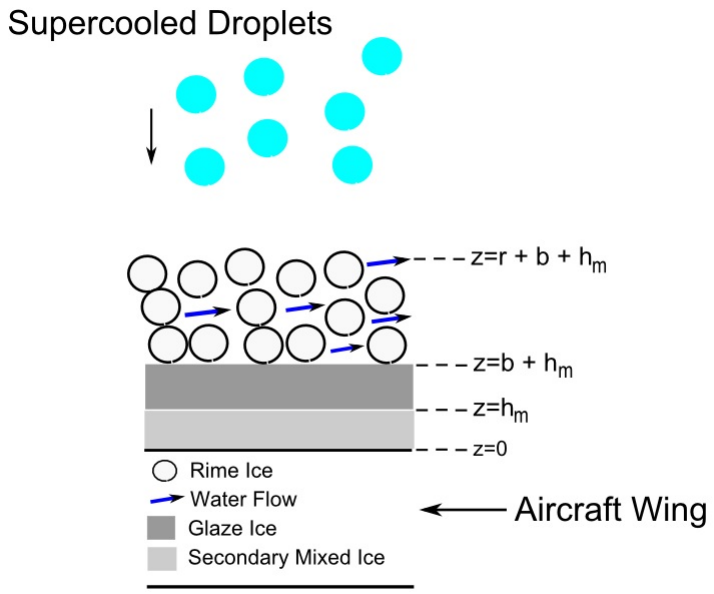


Figure 6.1: Schematic of two-dimensional ice accretion on an aerofoil.

where ϕ_i is the packing fraction of the ice in the porous rime layer r, b is the glaze ice height, ρ_i and ρ_w are the densities of glaze ice and water respectively. Additionally, U_s is the depth-averaged velocity of the water inside the rime matrix given by $U_s = \eta U_\infty$ where $\eta = 0.1$; see Beavers and Joseph (1967) [120] based on a statistical value of flow velocity inside a porous layer driven by an overlying shear. A saturation flux is $R = \alpha(x,t)r(x,t)$ where α is the saturation parameter, i.e. the level of saturation of the porous layer that is saturated with water ($0 < \alpha \leq 1$). In the special cases $\alpha = 0$, there is no water present inside the rime layer and when $\alpha = 1$, the rime layer is fully saturated. More generally α is given by

$$\alpha = \frac{\phi_w}{(1-\phi_i)}, \tag{6.2}$$

where ϕ_w is the packing fraction of liquid inside the rime layer and ϕ_a is the fraction of void space in the rime layer. A limitation is if α becomes larger than 1; when $\phi_w \geq \phi_a$. We separate the mass balance in equation 6.1 using the freezing fraction λ (see equation 5.30). The solid mass balance is

$$\lambda \dot{M} = \phi_i \rho_i \frac{\partial r}{\partial t}. \tag{6.3}$$

Integrating equation 6.3 with initial conditions at $t = 0$, $r = h_m$, we get

$$r = \frac{\lambda \dot{M} t}{\phi_i \rho_i} + h_m. \tag{6.4}$$

The growth of the glaze ice is given by the reduced Stefan condition considering isothermal water above the growing interface (see equation 5.34)

$$(1-\phi_i)\rho_i L_f \frac{\partial b}{\partial t} = \frac{k_i(T_f - T_s)}{b}. \tag{6.5}$$

Integrating equation 6.5 with initial conditions at $t = 0$, $b = h_m$,

we get

$$b = \sqrt{\frac{2k_i(T_f - T_s)t}{((1-\phi_i)\rho_i L_f)}} + h_m. \tag{6.6}$$

It is important to note that $r > b$ for the porous rime layer to exist. For if $b > r$, only solid secondary mixed ice is present.

The liquid mass balance is given by,

$$(1-\lambda)\dot{M} = (1-\phi_i)\rho_w \frac{\partial R}{\partial t} + (1-\phi_i)U_s\rho_w \frac{\partial R}{\partial x} + (1-\phi_i)\rho_i \frac{\partial b}{\partial t}. \tag{6.7}$$

Rearranging the terms gives us a governing partial differential equation for R that is time and spatially varying:

$$\frac{\partial R}{\partial t} + U_s \frac{\partial R}{\partial x} = \left[(1-\lambda)\dot{M} - (1-\phi_i)\rho_i \frac{\partial b}{\partial t}\right] \frac{1}{(1-\phi_i)\rho_w}. \tag{6.8}$$

The term within the brackets in the RHS must be positive as a second condition for water to be present. Essentially a positive value denotes that after water is removed from the unfrozen fraction on impact of supercooled droplets for the formation of glaze ice, there is an amount left over

that flows through the porous rime matrix at speed U_s. Substituting for the partial derivative of b from equation 6.5 into 6.8, we get

$$\frac{\partial R}{\partial t} + U_s \frac{\partial R}{\partial x} = \left[(1-\lambda)\dot{M} - \frac{k_i(T_f - T_s)}{L_f b} \right] \frac{1}{(1-\phi_i)\rho_w}. \tag{6.9}$$

We also include the possibility of runback water input to the system from melted ice near the leading edge of the wing. It is important as a first estimation to determine an appropriate mass flux of runback water. Subsequent scenarios can vary greatly due to factors such as the quantity and type of ice melted, power and application time of the electro-thermal mats etc. When the electro-thermal mats are switched on, the total amount of power E required to melt ice at an arbitrary temperature T_i (below T_f) to water at T_f (which is when it begins to first flow) is

$$E = \dot{M}_{rb} c_i (T_f - T_i) + \dot{M}_{rb} L_f, \tag{6.10}$$

where $\dot{M}_{rb}$ is the rate of ice melting (mass rate) and c_i is the specific heat capacity of ice. We note, the amount of power required to increase the temperature of the ice to T_f is significantly lower than latent heat that must be supplied to convert ice at T_f to water at T_f. Correspondingly in this case,

the first term in the RHS of equation 6.10 can be neglected. Rearranging equation 6.10 for M_{rb} gives us

$$\dot{M}_{rb} = \frac{E}{L_f}. \tag{6.11}$$

An estimate of relevant parameter values is given from considering GKN Aerospace B787 heater mats consume $\approx$ 45–75 kW [121]. Assuming the upper limit of power consumption, $E = 75000\,\mathrm{W}$. In this case, $M_{rb} = 0.22\,\mathrm{kg\,s^{-1}}$. The protected surface area of a wing A_i having a gross area of $122.4\,\mathrm{m^2}$, is $5.7\,\mathrm{m^2}$ [121]. The total mass flux of runback water in $\mathrm{kg\,m^{-2}s^{-1}}$ is:

$$\frac{\dot{M}_{rb}}{A_i} = 0.039\frac{kg}{m^2 s}. \tag{6.12}$$

It must be noted that this calculation assumes that a constant quantity of ice is melted per second which may be an overestimate since the electro-thermal mats are only switched on at intervals when the quantity of ice accreted near the leading edge is detrimental to flight characteristics. However, at the leading edge of the wing, the mass flux of supercooled droplets impinging to form the growing ice can equalize the value over a prolonged accretion period of 1–3 minutes. If the aircraft exits a cloud structure

with ice on the leading edge of the wings and the electro-thermal mats are switched on. This special condition will be discussed within the later analysis. The liquid mass balance with the inclusion of runback water becomes

$$\frac{\partial R}{\partial t} + U_s \frac{\partial R}{\partial x} = \left[(1-\lambda)\dot{M} + \frac{M_{rb}}{A_i} - \frac{k_i(T_f - T_s)}{L_f b} \right] \frac{1}{(1-\phi_i)\rho_w}. \qquad (6.13)$$

6.2.1 Solution Procedure

The numerical solution procedure for the results in (x,t) are obtained in this chapter are determined by incremental time steps, for a single time step as:

1. Determine a suitable numerical index for the dimensionless space-coordinate $\tilde{x}$. We use $\tilde{x}$ from -1 $\leq \tilde{x} \leq$ 2 for $\triangle x$ (space grid step) = i/100 (i = 0:300). This grid space provides accurate resolution for order of magnitude used in our finite difference scheme.

2. Solve equation 6.4 to determine r with respect to x dependent upon values of λ and $\dot{M}$ with respect to i.

3. Solve equation 6.6 to determine b which is constant across all values

of x. We note r must be greater than b for all values of x; otherwise we plot only b as solid secondary mixed ice.

4. The next step is to solve the PDE 6.9 to determine the saturation flux R. We use a first-order finite difference approach. Denoting $R(x_j, t_n) = R_j^n$ where x_j (time step) $= j \triangle x$ and $t_n = n \triangle t$. Taking the RHS of equation 6.9 as Q_j^n to simplify the discretization process, for a constant value of U_s ($U_s > 0$) we get

$$\frac{R_j^{n+1} - R_j^n}{\triangle t} + U_s \frac{R_j^{n+1} - R_j^n}{\triangle x} = Q_j^n. \tag{6.14}$$

Rearranging the terms, we obtain

$$R_j^{n+1} = R_j^n - r(R_j^{n+1} - R_j^n) + \triangle t Q_j^n, \tag{6.15}$$

where $r = \frac{\triangle t U_s}{\triangle x}$. For an explicit scheme such as this, $\mid r \mid < 1$. The accuracy of this scheme is of $O(\triangle x) + O(\triangle t)$. It is worth noting here that Q_j^n must be positive for water to flow through the rime layer. If $Q_j^n \leq 0$, we plot r as secondary mixed ice (avoiding the differentiation between individual rime and glaze boundaries).

5. We now calculate $\alpha(x,t) = \frac{R}{r}$ and $\phi_w(x,t)$ (equation 6.2) for all values of x. ϕ_w must be less than or equal to $(1-\phi_i)$ and α must be less than or equal to 1. If these two conditions are met, go to Step 2 for the next time step. If $\alpha > 1$, the supercooled droplets impact water directly. This scenario is not considered for two-dimensional modelling in this case. For the inclusion of runback water, solve Step 5 in an identical manner replacing equation 6.9 by equation 6.13.

6.3 Results and Analysis

This section will consist of non-dimensionalised equations to provide an analysis applicable to a wide range of similar mechanisms; dimensionalised solutions of the equations to determine the profile under different conditions seen in nature such as ascent/descent through clouds etc.; and the effect of runback water on the growth and profile of ice accretion.

6.3.1 Non-Dimensionalisation

No Freezing from Substrate Upwards

In the first instance, we consider a simple one-dimensional solution excluding freezing from the substrate upwards. In this case, we assume there is no glaze ice forming within the porous matrix. Essentially, this implies that the frozen fraction grows as the solid fraction of the porous layer, while the unfrozen fraction flows through the porous layer driven by the overlying shear of air speed. The adapted liquid mass balance from equation 6.9 for this scenario is

$$\frac{\partial R}{\partial t} + U_s \frac{\partial R}{\partial x} = \frac{(1-\lambda)\dot{M}}{(1-\phi_i)\rho_w}. \tag{6.16}$$

As a first step, we derive a time scale parameter applicable to equation 6.16. Setting $\frac{r}{\tilde{r}} = r^*$ and $\frac{t}{\tilde{t}} = t^*$ in equation 6.3, we get

$$\lambda \dot{M} = \frac{\phi_i \rho_i \tilde{r}}{\tilde{t}} \frac{\partial r^*}{\partial t^*}. \tag{6.17}$$

In this and all future notation, $\sim$ refers to the characteristic dimensional scale and $*$ refers to the non-dimensional quantity. Rearranging

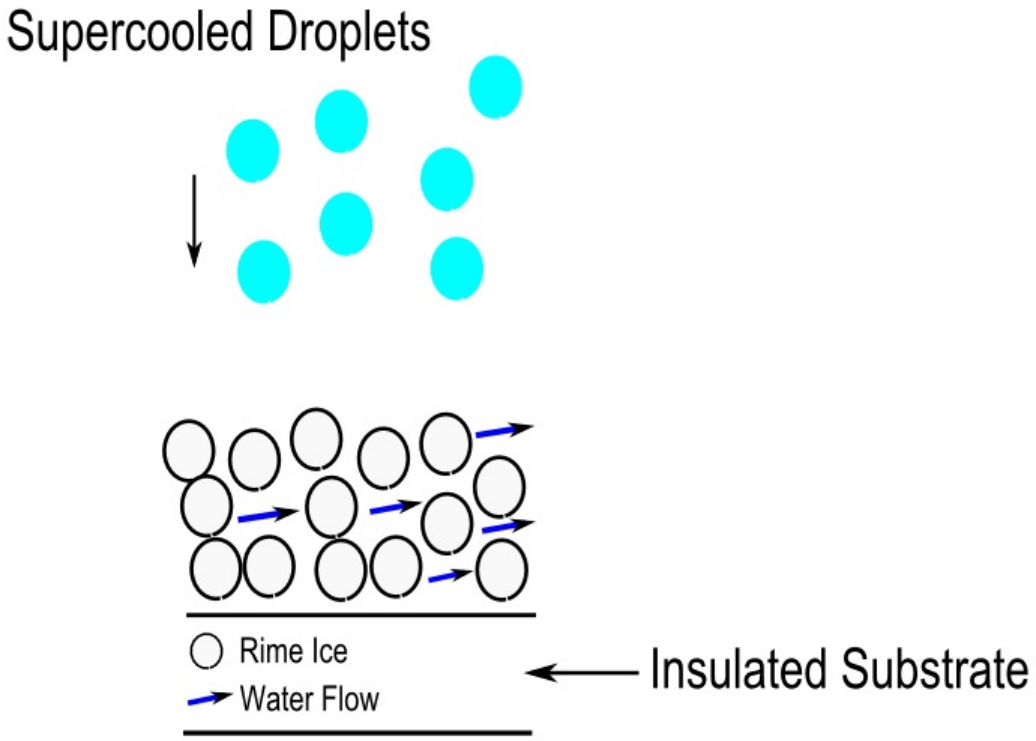


Figure 6.2: Schematic of non-dimensional ice accretion with no glaze formation.

equation 6.17 for $\tilde{t}$, gives the characteristic time scale as

$$\tilde{t} = \frac{\phi_i \rho_i \tilde{r}}{\lambda \dot{M}}. \tag{6.18}$$

Taking $\frac{R}{\tilde{R}} = R^*$ and $\frac{x}{U_s \tau} = R^*$ in equation 6.16, we get

$$\frac{\tilde{R}}{\tilde{t}} \frac{\partial R^*}{\partial t^*} + \frac{\tilde{R}}{\tau} \frac{\partial R^*}{\partial x^*} = \frac{(1-\lambda)\dot{M}}{(1-\phi_i)\rho_w}, \tag{6.19}$$

where τ is the time scale of the flow of water through the porous media. Rearranging equation 6.19,

$$\frac{\partial R^*}{\partial t^*} + \varepsilon \frac{\partial R^*}{\partial x^*} = \frac{(1-\lambda)\dot{M}\tilde{t}}{(1-\phi_i)\rho_w \tilde{R}}, \tag{6.20}$$

where $\varepsilon = \frac{\tilde{t}}{\tau} = \frac{\phi_i \rho_i \tilde{r}}{\lambda \dot{M} \tau}$ is ratio of the vertical growth timescale to the horizontal flow timescale. In the RHS, we substitute $\tilde{t}$ from equation 6.18 to get

$$\frac{\partial R^*}{\partial t^*} + \varepsilon \frac{\partial R^*}{\partial x^*} = \frac{(1-\lambda)\phi_i \rho_i}{(1-\phi_i)\rho_w \lambda \tilde{\alpha}}, \tag{6.21}$$

where $\tilde{\alpha} = \frac{\tilde{R}}{\tilde{r}}$ is the dimensionless saturation level of the porous matrix. The RHS can be simplified as a dimensionless number $\mathcal{Z}$ given as

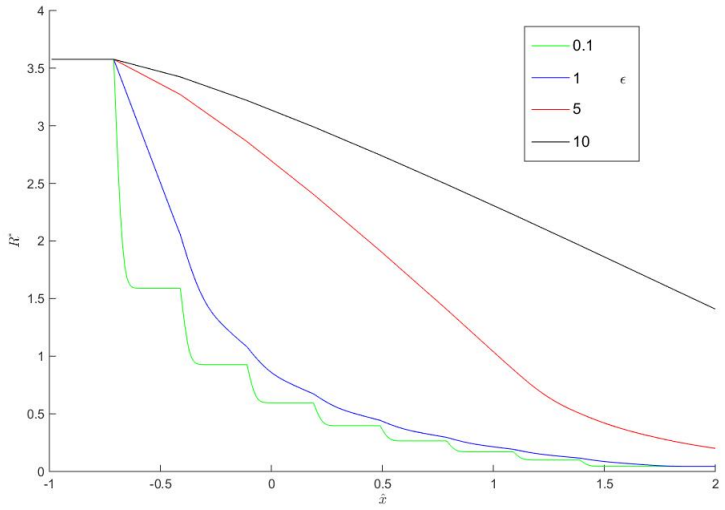


Figure 6.3: Non-dimensional saturation flux R^* for different values of time scale ratio ε.

$$\mathcal{Z} = \frac{(1-\lambda)\phi_i\rho_i}{\lambda(1-\phi_i)\rho_i\tilde{\alpha}}. \tag{6.22}$$

$\mathcal{Z}$ represents the balance of water flow through the porous matrix compared with the pore space available for the flow. In pure ratio terms, saturation flux is higher when freezing fraction is lower, packing fraction is higher, density of the solid is greater than the density of the liquid; and lower saturation levels are noted.

Figure 6.3 shows the variation in non-dimensional saturation flux R^* for different values of ε at 90 s. In this instance, ϕ_i and $\tilde{\alpha}$ are kept constant at

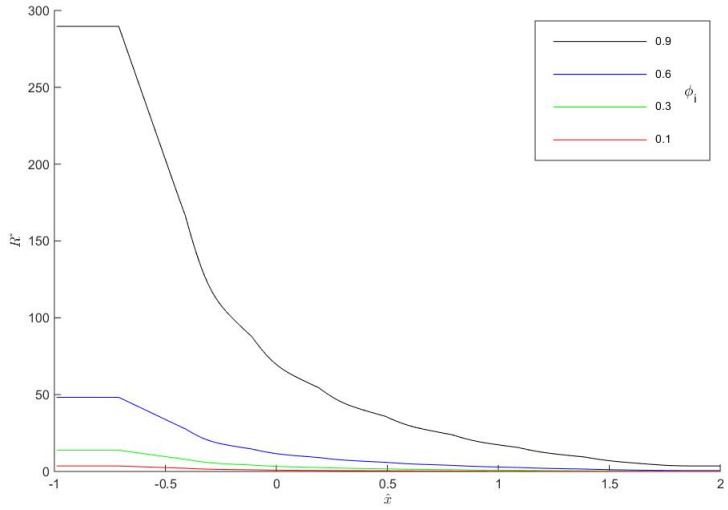


Figure 6.4: Non-dimensional saturation flux R^* for different values of ϕ_i.

0.1 and 1 respectively. λ is varied in steps from 0.1 to 0.9 across the domain $\tilde{x}$. From the figure, we can clearly see the effect of the convective term $\frac{\partial R^*}{\partial x^*}$ on the two-dimensional profile. When $\varepsilon = 0.1$ and flow is minimum, the profile takes the shape of the distributed impact. As ε increases, the profile spreads out due to the increasing impact of the convective term. The time scale ratio ε is thus a key term in this scenario.

Figure 6.4 shows the variation in R^* with respect to change in ϕ_i at 90 s. ε and $\tilde{\alpha}$ are both kept constant at a value of 1 for all four cases. From the figure, we note that a nine-fold increase in the value of ϕ_i from 0.1 to 0.9, results in a seventy-fold increase in the value of R^* at $\tilde{x} = 0$.

This is understandable since when ϕ_i is very large, the void space is much less and the flow for a fixed quantity is concentrated in a reduced space. Another interesting observation to note is that since $\varepsilon = 1$, the vertical growth and horizontal propagation of R^* are equal. The result of this is further downstream, despite differences in the packing fraction, R^* converges as the flow proceeds downstream. At higher values of ε, this convergence will occur further upstream; whereas at lower values of ε, this convergence will occur further downstream.

Inclusion of Freezing from Substrate Upwards

When including glaze ice accretion from the substrate upwards, we need to adapt equation 6.9 and follow a similar procedure of non-dimensionalisation to the previous section. The governing equation becomes

$$\frac{\partial R^*}{\partial t^*} + \varepsilon \frac{\partial R^*}{\partial x^*} = \mathcal{Z} - \frac{k_i(T_f - T_s)\tilde{t}}{L_f b \rho_w (1-\phi_i)\lambda \dot{M} \tilde{R}}. \tag{6.23}$$

Substituting for $\tilde{t}$ (equation 6.18), we get

$$\frac{\partial R^*}{\partial t^*} + \varepsilon \frac{\partial R^*}{\partial x^*} = \mathcal{Z} - \mathcal{J}, \tag{6.24}$$

where $\mathcal{J}$ is a non-dimensional number representing the ratio of conduction of latent heat through previously deposited glaze layer to the freezing of droplets. It is explicitly given as:

$$\mathcal{J} = \frac{k_i(T_f - T_s)\phi_i\rho_i}{L_f b\rho_w(1-\phi_i)\lambda\dot{M}\tilde{\alpha}} \tag{6.25}$$

The RHS in equation 6.24 must be positive to solve for saturation flux i.e. $\mathcal{Z} > \mathcal{J}$. Substituting for and rearranging the terms in this relation, gives

$$\frac{(1-\lambda)L_f\dot{M}b}{k_i(T_f - T_s)} > 1. \tag{6.26}$$

The LHS can be simplified to give a dimensionless number γ. This is an important relation involving values of freezing fraction, atmospheric temperature, collection efficiency, liquid water content and air speed; gives us the minimum height of the glaze ice above which we see the growth of a porous matrix above it with water flowing to give a saturation flux. It must be noted that in this instance, this is not a full solution considering b is taken constant, but an important first step towards determining the effect of other relevant atmospheric parameters on the two-dimensional spatial profile.

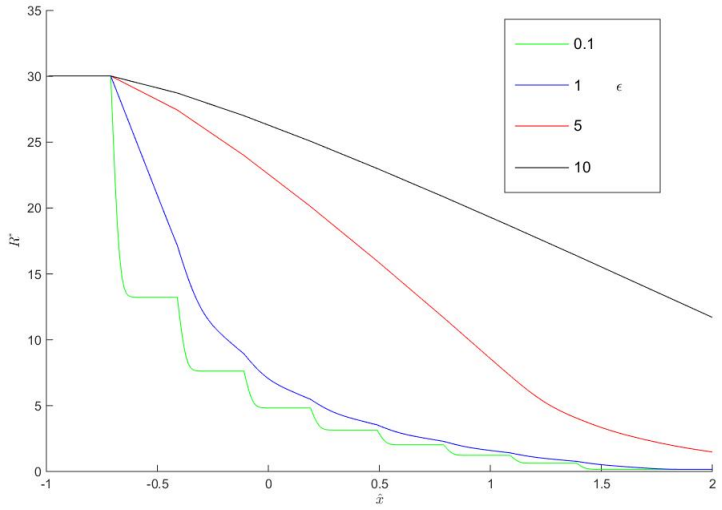


Figure 6.5: Non-dimensional saturation flux R^* for different values of ε. ϕ_i = 0.5, T_s = 268 K, b = 2 mm. λ is varied from 0.1 to 0.9 across $\tilde{x}$.

Evaluation of equation 6.23 is given for specimen cases; in the following figures, $\dot{M} = 0.27\,\mathrm{kg\,m^2 s^{-1}}$ and $\tilde{\alpha} = 1$. Figure 6.5 shows the variation in R^* for different values of ε. The results are similar to figure 6.3 with the inclusion of the condition that the RHS in equation 6.24 must be positive.

Figure 6.6 shows the variation in R^* with change in T_s; on keeping all other parameters fixed, the effect of substrate temperature is minimal. Generally, the substrate temperature will affect both the growth of the glaze ice and the freezing fraction but since the saturation flux itself is isothermal at T_f, the change is understandably minor.

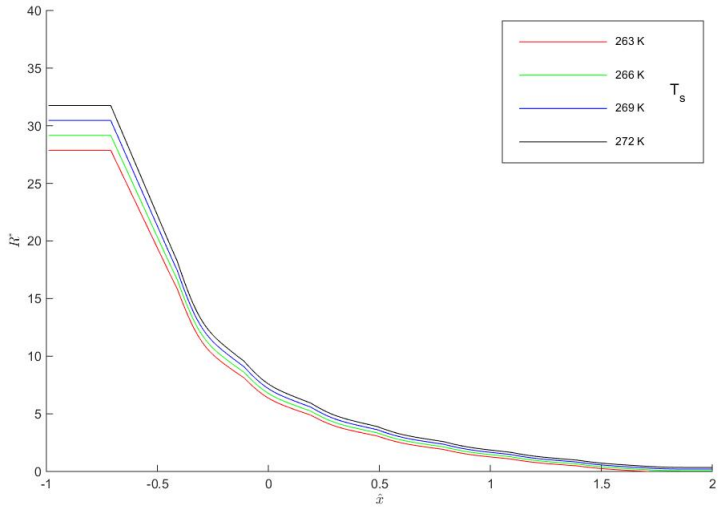


Figure 6.6: Non-dimensional saturation flux R^* for different values of T_s. ϕ_i = 0.5, $\varepsilon = 1$, $b = 2\,\text{mm}$. λ is varied from 0.1 to 0.9 across $\tilde{x}$.

Figure 6.7 shows the change in R^* with b. We note that while all other parameters are kept constant, changing the ice height does not significantly affect the non-dimensional saturation flux. This is because the effect of b is significant only at much smaller values of it; when $\mathcal{J}$ is closer to $\mathcal{Z}$. At such high values, $\mathcal{J}$ is insignificant to affect the saturation flux. Hence at longer accretion periods and greater glaze heights, the effect will be negligible.

Based on the relation in equation 6.26, we can determine minimum glaze heights for the presence of saturation flux and the formation of a porous

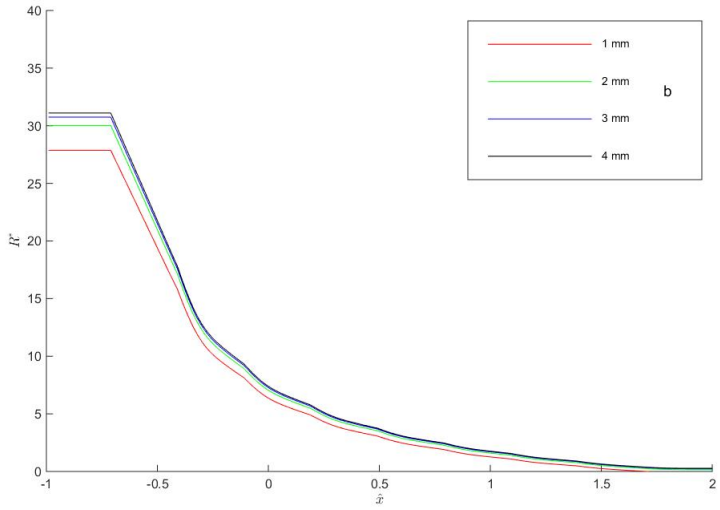


Figure 6.7: Non-dimensional saturation flux R^* for different values of b. ϕ_i = 0.5, $\varepsilon = 1$, $T_s = 268\,\mathrm{K}$. λ is varied from 0.1 to 0.9 across $\tilde{x}$.

rime layer with water flowing through it for different conditions.

Figure 6.8 shows the non-dimensional number γ for different values of b. We can see that as the substrate temperature decreases, the minimum glaze height required for the presence of saturation flux increases. This is because the growth rate of glaze ice is higher at lower temperatures and anticipated beyond a certain value is water left over to flow through the porous matrix.

Figure 6.9 shows the variation in γ versus b for different values of freezing fraction. Results show that at a fixed substrate temperature,

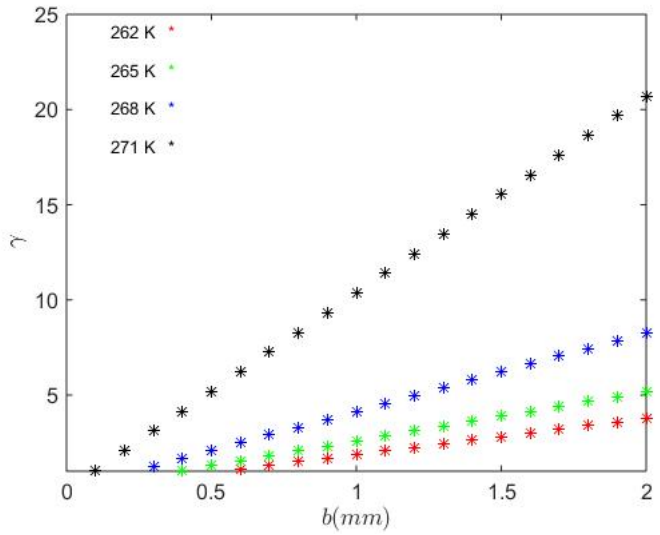


Figure 6.8: Non-dimensional number γ for different values of b. $\lambda = 0.5$, $\dot{M}$ $= 0.27\,\mathrm{kg\,m^{-2}\ s^{-1}}$.

saturation flux beings to exist for lower values of glaze ice at lower values of freezing fraction. This arises because at higher values of freezing fraction, the proportion of unfrozen droplet flux is lower and a greater amount is removed to form glaze ice. Hence it takes a longer time and subsequent glaze height, for left over water to exist and saturation flux to form.

6.3.2 Ice Accretion under Different Scenarios

There are several scenarios to consider when solving for the two dimensional profile of ice accretion on an aerofoil (Section 6.2.1). We use the values in

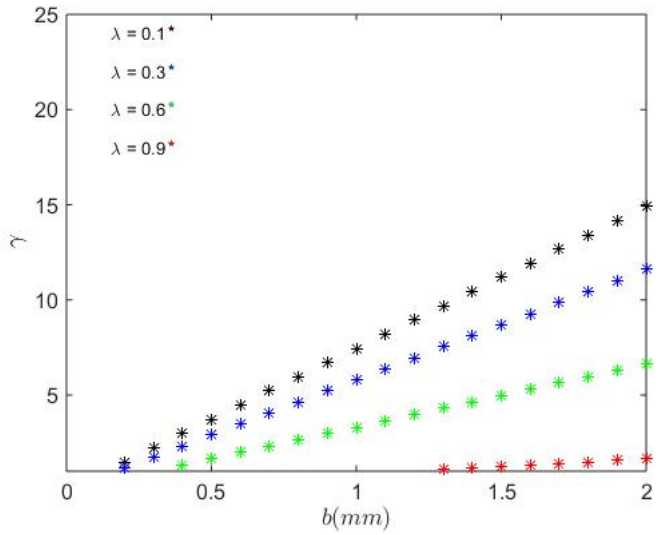


Figure 6.9: The latent heat-conduction ratio γ for different values of b. $T_s = 268\,\mathrm{K}$, $\dot{M} = 0.27\,\mathrm{kg\,m^{-2}\,s^{-1}}$.

the nomenclature and an initial secondary mixed ice height of 1 mm but vary collection efficiency β with $\tilde{x}$. $\rho_a = 0.003\,\mathrm{kg\,m^{-3}}$, $U_\infty = 90\,\mathrm{m\,s^{-1}}$ and AoA $= 0°$.

During ascent through clouds, we can envisage a scenario where β continuously decreases across the space co-ordinate from 0.9 to 0.5. Figure 6.10 shows us the two-dimensional profile of the ice height at 90 s. It is interesting to note that although downstream, the rime height is consistent; we note that a greater accumulation of water occurs in this region due to the shear effect of overlying wind speed pushing the flow through the rime

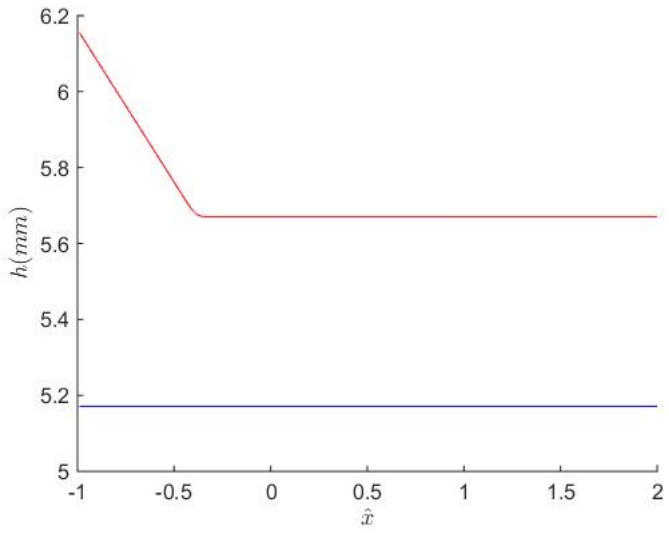


Figure 6.10: Two-dimensional ice height and profile at 90 s, $T_s = 266\,\mathrm{K}$ and $\phi_i = 0.49$. Red line represents rime ice and blue line represents glaze ice.

layer downstream. This is represented by figure 6.11 showing that the liquid fraction and saturation parameter increase downstream for the conditions in figure 6.10. It must be noted here that initially, the dual freezing mechanism causes no water to be left over and it is only at latter accretion times that such a formation develops. The profile is invalid for an instance when α is 0.

During descent through a cloud structure, we can envisage a scenario where β increases from 0.5 to 0.9 over $\tilde{x}$. Figure 6.12 shows the two-dimensional ice profile during cloud descent. In this situation, we confirm from figure 6.13 that saturation levels are higher upstream and lower down-

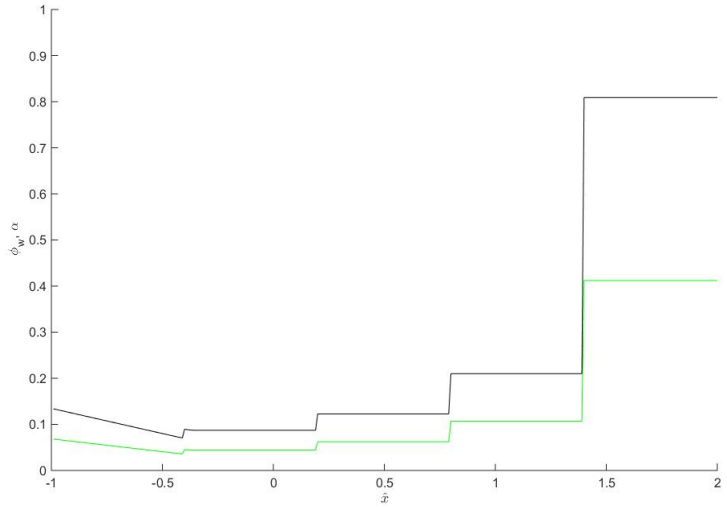


Figure 6.11: Two-dimensional profile of ϕ_w and α at 90 s, $T_s = 266$ K and $\phi_i = 0.49$. Green line represents ϕ_w and black line represents saturation level α.

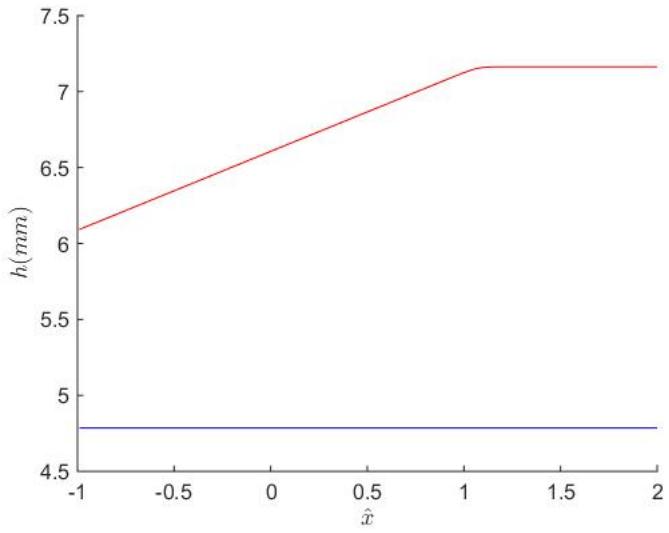


Figure 6.12: Two-dimensional ice height and profile at 90 s, $T_s = 266\,\mathrm{K}$ and $\phi_i = 0.38$. Red line represents rime ice and blue line represents glaze ice.

stream due to the droplet distribution pattern.

A further scenario to consider is within a formation of clouds such that droplet impact is divided equally with $\beta = 1$ and $\beta = 0.5$ over $\tilde{x}$. Figure 6.14 shows the two-dimensional ice profile when we have a large droplet impact and a lesser droplet impact over a length. In comparison to figure 6.10, results show that the slope of the height extends further downstream to emphasise the droplet pattern. The saturation levels shown in figure 6.15 also exhibit greater levels in the region of consistent height.

It is apparent from this section that a model such as this may not

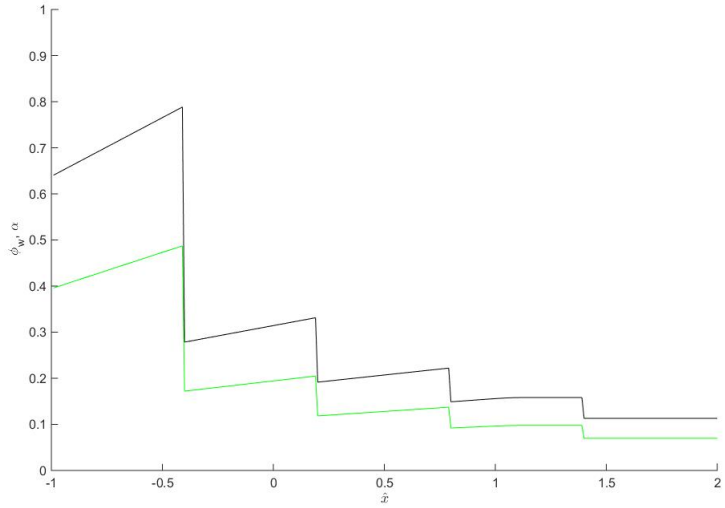


Figure 6.13: Two-dimensional profile of ϕ_w and α at 90 s, $T_s = 266$ K and $\phi_i = 0.38$. Green line represents ϕ_w and black line represents saturation level α.

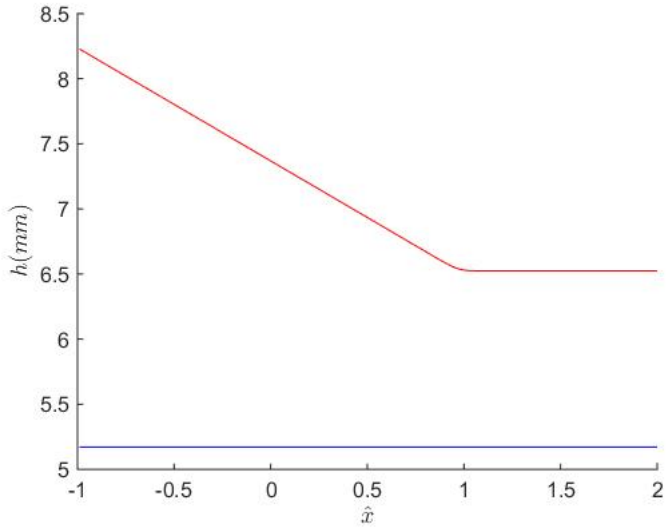


Figure 6.14: Two-dimensional ice height and profile at 90 s, $T_s = 266\,\mathrm{K}$ and $\phi_i = 0.49$. Red line represents rime ice and blue line represents glaze ice.

be present at all atmospheric conditions. Generally higher quantities of supercooled droplet flux, lower atmospheric temperatures and lower packing fractions favour this process.

6.3.3 Effect of Runback Water

In this section, we want to determine the effect of runback water on the accretion profile and saturation level. Three different scenarios are considered where the electro-thermal mats are working to full capacity (equation 6.12) and we have a runback water flux of $0.039\,\mathrm{kg\,m^{-2}s^{-1}}$; electro-thermal

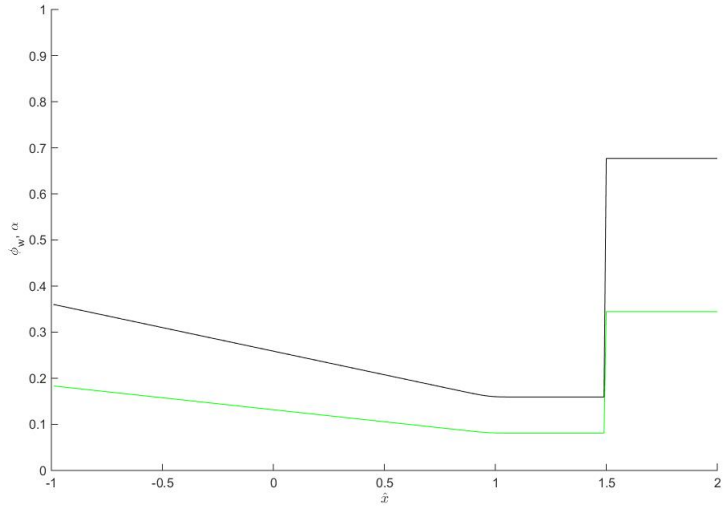


Figure 6.15: Two-dimensional profile of ϕ_i and α at 90 s, $T_s = 266$ K and $\phi_i = 0.49$. Green line represents ϕ_w and black line represents saturation level α.

mats working to 75% capacity i.e. $0.029\,\mathrm{kg\,m^{-2}s^{-1}}$; and 50% capacity i.e. $0.02\,\mathrm{kg\,m^{-2}s^{-1}}$. For comparison, the same conditions as the case of ascent through the clouds in figure 6.10 is maintained.

Figure 6.16 and 6.17 exhibit the plots of ice height and liquid fraction/saturation level for different efficiencies of the electro-thermal mats. From both the figures, it is apparent that under realistic values, the effect of the runback water is minimal in such a system where the flow inside the porous matrix is primarily driven by the overlying wind shear. This is also compounded by the fact that the quantity of runback water is much less as compared to the supercooled droplet impact. In the situation where these two values are closer in magnitude; which may include glaze ice formation; the effect may be amplified.

6.4 Conclusion

First order solutions to a two-dimensional code have been formed for a particular situation where a porous rime matrix growing above a glaze ice layer; and contains water flow due to the overlying wind shear.

In the non-dimensional situation of no glaze ice formation, the effect

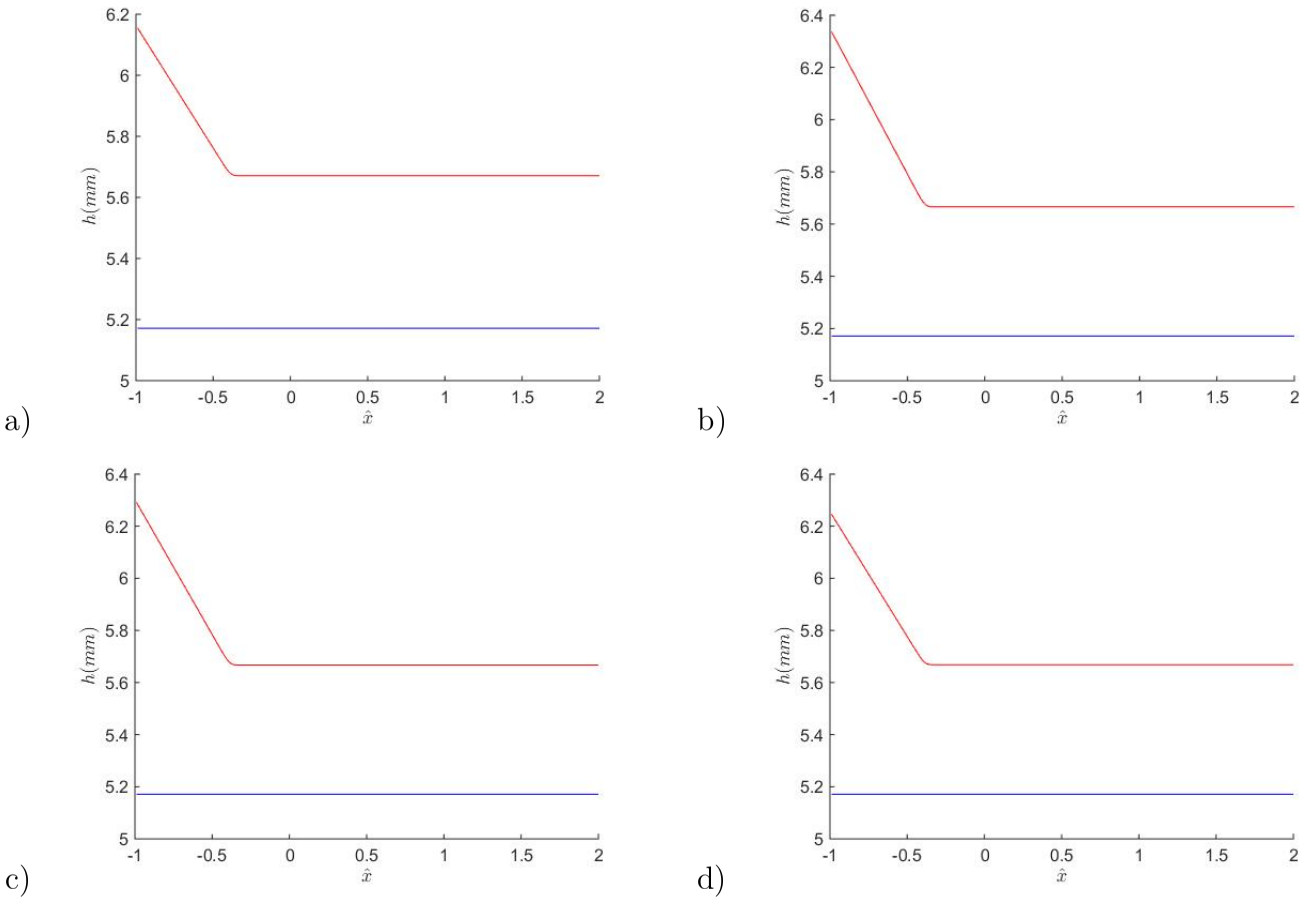


Figure 6.16: Two-dimensional ice profiles for a) No runback flux; b) 100% electro-thermal mat efficiency; c) 75% electro-thermal mat efficiency; and d) 50% electro-thermal mat efficiency.

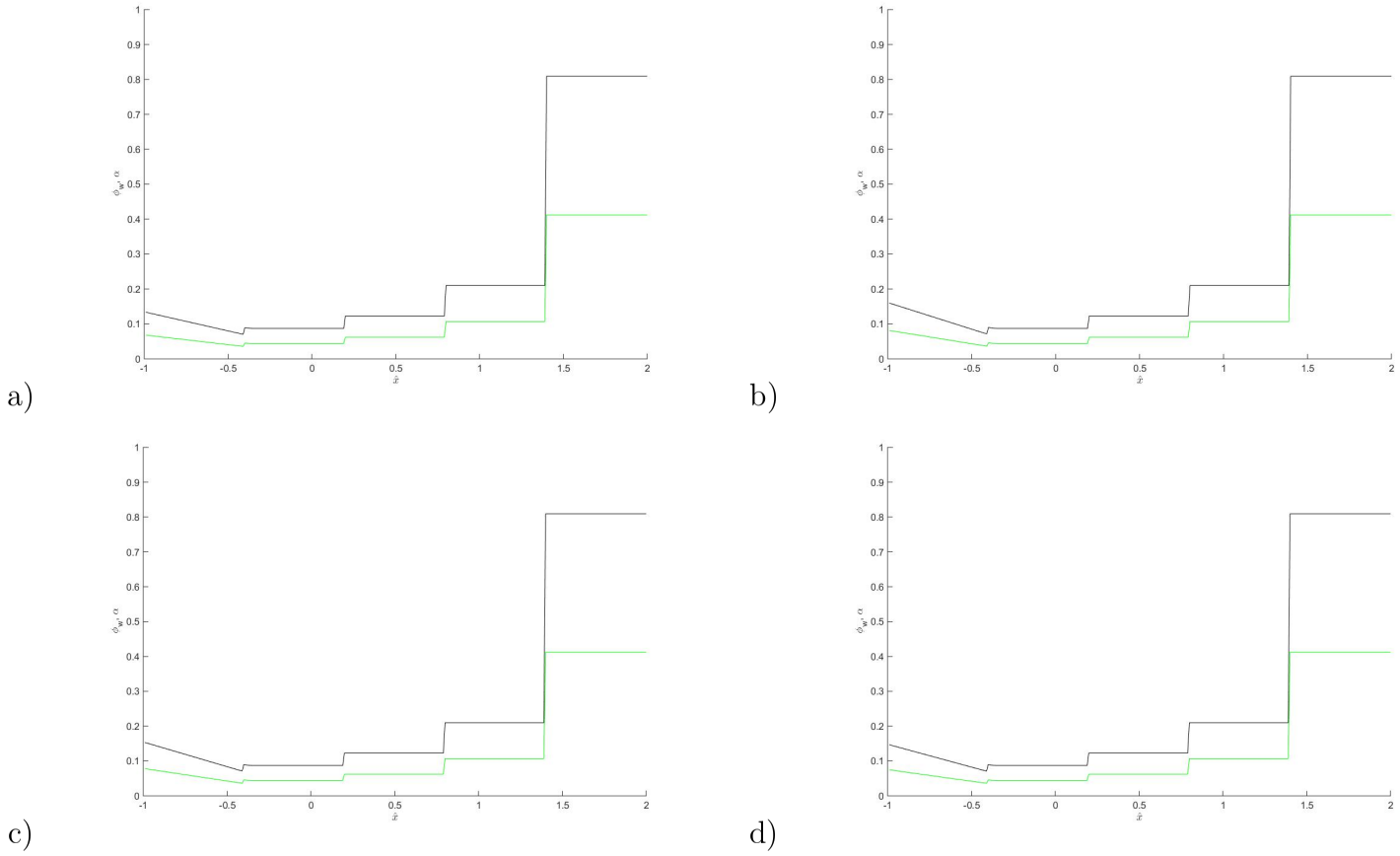


Figure 6.17: Two-dimensional saturation levels and liquid fraction profiles for a) No runback flux; b) 100% electro-thermal mat efficiency; c) 75% electro-thermal mat efficiency; and d) 50% electro-thermal mat efficiency.

of the convective term was studied due to a scaled time ratio ε and changes in ϕ_i. It was found that larger values of ε result in a smooth profile instead of a profile typically reflective of droplet impact; and increase in ϕ_i, increases the saturation flux as the porous space reduces. When considering the case of glaze ice formation, the effect of temperature and ice height is minimal on the non-dimensional saturation flux. A relation was developed to determine the minimum glaze height b beyond which the profile in question is present for different atmospheric conditions.

The dimensional ice profile yielded results for specimen scenarios such as ascent/descent through clouds; and different combinations of vertical and horizontal cloud structures. Even if the two-dimensional profile appears similar, the saturation level and liquid fraction differ greatly based on the pattern of droplet impact and convective effect of flow through the porous matrix. Lower atmospheric temperature, lower packing fraction and higher incoming droplet flux favour mixed ice accretion in this particular structure.

Chapter 7

Conclusion

An experimental and computational investigation into the formation of ice on aerofoils has been conducted. The research elucidates several new findings and confirms results from past research as well.

Looking back at the objectives of the PhD. (Chapter 1), there are several points to note:

1. An experimental setup to test the adhesion strength of ice was designed and tested for repeatability. The spinning centrifuge apparatus determined the repeatability to be 9.69–14.96% for a series of different substrates and temperature conditions. Tests were also conducted on three different substrates: SS 304, Al 6082-T651 and Al 1050A-H14 to determine the effect of

preparation and ambient temperature on the adhesion strength. Regarding the identification of key ice adhesion properties, freezing and ambient temperature were identified and the reasoning was linked to the presence of an amorphous liquid-like layer at the ice-substrate interface [63].

2. Adhesion tests were performed on 14 icephobic coatings manufactured using silica and carbon nanotube particles. Tests were repeated daily for a number of cycles (10–17) and contact angle parameters were measured before ice was grown on the coatings. It was found that the surface should possess high receding contact angle and low contact angle hysteresis to reduce adhesion to reduce ice-substrate contact points. Hydrophobicity and icephobicity may not necessarily be characteristics of a surface unless the aforementioned criteria is satisfied. Adhesion strength was found to decrease above CAH equal to 92° because air begins to occupy the increased spaces in the ice-substrate contact points and low adhesion strengths were already measured at CAH $\simeq 25°$. Anti-icing tests were also performed by measuring the freezing time of a droplet incident on the icephobic coatings resting on a cold plate. The key parameter delaying freezing time was the static contact angle because it determines the amount of surface area of a droplet in contact with a coating. The advancing contact angle had a slightly reduced effect but no correlation was found with the receding contact angle and CAH.

3. We introduced a one-dimensional accretion model to determine the accre-

tion of mixed ice in addition to rime and glaze; on a flat plate representing an aircraft wing. Accretion occurred in four distinct stages and the effect of atmospheric parameters on the transition time through stages and ice height was studied. Our model predicts lower glaze ice heights than existing models at lower temperatures. Lower temperatures favour higher ice growth and increasing the packing fraction corresponds to lower ice height and glaze icing regime. Thus, numerical investigation into the formation of ice on aerofoils was conducted by developing a theory for the formation of mixed ice in a one and two dimensional scenario. A new parameter λ was introduced to determine the fraction of a droplet that freezes on impact with a surface on an aerofoil.

4. Continuing with the numerical investigation, a two-dimensional model was studied for the particular condition of rime growing above glaze with water flowing through the porous rime matrix. The equations were non-dimensionalised to determine the effect of the convective flow, packing fraction, atmospheric temperature and glaze height on the profile. The first two had a profound impact in comparison to the latter two. Dimensional values of ice height were determined for different conditions including ascent/descent through clouds to visualise the profile.

In totality, it is fair to say that the objectives of the project were achieved. Several avenues of future research are detailed in the following chapter.

Chapter 8

Future Work

Building upon the work conducted in this research, there exist several avenues for future research in this specific field.

With regards to Chapter 2, in the future, it will be interesting to repeat these adhesion tests on different conducting substrates to expand on this theory; as well as performing adhesion tests on insulating substrates to determine the effect of temperature on adhesion strength. We can also vary the beam temperature and increase the settling time between the change of temperature and note if any, an effect on the adhesion strength value obtained.

With regards to Chapter 3, in the future, it will be interesting to

test such coatings in a dynamic environment to determine their effectiveness in preventing the formation of runback icing. These tests can be conducted in an icing tunnel where measurements can be recorded of the delay time and distance for ice accretion in relation to an uncoated surface.

With regards to Chapter 4, in the future, it will be useful to test the freezing time with an infra-red camera to determine the temperature change in the droplet. This will also enable a better comparison with the literature and the differentiation of freezing into the four defined stages.

With regards to Chapter 5, in the future, it will be useful to expand the model to include the effect of droplet size etc. on the dimensionless freezing fraction parameter and subsequently the packing fraction ϕ. Eventually, a relation such as the Macklin number [92] can be developed to determine λ and ϕ for higher speed collisions. Experimental procedures examining the impact of supercooled droplets on pre-formed rime with varying diameters can also provide an insight into the actual icing process compared with the model.

With regards to Chapter 6, in the future, the model can be expanded to the situation of supercooled droplets directly impacting a water film instead of rime. It can also be expanded to a three-dimensional model.

Appendix A

Table A.1: Summary of results for coating A from test period. MF stands for mould failure. PD stands for partial detachment.

Cycle	**SCA(°)**	**ACA(°)**	**RCA(°)**	**CAH(°)**	**DS (rpm)**	**AS (kPa)**	**ARF**
1	101.98 ± 1.96	110.67 ± 1.03	82.94 ± 4.86	27.73 ± 4.97	1020	8.96 ± 1.18	17
2	100.46 ± 0.19	113.34 ± 1.19	78.8 ± 4.4	34.54 ± 4.56	MF	-	-
3	104.09 ± 0.21	109.17 ± 2.30	73.95 ± 0.73	35.22 ± 2.41	1335	15.34 ± 2.02	9.94
4	105.97 ± 1.13	114.90 ± 3.39	70.11 ± 4.79	44.79 ± 5.87	1650	23.44 ± 3.08	6.5
5	106.88 ± 1.71	112.29 ± 0.45	72.52 ± 1.09	39.76 ± 1.18	1785	27.43 ± 3.61	5.55
6	108.00 ± 2.04	116.54 ± 2.55	70.01 ± 5.04	46.52 ± 5.65	1635	23.01 ± 3.03	6.62
7	107.34 ± 0.35	115.80 ± 0.52	62.14 ± 5.14	53.67 ± 5.16	2370	48.35 ± 6.36	3.15
8	111.45 ± 3.28	115.29 ± 0.88	58.63 ± 10.84	56.65 ± 10.88	MF	-	-
9	108.59 ± 1.82	116.18 ± 0.64	63.88 ± 7.48	52.29 ± 7.51	2340	50.83 ± 6.69	2.99
10	107.03 ± 2.84	115.48 ± 1.57	67.08 ± 3.59	48.39 ± 3.92	2295	45.34 ± 5.97	3.36
11	106.97 ± 3.92	113.48 ± 3.55	62.08 ± 3.58	51.4 ± 5.04	2205	41.85 ± 5.51	3.64
12	109.71 ± 2.01	117.9 ± 0.91	66.84 ± 5.86	51.06 ± 5.93	PD	-	-
13	105.37 ± 1.23	113.96 ± 2.34	56.9 ± 4.73	57.06 ± 5.28	2610	58.64 ± 7.72	2.6
14	107.96 ± 3.52	115.74 ± 1.67	49.68 ± 3.74	66.06 ± 4.1	2955	75.16 ± 9.89	2.02
15	103.59 ± 5.73	112.67 ± 4.82	41.61 ± 6.77	71.06 ± 8.31	3555	108.79 ± 14.31	1.4
16	104.27 ± 4.82	116.43 ± 1.84	43.37 ± 2.94	73.06 ± 3.47	3645	114.37 ± 15.05	1.33
17	106.82 ± 3.3	121 ± 0.99	47.75 ± 8.04	73.25 ± 8.1	3990	137.04 ± 18.03	1.11

Table A.2: Summary of results for coating B from test period. MF stands for mould failure. PD stands for partial detachment.

Cycle	**SCA(°)**	**ACA(°)**	**RCA(°)**	**CAH(°)**	**DS (rpm)**	**AS (kPa)**	**ARF**
1	100.36 ± 3.15	108.84 ± 0.72	82.65 ± 5.57	26.18 ± 5.62	930	7.44 ± 0.98	20.49
2	98.63 ± 2.12	111.73 ± 0.77	78.46 ± 1.00	33.27 ± 1.33	1005	8.69 ± 1.14	17.54
3	102.70 ± 0.64	111.38 ± 2.83	77.61 ± 0.675	33.77 ± 2.91	MF	-	-
4	103.35 ± 1.80	109.2 ± 2.11	68.76 ± 2.02	40.43 ± 2.92	1665	23.86 ± 3.14	6.39
5	104.00 ± 0.28	113.91 ± 1.40	71.67 ± 3.49	42.24 ± 3.76	MF	-	-
6	106.42 ± 0.95	114.09 ± 1.25	70.24 ± 3.94	43.85 ± 4.13	1815	28.36 ± 3.73	5.37
7	106.16 ± 0.92	112.86 ± 1.88	73.38 ± 3.33	39.48 ± 3.82	MF	-	-
8	108.15 ± 0.84	113.91 ± 2.21	60.39 ± 3.49	53.52 ± 4.13	2200	41.66 ± 5.48	3.65
9	112.7 ± 2.45	112.32 ± 0.62	58.10 ± 2.73	54.22 ± 2.8	2595	57.96 ± 7.63	2.63
10	109.33 ± 3.32	115.79 ± 8.63	65.04 ± 1.79	50.75 ± 8.81	PD	-	-
11	105.46 ± 3.32	117.79 ± 4.54	63.04 ± 3.61	54.75 ± 5.8	MF	-	-
12	108.77 ± 0.23	115.27 ± 0.56	60.24 ± 8.42	55.02 ± 8.44	2235	43 ± 5.66	3.55
13	105.38 ± 1.31	113.73 ± 2.54	48.78 ± 1.94	64.95 ± 3.2	3255	91.2 ± 12	1.67
14	109.53 ± 2.73	115.27 ± 3.16	47.33 ± 1.21	67.94 ± 3.38	PD	-	-
15	106.53 ± 2.63	114.51 ± 0.94	45.14 ± 3.74	69.37 ± 3.86	PD	-	-
16	105.72 ± 2.31	112.42 ± 3.88	41.4 ± 1.12	71.02 ± 4.04	3960	134.92 ± 17.75	1.13
17	107.39 ± 1.17	118.34 ± 0.19	50.99 ± 4.53	67.35 ± 4.54	MF	-	-

Table A.3: Summary of results for coating C from test period. MF stands for mould failure. PD stands for partial detachment.

Cycle	**SCA(°)**	**ACA(°)**	**RCA(°)**	**CAH(°)**	**DS (rpm)**	**AS (kPa)**	**ARF**
1	130.48 ± 3.84	132.66 ± 5.66	87.87 ± 4.75	44.79 ± 7.39	1650	23.43 ± 3.08	6.5
2	115.35 ± 4.87	123.68 ± 1.20	79.18 ± 1.18	44.5 ± 1.68	MF	-	-
3	106.06 ± 3.13	114.68 ± 2.44	71.06 ± 4.66	43.62 ± 5.26	1845	29.30 ± 3.85	5.2
4	114.62 ± 2.09	117.76 ± 0.917	60.69 ± 5.06	57.07 ± 5.14	2505	54.02 ± 7.11	2.82
5	116.01 ± 1.29	119.81 ± 2.52	58.18 ± 3.46	61.64 ± 4.28	PD	-	-
6	114.65 ± 1.96	117.16 ± 0.48	59.58 ± 8.62	57.57 ± 8.63	2250	43.57 ± 5.73	3.49
7	113.12 ± 2.23	117.87 ± 0.68	51.86 ± 5.76	66.01 ± 5.8	PD	-	-
8	112.21 ± 2.29	118.25 ± 1.12	54.37 ± 7.32	63.88 ± 7.41	2520	54.66 ± 7.19	2.78
9	110.99 ± 1.08	123.05 ± 1.02	60.70 ± 6.79	62.35 ± 6.86	3240	90.36 ± 11.89	1.68
10	112.62 ± 2.90	119.74 ± 0.17	46.92 ± 2.88	72.81 ± 2.89	3765	122.02 ± 16.06	1.25
11	109.51 ± 1.27	115.32 ± 2.32	46.56 ± 1.48	68.76 ± 2.75	MF	-	-
12	110.34 ± 1.99	117.82 ± 0.62	45.98 ± 5.28	71.84 ± 5.32	PD	-	-
13	111.57 ± 2.91	118.24 ± 1.62	48.09 ± 3.54	70.15 ± 3.89	3405	99.8 ± 13.13	1.53
14	115.92 ± 3.36	119.41 ± 4.17	46.7 ± 1.63	72.71 ± 4.47	PD	-	-
15	112.58 ± 1.71	114.69 ± 3.53	40.15 ± 2.51	74.54 ± 4.33	PD	-	-
16	114.78 ± 2.94	117.42 ± 2.75	41.58 ± 3.96	75.84 ± 4.82	MF	-	-
17	111.62 ± 3.42	118.16 ± 1.52	43.53 ± 4.44	74.59 ± 4.69	3900	131.44 ± 17.3	1.16

Table A.4: Summary of results for coating D from test period. MF stands for mould failure. PD stands for partial detachment.

Cycle	**SCA(°)**	**ACA(°)**	**RCA(°)**	**CAH(°)**	**DS (rpm)**	**AS (kPa)**	**ARF**
1	135.12 ± 1.71	137.22 ± 3.41	92.43 ± 5.35	44.17 ± 6.34	1380	16.39 ± 2.16	9.3
2	124.47 ± 7.39	133.41 ± 3.82	91.9 ± 3.22	41.52 ± 5	1395	16.75 ± 2.2	9.1
3	112.88 ± 3.15	114.09 ± 0.37	73.23 ± 3.35	40.86 ± 3.37	MF	-	-
4	115.18 ± 1.36	117.47 ± 1.57	75.10 ± 5.23	42.37 ± 5.46	1770	26.97 ± 3.55	5.65
5	111.86 ± 1.96	112.52 ± 1.69	68.18 ± 3.46	44.33 ± 3.85	PD	-	-
6	116.46 ± 6.70	117.99 ± 0.77	60.37 ± 2.73	57.62 ± 2.84	2295	45.34 ± 5.97	3.36
7	112.10 ± 2.02	119.78 ± 2.66	66.42 ± 1.22	53.36 ± 2.93	2400	49.58 ± 6.52	3.07
8	111.30 ± 1.42	119.52 ± 0.66	63.21 ± 6.54	56.31 ± 6.57	2820	68.45 ± 9	2.23
9	111.73 ± 3.5	124.97 ± 0.86	58.62 ± 6.08	66.35 ± 6.14	3090	81.97 ± 10.79	1.86
10	112.51 ± 2.31	122.13 ± 1.43	52.62 ± 1.15	69.51 ± 1.84	MF	-	-
11	110.63 ± 1.84	119.56 ± 2.53	47.87 ± 2.28	71.69 ± 3.41	MF	-	-
12	110.75 ± 1.28	117.40 ± 1.16	47.93 ± 2.16	69.57 ± 2.45	MF	-	-
13	111.23 ± 2.09	119.48 ± 2.84	44.85 ± 1.64	74.63 ± 3.28	3885	129.92 ± 17.09	1.17
14	113.36 ± 3.26	117.35 ± 2.71	42.62 ± 4.72	74.73 ± 5.44	3870	128.92 ± 16.96	1.18
15	110.54 ± 2.74	117.40 ± 3.02	41.87 ± 1.83	75.53 ± 3.53	MF	-	-
16	108.39 ± 1.74	119.40 ± 2.64	43.83 ± 3.26	75.57 ± 4.19	PD	-	-
17	107.64 ± 2.01	117.61 ± 1.28	41.68 ± 6.61	75.93 ± 6.73	MF	-	-

Table A.5: Summary of results for coating E from test period. MF stands for mould failure. PD stands for partial detachment. ND stands for no detachment at maximum speed of 4500 rpm.

Test Number	**Detachment speed (rpm)**	**Shear stress (kPa)**	**ARF**
1	ND	-	-
2	ND	-	-
3	MF	-	-
4	ND	-	-
5	ND	-	-
6	4110	145.4 $\pm$ 19.1	1.05

Table A.6: Summary of results for coating F from test period. MF stands for mould failure. PD stands for partial detachment. ND stands for no detachment at maximum speed of 4500 rpm.

Test Number	**Detachment speed (rpm)**	**Shear stress (kPa)**	**ARF**
1	ND	-	-
2	ND	-	-
3	4095	144.4 ± 19	1.05
4	ND	-	-
5	ND	-	-
6	ND	-	-

Table A.7: Summary of results for coating G from test period. MF stands for mould failure. PD stands for partial detachment. ND stands for no detachment at maximum speed of 4500 rpm.

Test Number	**Detachment speed (rpm)**	**Shear stress (kPa)**	**ARF**
1	MF	-	-
2	2475	52.7 ± 6.9	2.9
3	PD	-	-
4	2535	55.3 ± 7.3	2.75
5	2985	76.7 ± 10	2
6	2865	70.7 ± 9.3	2.15

Table A.8: Summary of results for coating H from test period. MF stands for mould failure. PD stands for partial detachment.

Cycle	**SCA(°)**	**ACA(°)**	**RCA(°)**	**CAH(°)**	**DS (rpm)**	**AS (kPa)**	**ARF**
1	140.67 ± 2.65	143.56 ± 5.4	62.28 ± 4.15	81.27 ± 6.81	3945	133.97 ± 17.63	1.13
2	142.89 ± 7.93	144.57 ± 0.84	59.13 ± 4.62	85.44 ± 4.7	3930	132.95 ± 17.5	1.14
3	144.56 ± 1.62	147.58 ± 2.11	58.73 ± 3.65	88.86 ± 4.22	ND	-	-
4	141.99 ± 1.19	146.32 ± 0.66	63.25 ± 5.89	83.07 ± 5.93	4500	174.31 ± 22.9	0.87
5	140.65 ± 0.77	146.05 ± 2.12	56.13 ± 2.88	89.91 ± 3.58	ND	-	-
6	140.99 ± 2.52	145.38 ± 3.51	55.85 ± 3.44	89.53 ± 4.91	ND	-	-
7	140.07 ± 2.53	144.42 ± 0.85	56.1 ± 3.58	88.31 ± 3.68	ND	-	-
8	139.39 ± 2.41	141.93 ± 0.70	48.25 ± 7.75	93.74 ± 7.78	ND	-	-
9	133.1 ± 2.78	136.26 ± 4.14	40.89 ± 1.30	94.18 ± 4.34	ND	-	-
10	140.32 ± 3.61	140.94 ± 3.33	53.88 ± 4.59	87.05 ± 5.67	4500	174.31 ± 22.9	0.87

Table A.9: Summary of results for coating I from test period. MF stands for mould failure. PD stands for partial detachment.

Cycle	**SCA(°)**	**ACA(°)**	**RCA(°)**	**CAH(°)**	**DS (rpm)**	**AS (kPa)**	**ARF**
1	154.14 ± 1.63	157.81 ± 2.86	145.06 ± 4.38	12.75 ± 5.23	MF	-	-
2	153.39 ± 7.52	160.48 ± 5.55	129.64 ± 1.38	30.85 ± 5.72	1155	11.48 ± 1.51	13.2
3	157.63 ± 2.34	162.22 ± 3.83	129.38 ± 3.79	32.84 ± 5.39	MF	-	-
4	158.27 ± 3.92	159.00 ± 2.30	122.98 ± 5.13	36.02 ± 5.62	1680	24.3 ± 3.19	6.25
5	150.54 ± 1.77	160.65 ± 6.18	118.15 ± 3.3	42.5 ± 7	2175	40.72 ± 5.36	3.73
6	151.84 ± 10.85	155.45 ± 2.75	111.00 ± 1.37	44.45 ± 3.07	MF	-	-
7	145.80 ± 5.94	151.08 ± 6.11	104.16 ± 5.75	46.91 ± 8.39	2505	54.01 ± 7.1	2.81
8	138.36 ± 0.73	145.58 ± 1.03	87.53 ± 3.14	58.05 ± 3.3	PD	-	-
9	135.59 ± 0.43	140.04 ± 5.90	66.73 ± 6.22	73.30 ± 8.57	3105	82.99 ± 10.9	1.83
10	141.35 ± 3.55	136.42 ± 1.28	63.1 ± 3.68	73.32 ± 3.89	3405	99.80 ± 13.13	1.52

Table A.10: Summary of results for coating J from test period. MF stands for mould failure. PD stands for partial detachment.

Cycle	**SCA(°)**	**ACA(°)**	**RCA(°)**	**CAH(°)**	**DS (rpm)**	**AS (kPa)**	**ARF**
1	112.97 ± 3.15	133.94 ± 2.63	57.55 ± 2.90	76.39 ± 3.91	3375	98.05 ± 12.9	1.55
2	113.63 ± 1.53	132.93 ± 1.05	59.07 ± 4.77	73.86 ± 4.88	ND	-	-
3	110.25 ± 3.25	130.57 ± 2.08	59.79 ± 5.27	70.77 ± 5.67	ND	-	-
4	121.33 ± 4.19	131.59 ± 1.69	61.39 ± 7.66	70.19 ± 7.84	ND	-	-
5	118.22 ± 1.43	129.06 ± 2.37	59.48 ± 0.13	69.57 ± 2.38	ND	-	-
6	119.54 ± 1.30	130.26 ± 0.81	53.68 ± 3.79	76.58 ± 3.88	ND	-	-
7	118.49 ± 2.1	131.57 ± 1.91	54.03 ± 3.12	77.53 ± 3.66	4155	148.61 ± 19.55	1.02
8	118.36 ± 2.17	132.85 ± 2.73	52.83 ± 6.09	80.01 ± 6.67	ND	-	-
9	117.75 ± 6.59	130.05 ± 0.59	47.28 ± 9.3	82.76 ± 9.32	4320	160.65 ± 21.14	0.95
10	124.34 ± 3.24	134.82 ± 2.85	48.63 ± 3.24	86.19 ± 4.32	ND	-	-

Table A.11: Summary of results for coating K from test period. MF stands for mould failure. PD stands for partial detachment.

Cycle	**SCA(°)**	**ACA(°)**	**RCA(°)**	**CAH(°)**	**DS (rpm)**	**AS (kPa)**	**ARF**
1	108.2 ± 0.85	129.82 ± 2.94	49.32 ± 1.55	80.5 ± 3.32	4350	162.89 ± 21.43	0.93
2	107.49 ± 1.24	131.54 ± 0.95	44.37 ± 8.48	87.16 ± 8.53	4455	170.85 ± 22.48	0.89
3	108.25 ± 5.43	121.79 ± 0.71	41.51 ± 3.66	80.28 ± 3.73	4005	138.07 ± 18.17	1.1
4	111.84 ± 3.92	130.01 ± 2.01	40.44 ± 3.49	89.57 ± 4.03	MF	-	-
5	114.82 ± 3.16	123.76 ± 0.62	36.49 ± 2.26	87.27 ± 2.34	4080	143.29 ± 18.86	1.06
6	104.46 ± 4.18	123.58 ± 0.81	34.89 ± 2.08	88.69 ± 2.23	PD	-	-
7	103.71 ± 1.56	122.04 ± 0.75	32.47 ± 2.00	89.57 ± 2.14	4215	152.93 ± 20.12	1
8	109.08 ± 3.6	124.16 ± 0.87	34.91 ± 5.44	89.25 ± 5.51	MF	-	-
9	113.77 ± 2.05	123.03 ± 2.82	41.65 ± 4.53	81.38 ± 5.34	4245	155.12 ± 20.41	0.98
10	109.73 ± 2.73	117.81 ± 0.18	31.91 ± 1.29	85.9 ± 1.3	MF	-	-

Table A.12: Summary of results for coating L from test period. MF stands for mould failure. PD stands for partial detachment.

Cycle	**SCA(°)**	**ACA(°)**	**RCA(°)**	**CAH(°)**	**DS (rpm)**	**AS (kPa)**	**ARF**
1	110.86 ± 0.61	132.66 ± 1.43	34.18 ± 2.34	98.48 ± 2.74	ND	-	-
2	106.94 ± 1.2	136.64 ± 3.26	38.38 ± 8.67	98.26 ± 9.26	4140	147.54 ± 19.41	1.03
3	109.6 ± 1.03	138.67 ± 2.43	41.25 ± 4.53	97.42 ± 5.14	4500	174.31 ± 22.94	0.87
4	110.54 ± 2.64	137.19 ± 1.49	41.89 ± 0.78	95.3 ± 1.68	PD	-	-
5	112.37 ± 3.75	129.30 ± 3.49	42.94 ± 5.08	86.36 ± 6.16	ND	-	-
6	106.04 ± 0.65	126.78 ± 1.57	42.96 ± 4.3	83.82 ± 4.57	ND	-	-
7	110.03 ± 2.01	128.64 ± 1.2	38.46 ± 6.99	90.18 ± 7.09	ND	-	-
8	111.35 ± 0.36	131.25 ± 0.67	30.83 ± 6.93	100.42 ± 6.96	4245	155.12 ± 20.41	0.98
9	117.50 ± 0.85	133.26 ± 0.42	30.95 ± 3.1	102.31 ± 3.13	3795	123.97 ± 16.31	1.23
10	119.22 ± 4.99	132.87 ± 1.59	30.61 ± 2.19	102.2 ± 2.71	ND	-	-

Table A.13: Summary of results for coating M from test period. MF stands for mould failure. PD stands for partial detachment.

Cycle	**SCA(°)**	**ACA(°)**	**RCA(°)**	**CAH(°)**	**DS (rpm)**	**AS (kPa)**	**ARF**
1	108.13 ± 0.68	118.69 ± 0.42	34.11 ± 2.66	84.57 ± 2.69	4395	166.27 ± 21.88	0.91
2	105.92 ± 5.66	116.69 ± 1.26	35.39 ± 5.5	81.30 ± 5.64	ND	-	-
3	106.72 ± 3.54	118.71 ± 2.32	32.87 ± 5.34	85.84 ± 5.82	4500	174.31 ± 22.94	0.87
4	101.49 ± 1.92	117.42 ± 1.71	35.01 ± 3.14	82.41 ± 3.57	4080	143.29 ± 18.85	1.06
5	96.5 ± 1.1	103.97 ± 0.74	28.58 ± 7.02	75.39 ± 7.06	3975	136.01 ± 17.89	1.12
6	96.42 ± 2.55	105.04 ± 0.27	30.32 ± 5.15	74.72 ± 5.16	4125	146.47 ± 19.27	1.04
7	103.37 ± 1.47	106.35 ± 2.75	32.25 ± 4.83	74.1 ± 5.56	ND	-	-
8	97.55 ± 9.80	108.73 ± 1.26	30.08 ± 2.94	78.65 ± 3.2	ND	-	-
9	97 ± 5.15	105.4 ± 0.96	33.41 ± 1.88	71.99 ± 2.11	ND	-	-
10	100.63 ± 6.19	106.87 ± 0.99	33.92 ± 1.71	72.94 ± 1.98	MF	-	-

Table A.14: Summary of results for coating N from test period. MF stands for mould failure. PD stands for partial detachment.

Cycle	**SCA(°)**	**ACA(°)**	**RCA(°)**	**CAH(°)**	**DS (rpm)**	**AS (kPa)**	**ARF**
1	159.7 ± 3.04	164.69 ± 3.05	138.60 ± 1.24	26.08 ± 3.29	MF	-	-
2	157.83 ± 1.77	160.87 ± 1.35	135.12 ± 2.44	25.75 ± 2.79	540	2.51 ± 0.33	60.55
3	162.28 ± 3.77	164.41 ± 1.45	134.27 ± 2.77	30.14 ± 3.13	MF	-	-
4	164.72 ± 4.6	166.22 ± 3.76	137.48 ± 1.38	28.74 ± 4	1365	16.03 ± 2.11	9.48
5	160.25 ± 7.65	160.32 ± 5.59	117.14 ± 4.81	43.18 ± 7.37	2040	35.82 ± 4.71	4.24
6	155.44 ± 3.89	157.81 ± 3.06	112.89 ± 3.1	44.92 ± 4.35	1800	27.89 ± 3.67	5.45
7	158.7 ± 4.86	160.58 ± 4.09	113.50 ± 3.97	47.08 ± 5.69	MF	-	-
8	155.03 ± 3.19	156.65 ± 2.70	113.36 ± 1.68	43.29 ± 3.18	2025	35.29 ± 4.64	4.31
9	136.87 ± 2.37	147.96 ± 4.17	101.63 ± 1.00	46.33 ± 4.28	2160	40.16 ± 5.28	3.78
10	144.96 ± 1.61	148.44 ± 0.92	105.53 ± 0.40	42.91 ± 1.04	1980	33.74 ± 4.44	4.5

Appendix B

The Biot number calculations will give us an approximate length scale for the distance between the syringe and coated plate required for supercooling. For the assumption of a droplet maintaining its shape as a droplet before impact, the calculated length scale must be larger than 18 mm for the same parameters.

Diameter of a supercooled droplet (D) $\sim$ 23 mm.

Temperature of the droplet (T) = 297.15 K.

Bulk temperature of the air (θ) = 263.15 K (assumed below the freezing temperature for calculative purposes).

Final centreline temperature of the supercooled droplet (Γ) = 273 K.

Terminal Velocity (V) = 300 mm s^{-1}.

Droplet's Reynold Number

$\mathcal{RE} = \frac{\rho_w V l}{\mu}$.

$\rho_w = 1.284\,\mathrm{kg\,m^{-3}}$.

$V = 0.3\,\mathrm{m\,s^{-1}}$.

$l = D = 23 \times 10^{-3}$ m.

$\mu = 1.725$ x 10^{-5} $\mathrm{kg\,m^{-1}s^{-1}}$.

$\mathcal{RE} = (1.284 \text{ x } 0.3 \text{ x } 23 \text{ x } 10^{-3})/(1.725 \text{ x } 10^{-5}) = 514$.

Prandtl Number Calculation

$\mathcal{PR} = \frac{c_p \mu}{\kappa}$

$c_p = 1004\,\mathrm{J\,kg^{-1}\ K^{-1}}$.

$\kappa = 2.428$ x $10^{-2}\ \mathrm{W\,m^{-1}\ K^{-1}}$.

$\mathcal{PR} = (1004$ x 1.725 x $10^{-5})/2.428$ x $10^{-2} = 0.71$

Nusselt Number Calculation

$\mathcal{NU} = 2 + (0.4\mathcal{RE}^{0.5} + 0.06\mathcal{RE}^{0.67})\mathcal{PR}^{0.4}\ (\frac{\mu}{\mu_s})^{0.25}$

$\mu_s = 0.001787\,\mathrm{kg\,m^{-1}s^{-1}}$.

$\mathcal{NU} = 9.25$.

Heat Transfer Coefficient Calculation

$h = \frac{\mathcal{NU}\kappa}{D} = (9.25$ x 2.428 x $10^{-2})/(23$ x $10^{-3}) = 9.76\,\mathrm{W\,m^2\ k^{-1}}$.

Biot Number Calculations

$\mathcal{BI} = \frac{hL}{\kappa_i}$.

$L = \mathrm{r}/3 = \mathrm{D}/6 = 3.83 \times 10^{-3}\mathrm{m}$.

$\kappa_w = 0.571\,\mathrm{J.kg^{-1}K^{-1}}$.

$\mathcal{BI} = (9.76 \text{ x } 3.83 \text{ x } 10^{-3})/0.571 = 0.07$. This shows that the lumped system analysis is applicable since $\mathcal{BI} \leq 0.1$.

Exponent b calculations

$b = \frac{h}{\rho_w c_{pw} L}$.

$\rho_w = 1000\,\mathrm{kg\,m^{-3}}$.

$c_{pw} = 4220\,\mathrm{J\,kg^{-1}\ K^{-1}}$.

$b = (9.76)/(1000 \text{ x } 4220 \text{ x } 3.83 \text{ x } 10^{-3}) = 0.0006$.

Time calculations

$\frac{\Gamma-\theta}{T-\theta} = e^{-bt}$.

(273 - 263.15)/(297.15 - 263.15) = 0.29 = e^{-bt}.

-0.0006 x t = -1.23.

t = 2063 s.

Supercooling distance

supercooling distance = velocity x time = 0.3 x 2063 = 619 m. This value is far greater than 18 mm which validates our hypothesis.

Bibliography

[1] National Weather Service. Icing hazards. *Online Article*, http://www.weather.gov/source/zhu/ZHUTrainingPage/icingstuff/icing/icing.htm. Accessed on 16/02/17, 2014.

[2] Whalen E.A., Broeren A.P., and Bragg M.B. Characteristics of run-back ice accretions and their aerodynamic effects. Technical Report DOT/FAA/AR-07/16, Federal Aviation Administration, 2007.

[3] Federal Aviation Administration. Structural icing type. *Online Article*, Accessed on 19th July 2017:Link – https://www.faasafety.gov/gslac/ALC/course$_c$*ontent.aspx*?cID = $33sID = 152preview = true$, 2017.

[4] Janjua Z.A., Turnbull B., Choy K-L., Pandis C., Liu J., Hou X., and Choi K-S. Performance and durability tests of smart icephobic coatings to reduce ice adhesion. *Applied Surface Science*, 407:555–564, 2017.

[5] Myers T.G. Extension to the messinger model for aircraft icing. *AIAA Journal*, 39(2):211–218, 2001.

[6] Janjua Z.A. The influence of freezing and ambient temperature on the adhesion strength of ice. *Cold Regions Science and Technology*, 140:14–19, 2017.

[7] Laforte C. and Beisswenger A. Icephobic material centrifuge adhesion test. In *11th International Workshop on Atmospheric Icing on Structures*, Montreal, Canada, 2005.

[8] Thomas S.K., Cassoni R.P., and MacArthur C.D. Aircraft anti-icing and de-icing techniques and modelling. *Journal of Aircraft*, 33(5):841–854, 1996.

[9] ISO 12494. Atmospheric icing of structures. Technical Report ISO/TC 98/SC 3, International Organization for Standardization, July 2000.

[10] Politovich M.K. Aircraft icing. *Encyclopaedia of Atmospheric Sciences*, pages 68–75, 2003.

[11] Gent R.W., Dart N.P., and Cansdale J.T. Aircraft icing. *Philosophical Transactions of The Royal Society London A*, 358:2873–2911, 2000.

[12] Fikke S., Ronsten G., Heimo A., Kunz S., Ostrozlik M., Persson P.-E., Sabata J., Wareing B., Wichura B., Chum J., Laakso T., Santti K., and Makkonen L. Cost-727:atmospheric icing on structures: Measurements and data collection on icing: State of the art. Technical Report 75, MeteoSwiss, 2006.

[13] Vargas M., Broughton H., Sims J.J., Bleeze B., and Gaines V. Local and total density measurements in ice shapes. In *43rd AIAA Aerospace Sciences Meeting and Exhibit AIAA-2005-0657*, Reno Nevada, January 2005. Glenn Research Center.

[14] Enzmann F., Miedaner M.M., Kersten M., von Blohn N., Diehl K., Bormann S., Stampanoni M., Ammann M., and Huthwelker T. 3 dimensional imaging and quantification of graupel porosity by synchrotron based micro tomography. *Atmospheric Measurement Techniques*, 4:2225–2234, 2011.

[15] Carras J.N. and Macklin W.C. Air bubbles in accreted ice. *Quarterly Journal of the Royal Meteorological Society*, 101:127–146, 1975.

[16] Varela G.G.A., Castellano N., and Avila E.E. A possible influence of the density of ice accretions on their heat transfer coefficient. *Quarterly Journal of the Royal Meteorological Society*, 131:377–379, 2005.

[17] Chen A. S-H. and Morris S.W. Experiments on the morphology of icicles. *Physics Review E*, 83:026307, 2011.

[18] Politovich M.K. Predicting glaze or rime ice growth on airfoils. *Journal of Aircraft*, 37(1):117–121, 2000.

[19] Ryerson C.C. Ice protection of offshore platforms. *Cold Regions Science and Technology*, 65:97–110, 2011.

[20] Cebeci T. and Kafyeke F. Aircraft icing. *Annual Review of Fluid Mechanics*, 35:11–21, 2003.

[21] Farzaneh M. and Ryerson C.C. Editorial: Anti-icing and deicing techniques. *Cold Regions Science and Technology*, 65:1–4, 2011.

[22] Myers T., Thompson C., and Bandakhavai V.K.S.S. Modelling water flow on aircraft in icing conditions. part 1: Theory and results. In *15th IMACS World Congress on Scientific Computation Modelling and Applied Mathematics*, Germany, 1997. Wissenschaft and Technik.

[23] Mingione G., Barocco M., Denti E., and Bindi F.G. Flight in icing conditions summary. Technical report, French DGAC, 1997.

[24] Broeren A.P., Whalen E.A., Busch G.T., and Bragg M.B. Aerodynamic simulation of runback ice accretion. *Journal of Aircraft*, 47(3):924–939, 2010.

[25] Kasaai M.R. and Farzaneh M. A critical review of evaluation methods of ice adhesion strength on the surface of materials. In *Proceedings of OMAE04, 23rd International Conference on Offshore Mechanics and Arctic Engineering*, Vancouver, British Columbia, Canada, June 20-25 2004. ASME.

[26] Anderson D.N. and Reich A.D. Tests of the performance of coatings for low ice adhesion. In *AIAA, 35th Aerospace Sciences Meeting and Exhibit*, Reno, Nevada, 1997.

[27] Susoff M., Siegmann K., Pfaffenroth C., and Hirayama M. Evaluation of icephobic coatings - screening of different coatings and influence of roughness. *Applied Surface Science*, 282:870–879, 2013.

[28] Gohardani O. and Hammond D.W. Ice adhesion to pristine and eroded polymer matrix composites reinforced with carbon nanotubes for potential usage on future aircraft. *Cold Regions Science and Technology*, 96:8–16, 2013.

[29] Kraj A.G. and Bibeau E.L. Measurement method and results of ice adhesion force on the curved surface of a wind turbine blade. *Renewable Energy*, 35:741–746, 2010.

[30] Kulinich S.A. and Farzaneh M. Ice adhesion on super-hydrophobic surfaces. *Applied Surface Science*, 255:8153–8157, 2009.

[31] Bharathidasan T., Vijay Kumar S., Bobji M.S., Chakradhar R.P.S., and Basu B.J. Effect of wettability and surface roughness on ice-adhesion strength of hydrophilic, hydrophobic and superhydrophobic surfaces. *Applied Surface Science*, 314:241–250, 2014.

[32] Saito H., Takai K., and Yamauchi G. Water and ice repellant coatings. *Surf. Coat. Int. B: Coat. Trans.*, 80(4):168–171, 1997.

[33] Momen G., Jafari R., and Farzaneh M. Ice repellency behaviour of superhydrophobic surfaces: Effects of atmospheric icing conditions and surface roughness. *Applied Surface Science*, 349:211–218, 2015.

[34] Jin Z. and Hu H. Icing process of small water droplets impinging onto a frozen cold plate. *Journal of Thermophysics and Heat Transfer*, 24(4):841–844, 2010.

[35] Sayward J.M. Special report 79-11: Seeking low ice adhesion. Technical report, Cold Regions Research and Engineering Laboratory, Corps of Engineers, United States Army, Hanover: New Hampshire, 1979.

[36] Li X., Zhao Y., Li H., and Yuan X. Preparation and icephobic properties of polymethyltrifluoropropylsiloxane-polyacrylate block copolymers. *Applied Surface Science*, 316:222–231, 2014.

[37] Jafari R., Menini R., and Farzaneh M. Superhydrophobic and icephobic surfaces prepared by rf-sputtered polytetrafluoroethylene coatings. *Applied Surface Science*, 257:1540–1543, 2010.

[38] Zhang K., Li X., Zhu K., Li Y., Tao C., and Yuan X. Uv-curable poss-fluorinated methacrylate diblock copolymers for icephobic coatings. *Progress in Organic Coatings*, 93:87–96, 2016.

[39] Li Y., Luo C., Li X., Zhang K., Zhao Y., Zhu K., and Yuan X. Submicron/nano-structured icephobic surfaces made from fluorinated polymethlysiloxane and octavinyl-poss. *Applied Surface Science*, 360:113–120, 2016.

[40] Menini R. and Farzaneh M. Elaboration of Al_2 O_3 /ptfe icephobic coatings for protecting aluminum surfaces. *Surfaces Coatings Technology*, 203:1941–1946, 2009.

[41] Jung S., Dorrestijn M., Raps D., Das A., Megaridis C.M., and Poulikakos D. Are superhydrophobic surfaces best for icephobicity? *Langmuir*, 27:3059–3066, 2011.

[42] Nosonovsky M. and Hejazi V. Why superhydrophobic surfaces are not always icephobic. *ACS Nano*, 6:8488–8491, 2012.

[43] Kulinich S.A., Farhadi S., Nose K., and Du X.W. Superhydrophobic surfaces: Are they really ice-repellant? *Langmuir*, 27:14143–14150, 2011.

[44] Li H., Li X., Luo C., Zhao Y., and Yuan X. Icephobicity of polydimethylsiloxane-b-poly (fluorinated acrylate). *Thin Solid Films*, 573:67–73, 2014.

[45] Messinger B.L. Equilibrium temperature of an unheated icing surface as a function of air speed. *Journal of Aeronautical Sciences*, pages 29–42, 1953.

[46] Poots G.I. Ice and snow accretion on structures. *Research Studies Press*, 1996.

[47] Bourgault Y., Beaugendre H., and Habashi W.G. Development of a shallow-water icing model in fensap-ice. *Journal of Aircraft*, 37(4):640–646, 2000.

[48] Brakel T.W., Charpin J.P.F., and Myers T.G. One-dimensional ice growth due to incoming supercooled droplets impacting on a thin conducting substrate. *International Journal of Heat and Mass Transfer*, 50:1694–1705, 2007.

[49] Cao Y., Ma C., Zhang Q., and Sheridan J. Numerical simulation of ice accretions on an aircraft wing. *Aerospace Science and Technology*, 23:296–304, 2012.

[50] Myers T.G. and Thompson P. Modelling the flow of water on aircraft in icing conditions. *American Institute of Aeronautics and Astronautics*, 36(6):1010–1013, 1998.

[51] Myers T.G. and Hammond D.W. Ice and water film growth from incoming supercooled droplets. *International Journal of Heat and Mass Transfer*, 42:2233–2242, 1999.

[52] Myers T.G., Charpin J.P.F., and Thompson C.P. Slowly accreting ice due to supercooled water impacting on a cold surface. *Physics of Fluids*, 14(1):240–256, 2002.

[53] Hansman Jr. R.J. and Turnock S.R. Investigation of surface water behavior during glaze ice accretion. *Journal of Aircraft*, 26(2):140–147, 1989.

[54] Gong X. and Chen R. Total pressure loss mechanism of centrifugal compressors. *Mechanical Engineering Research*, 4(2):45–59, 2014.

[55] Smith R.B. and Gronas S. Stagnation points and bifurcation in 3-d mountain airflow. *Tellus*, 45A:28–43, 1993.

[56] Yamaguchi K. and Hansman Jr. R.J. Heat transfer on accreting surfaces. *Journal of Aircraft*, 29(1):108–113, 1992.

[57] Karev A.R., Farzaneh M., and Lozowski E.P. Character and stability of a wind-driven supercooled water film on an icing surface-i: Laminar heat transfer. *International Journal of Thermal Sciences*, 42:481–498, 2003.

[58] Karev A.R., Farzaneh M., and Lozowski E.P. Character and stability of a wind-driven supercooled water film on an icing surface-ii: Transition and turbulent heat transfer. *International Journal of Thermal Sciences*, 42:499–511, 2003.

[59] Yanxia D., Yewei G., Chunhua X., and Xian Y. Investigation on heat transfer characteristics of aircraft icing including runback water. *Journal of Heat and Mass Transfer*, 53:3702–3707, 2010.

[60] Strobl T., Raps D., and Hornung M. Comparative evaluation of ice adhesion behaviour. *World Academy of Science, Engineering and Technology*, 68:1673–1678, 2012.

[61] Guerin F., Laforte C., Farinas M-I., and Perron J. Analytical model based on experimental data of centrifuge ice adhesion tests with different substrates. *Cold Regions Science and Technology*, 121:93–99, 2016.

[62] Drelich J. Guidelines to measurements of reproducible contact angles using a sessile-drop technique. *Ice Science*, DOI: 10.1680/si.13.00010:1–7, 2013.

[63] Doppenschmidt A. and Butt H-J. Measuring the thickness of the liquid-like layer on ice surfaces with atomic force microscopy. *Langmuir*, 16(16):6709–6714, 2000.

[64] Makkonen L. Ice adhesion - theory, measurements and countermeasures. *Journal of Adhesion Science and Technology*, 26:413–445, 2012.

[65] Meuler A.J., Smith D.J., Varanasi K.K., Mabry J.M., McKinley G.H., and Cohen R.E. Relationships between water wettability and ice adhesion. *ACS Applied Materials Interfaces*, 2(11):3100–3110, 2010.

[66] Wang N., Xiong D., Deng Y., and Wang K. Mechanically robust superhydrophobic steel surface with anti-icing, uv-durability and corrosion resistance properties. *ACS Applied Materials and Interfaces*, 7:6260–6272, 2015.

[67] Wang N., Xiong D., Lu Y., Pan S., Wang K., Deng Y., and Shi Y. Design and fabrication of the lyophobic slippery surface and its application in anti-icing. *The Journal of Physical Chemistry C*, 120:11054–11059, 2016.

[68] Zhang L., Wu J., Hedhili M.N., Yang X., and Wang P. Inkjet printing for direct micropatterning of a superhydrophobic surface: toward biomimetic fog harvesting surfaces. *Journal of Materials Chemistry A*, 3:2844–2852, 2015.

[69] Cao L., Jones A.K., Sikka V.K., Wu J., and Gao D. Anti-icing superhydrophobic coatings. *Langmuir*, 25(21):12444–12448, 2009.

[70] Della Volpe C., Siboni S., and Morra M. Comments on some recent papers on interfacial tension and contact angles. *Langmuir*, 18(4):1441–1444, 2002.

[71] Yuan Y. and Lee T.R. Chapter 1 - contact angle and wetting properties. In *Surface Science Techniques*, Bracco G., B. Holst (eds), 2013. Springer-Verlag Berlin Heidelberg.

[72] Kulinich S.A. and Farzaneh M. How wetting hysteresis influences ice adhesion strength on superhydrophobic surfaces. *Langmuir*, 25(16):8854–8856, 2009.

[73] Ling E.J.Y., Uong V., Renault-Crispo J-S., Kietzig A-M., and Servio P. Reducing ice adhesion on nonsmooth metallic surfaces: wettability and topography effects. *ACS Applied Materials and Interfaces*, 8:8789–8800, 2016.

[74] Epstein M. and Fauske H. Kinetic and heat trasnfer controlled solidification of highly supercooled droplets. *International Journal of Heat and Mass Transfer*, 36(12):2987–2995, 1993.

[75] Hindmarsh J.P., Russell A.B., and Chen X.D. Experimental and numerical analysis of the temperature transition of a suspended freezing water droplet. *International Journal of Heat and Mass Transfer*, 46:1199–1213, 2003.

[76] Chaudhary G. and Li R. Freezing of water droplets on solid surfaces: An experimental and numerical study. *Experimental Thermal and Fluid Science*, 57:86–93, 2014.

[77] Hu J., Xu K., Wu Y, Lan B., Jiang X., and Shu L. The freezing process of continuously sprayed water droplets on thesuperhydrophobic silicone acrylate resin coating surface. *Applied Surface Science*, 317:534–544, 2014.

[78] Shen Y., Tao H., Chen S., Zhu L., Wang T., and Tao J. Icephobic/anti-icing potential of superhydrophobic Ti_6 Al_4 v surfaces with hierarchical textures. *RSC Advances*, 5:1666–1672, 2015.

[79] Huang L., Liu Z., Liu Y., Gou Y., and Wang L. Effect of contact angle on water droplet freezing process on a cold flat surface. *Experimental Thermal and Fluid Science*, 40:74–80, 2012.

[80] Oberli L., Caruso D., Hall C., Fabretto M., Murphy P.J., and Evans D. Condensation and freezing of droplets on superhydrophobic surfaces. *Advances in Colloid and Interface Science*, 210:47–57, 2014.

[81] Ozbay S. and Erbil H.Y. Ice accretion by spraying supercooled droplets is not dependent onwettability and surface free energy of substrates. *Colloids and Surfaces A: Physicochemical Engineering Aspects*, 504:210–218, 2016.

[82] Ramachandran S.G. and Shih T.I-P. Biot number analogy for design of experiments in turbine cooling. *Journal of Turbomachinery*, 137(6):1–14, 2015.

[83] Shen Y., Tao J., Tao H, Chen S., Pan L., and Wang T. Anti-icing potential of superhydrophobic Ti_6 Al_4 v surfaces: Ice nucleation and growth. *Langmuir*, 31:10799–10806, 2015.

[84] Poots G. and Skelton P.L.I. A simple mathematical model for rime and glaze-ice accretion due to freezing rain on a horizontal plane surface. *Atmospheric Environment*, 26A:1029–1040, 1992.

[85] Sherif S.A., Pasumarthi N., and Bartlett C.S. A semi-empirical model for heat transfer and ice accretion on aircraft wings in supercooled clouds. *Cold Regions Science and Technology*, 26:165–179, 1997.

[86] Stefan J. Über die theorie der eisbildung insbesondere über die eisbildung im polarmeere sitzungsberichte der kaiserlichen akademie der wissenschaften mathematische-naturwissenschaftliche. *Classe II Abtheilung*, 98:965–983, 1889.

[87] Verdin P. *An Automatic Multi-Stepping Approach for Aircraft Ice Prediction.* PhD thesis, Cranfield University, 2007.

[88] Myers T.G., Charpin J.P.F., and Chapman S.J. The flow and solidification of a thin fluid film on an arbitrary three-dimensional surface. *Physics of Fluids*, 14(8):2788–2803, 2002.

[89] Myers T.G. and Charpin J.P.F. A mathematical model for atmospheric ice accretion and water flow on a cold surface. *International Journal of Heat and Mass Transfer*, 47:5483–5500, 2004.

[90] Xin L., Junqiang B., Jun H., Kun W., and Yang Z. A spongy model for aircraft icing. *Chinese Journal of Aeronautics*, 27(1):40–51, 2014.

[91] Worster M.G. Convection in mushy layers. *Annual Review of Fluid Mechanics*, 29:91–122, 1997.

[92] Macklin W.C. The density and structure of ice formed by accretion. *Quarterly Journal of the Royal Meteorological Society*, 88:30–50, 1962.

[93] Williams E.R. and Zhang R. Density of rime in laboratory simulations of thunderstorm microphysics and electrification. *Journal of Geophysical Research*, 101(D23):29715–29719, 1996.

[94] Dong Y.Y. and Hallett J. Droplet accretion during rime growth and formation of secondary ice crystals. *Quarterly Journal of the Royal Meteorological Society*, 115:127–142, 1989.

[95] Hobbs P.V. Ice in clouds. *Proceedings of 1990 Cloud Physics Conference*, American Meteorological Society:600–606, 1990.

[96] Battisti L. *Wind Turbines in Cold Climates - Icing Impacts and Mitigation Systems*. Springer International Publishing, New Delhi, India, 2015.

[97] Lynch F. T. and Khodadoust A. Effect of ice accretions on aircraft aerodynamics. *Progress in Aerospace Sciences*, 37:669–767, 2001.

[98] Mirzaei M., Ardekani M. A., and Doosttalab M. Numerical and experimental study of flow field characterstics of an iced aerofoil. *Aerospace Science and Technology*, 13:267–276, 2009.

[99] Worster M.G. *Perspectives in Fluid Dynamics: A Collective Introduction to Current Research (edited by. G.K. Batchelor, H.K. Moffatt and M.G. Worster)*, chapter Solidification of fluids, pages 393–446. Cambridge University Press, 2000.

[100] Valarezo W.O. Aerodynamic performance effects due to small leading edge ice (roughness) on wings and tails. *Journal of Aircraft*, 30(6):807–812, 1993.

[101] Binzaid S., Al-Tomal S.A., Zaid D., and Rosen M.H. Deicing technology for modern military and commercial aircraft wing surfaces. In *Electrical and Electronic Engineering Proceedings of the Conference on Engineering Research, Innovation and Education 2011*, Sylhet, Bangladesh, 11-13 January 2011. CERIE.

[102] Gao H. and Rose J.L. Ice detection and classification on an aircraft wing with ultrasonic shear horizontal guided waves. *IEEE Transactions on Ultrasonics, Ferroelectrics and Frequency Control*, 56(2):334–344, 2009.

[103] Palacios J.L., Brouwers E.W., Han Y., and Smith E.C. Adverse environment rotor test stand calibration procedures and ice shape correlation. *American Helicopter Society 66th Annual Forum, Phoenix, AZ, May 11-13*, 2010.

[104] Ruff G. Analysis and verification of the icing scaling equations. *Air Force Technical Report AEDC-TR-85-30*, November 1985.

[105] Feltham D.L. and Worster M.G. Flow-induced morphological instability of a mushy layer. *Journal of Fluid Mechanics*, 391:339–361, 1999.

[106] Huppert H.E. and Worster M.G. Dynamic solidification of a binary melt. *Nature*, 314(25):703–707, 1985.

[107] Aseev D.L. and Alexandrov D.V. Unidirectional solidification with a mushy layer - the influence of weak convection. *Acta Materialia*, 54:2401–2406, 2006.

[108] Alexandrov D.V. and Nizovtseva I.G. To the theory of underwater ice evolution, or nonlinear dynamics of "false bottoms". *International Journal of Heat and Mass Transfer*, 51:5204–5208, 2008.

[109] Alexandrov D.V. and Ivanov A.A. Solidification of a ternary melt from a cooled boundary or nonlinear dynamics of mushy layers. *International Journal of Heat and Mass Transfer*, 52:4807–4811, 2009.

[110] Bhatta D., Muddamallappa M.S., and Riahi D.N. On weakly nonlinear evolution of convective flow in a passive mushy layer. *Nonlinear Analysis: Real World Applications*, 11:4010–4020, 2010.

[111] Alexandrov D.V. and Malygin A.P. Flow-induced morphological instability and solidification with the slurry and mushy layers in the presence of convection. *International Journal of Heat and Mass Transfer*, 55:3196–3204, 2012.

[112] Neufeld J.A., Goldstein R.E., and Worster M. On the mechanisms of icicle evolution. *Journal of Fluid Mechanics*, 647:287–308, 2010.

[113] Chung C.A. and Chen F. Morphological instability in a directionally solidifying binary solution with an imposed shear flow. *Journal of Fluid Mechanics*, 436:85–106, 2001.

[114] Chiareli A.O.P. and Worster M.G. On measurement and prediction of the solid fraction within mushy layers. *Journal of Crystal Growth*, 125:487–494, 1992.

[115] Jahrling K. and Tait S. Measurements of the evolution of porosity in a mushy layer. *Journal of Crystal Growth*, 167:285–291, 1996.

[116] Huppert H.E. and Hallworth M.A. Solidification of NH_4Cl and NH_4Br from aqueous solutions contaminated by $CuSO_4$: the extinction of chimneys. *Journal of Crystal Growth*, 130:495–506, 1993.

[117] Riahi D.N. On non-linear magneto in a mushy layer with joule heating. *International Journal of Non-Linear Mechanics*, 47(4):49–54, 2012.

[118] Neufeld J.A. and Wettlaufer J.S. Shear-enhanced convection in a mushy layer. *Journal of Fluid Mechanics*, 612:339–361, 2008.

[119] Neufeld J.A. and Wettlaufer J.S. An experimental study of shear-enhanced convection in a mushy layer. *Journal of Fluid Mechanics*, 612:363–385, 2008.

[120] Beavers G.S. and Joseph D.L. Boundary conditions at a naturally permeable wall. *Journal of Fluid Mechanics*, 30(1):197–207, 1967.

[121] Shinkafi A. and Lawson C. Enhanced method of conceptual sizing of aircraft electro-thermal de-icing system. *World Academy of Science, Engineering and Technology*, 8(6):1077–1084, 2014.